Fall 2019

Graphene-Based Water Desalination Using Atomistic Simulations

Thanh Chinh Nguyen
Southern Methodist University, chinhn@smu.edu

GRAPHENE-BASED WATER DESALINATION USING ATOMISTIC SIMULATIONS

Approved by:

_____
Prof. Ali Beskok
Professor of Mechanical Engineering

_____
Prof. Vladimir Ajaev
Professor of Mathematics

_____
Prof. David Willis
Professor of Mechanical Engineering

_____
Prof. MinJun Kim
Professor of Mechanical Engineering

_____
Prof. Paul S. Krueger
Professor, Chair of Mechanical Engineering

GRAPHENE-BASED WATER DESALINATION USING ATOMISTIC SIMULATIONS

A Dissertation Presented to the Graduate Faculty of

Lyle School of Engineering

Southern Methodist University

in

Partial Fulfillment of the Requirements

for the degree of

Doctor of Philosophy

with a

Major in Mechanical Engineering

by

Chinh Thanh Nguyen

(B.E., Electronics and Communications Engineering, Danang University of Technology, Vietnam, 2011)
(M.Sc., Mechanical Engineering, University of Ulsan, South Korea, 2016)

December 21, 2019

Acknowledgements

I would like to thank my dissertation advisor Prof. Ali Beşkök, for his incessant support through my graduate studies as well as his mentoring, encouragements and his friendship during this period. One of the most wonderful things in my life is the chance to work with him who is an excellent scientist and a very nice person. This dissertation would not have been accomplished without his precious advices. Furthermore, without him, I would not have had the chance to meet exceptional people during my graduate study. I also would like to thank my other advisory committee members, Professors David Willis, Vladimir Ajaev, MinJun Kim, and Paul Krueger for their contributions in this dissertation.

Additionally, I would like to especially thank Prof. BoHung Kim for his great help on my early days in the field and his endless encouragements. I am also grateful for invaluable help and support of past group members namely Alper Tunga Celebi, Anil Koklu, Amin Mansoorifar, Jafar Ghorbanian, and Yigit Akkus.

Finally, a great thanks to my family, especially my wife and my little baby boy. Without their love and support this dissertation would not be completed successfully.

Nguyen, Chinh Thanh B.E., Danang University of Technology, Vietnam, 2011
M.Sc., University of Ulsan, South Korea, 2016

Graphene-Based Water Desalination using Atomistic Simulations

Advisor: Professor Ali Beskok

Doctor of Philosophy conferred: 12/21/2019
Dissertation completed: 11/18/2019

My research focused on investigating saltwater transport through nanoporous graphene membranes using molecular dynamics (MD) simulations. Particularly, in this dissertation, we focused on pressure-driven flows of salt water through uncharged and charged nanoporous graphene membranes for water desalination applications. In the first study, desalination performance of uncharged single-layer nanoporous graphene membranes was observed based on volumetric flow rate, required pressure drop, and salt rejection efficiency. A functional relationship between the volumetric flow rate, pressure drop, pore diameter, and the dynamic viscosity of saltwater was also examined. In further studies, transport of salt ions through positively and negatively charged single-layer nanoporous graphene membranes with large hydraulic diameters was investigated. I discovered that the positively charged membranes are better than the negatively charged ones in filtering salt ions. The largest pore diameter for which positively charged single-layer graphene membranes still conserve high salt rejection efficiency ($\geq 98\%$) is 18.9 Å. I also showed that using charged bilayer graphene membranes is a good remedy, in which, perfect salt rejection can be obtained while pressure drop is lower than that required for the uncharged single-layer graphene membranes with the same salt removal efficiency.

TABLE OF CONTENTS

LIST OF FIGURES

Chapter 1

INTRODUCTION

The rapidly increasing population of the world is the main cause of the growing demand for fresh water worldwide. These days, many countries are still facing a water scarcity problem in which 25% of the world's population has no safe water. In addition, approximately half of the population have no proper sanitation, and each year four million children die of water-borne disease [1]. Developing affordable and clean technologies along with advanced personalized learning, economical solar energy, virtual reality enhancement, brain reverse-engineering, better medicines, health informatics, urban infrastructure improvements, secure cyberspace, providing energy from fusion, preventing nuclear terror, nitrogen cycle management, developing carbon sequestration methods, engineering the tools of scientific discovery are the 14 Grand Challenges for Engineering in the 21st century [2]. Therefore, enhancing water purification processes, addressed in terms of permeability, selectivity, and power consumption, is the ultimate goal in developing water purification technologies. Here, permeability is the ability of semipermeable membranes to allow transport of water without any chemical or physical distortion of the membranes. It can be quantified using volumetric flow rates or volumetric fluxes. Selectivity represents the ability of the membranes to prevent leakage of salt ions. It is usually quantified as the ratio of salt amount remained past a membrane to the initial salt amount in the feed stream. Since seawater is the largest water resource on earth, seawater desalination is the most promising approach to solve the fresh water scarcity

problem [3]. Over the past half-century, reverse osmosis (RO) membrane-based desalination technology has been developed to meet the critical goal of water desalination. Because of the advances in continuous process improvements including module design, process design, feed pre-treatment, and reduction in energy consumption, RO desalination is still the most promising method, although some alternative technologies have also been proposed [4, 5]. It has been shown that membrane-based reverse osmosis (RO) water desalination has the largest share in installed plants (80%) and production capacity (44%) as compared to other commercial technologies [6].

Improvement of the mechanical, chemical and biological properties of membranes can significantly affect their desalination performance. A variety of membrane types, such as polymeric membranes made of cellulose triacetate and thin film composite polyamide [7-10], zeolite [11, 12], and carbon nanotube (CNT) membranes [13, 14], have been investigated. Desalination efficiencies of these types of membranes are still limited due to their low permeability, degradation by chlorine, and low fouling resistance. Due to their single-atom thickness, high mechanical strength and elasticity [15], and stability [16], graphene membranes attracted considerable attention for improving water desalination efficiency. Thanks to the development in fabrication methods, large-scale single-layer graphene membranes can be fabricated based on roll-based growth and separation of graphene films on a copper foil [17]. There are three forms of graphene including pristine graphene, graphene oxide (GO), and reduced graphene oxide (rGO) [18]. Pristine graphene is a single-layer of carbon atoms arranged in hexagonal lattice structure. Natural graphite can be oxidized using strong oxidants accompanied by strong acids to produce GO. Single GO sheets which contain oxygen functional groups can be then exfoliated by

ultrasonication [19, 20]. GO can be converted to rGO through reduction processes such as chemical reduction, electro-reduction, thermal annealing, flash reduction and enzymatic reduction with some residual oxygen atoms and structural defects [21]. Nanopores with pore diameter even in sub-nanometer scale can be fabricated using different technologies such as oxygen plasma etching [22], ion-bombardment [23, 24], electron-beam lithography with scanning transmission electron microscope (STEM) [25, 26], and electrical pulse [27]. **Figure 1.1** shows the comparison in shape and size between graphene nanopore models and those created by the argon ion bombardment method. **Figure 1.2** illustrates graphene

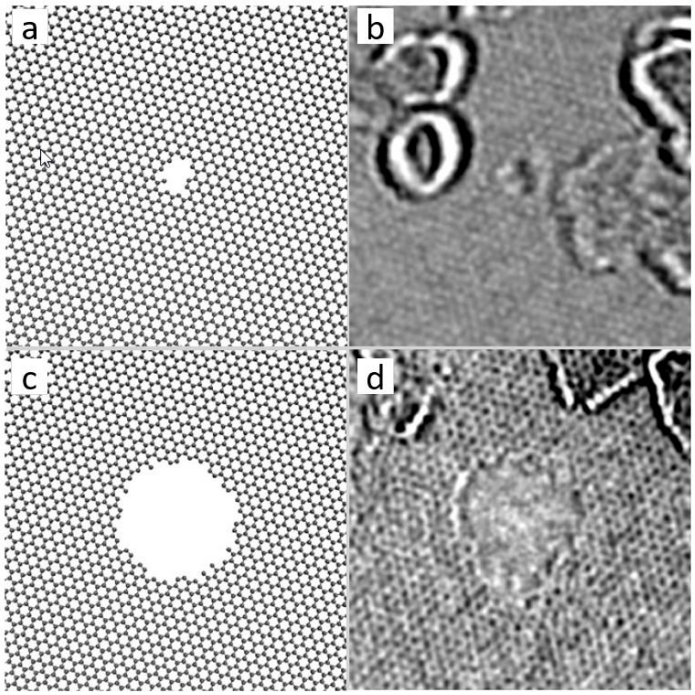

Figure 1.1. Comparison of graphene nanopore models (a and c) and experimental TEM images (b and d) of those created using the argon ion bombardment method with an average radius of 2.9 Å (b) and 12.2 Å (d). Figure adopted from [23].

nanopores created by the STEM method. Nanoporous graphene sheets can endure pressures higher than 57.0 MPa, as long as their supporting substrate pore diameters are smaller than 1.0 μm [28]. Furthermore, because of the hexagonal structure of graphene with the lattice constant of 2.46 Å, which is even smaller than the diameter of a water molecule (2.9 Å), graphene is impermeable to ionic aqueous solutions. Depending on their pore size, pristine graphene membranes can retard transport of salt ions due to the hydrodynamic interactions between ions and the pore edges, whereas water molecules can pass through them. These unique characteristics make nanoporous graphene membranes potentially robust salt-selective materials. Recently, there have been significant efforts to investigate the applicability of graphene and graphene-based membranes for water desalination. It was experimentally shown that graphene oxide membranes with sub-nanometer pore sizes can efficiently sieve out salt ions while maintaining reasonable flow rates [29-31], and single-layer graphene membranes were fabricated and utilized in water desalination systems with good selectivity and permeability [22, 24]. Although the desalination performances of the single-layer graphene membranes in the aforementioned studies mainly depended on membrane fabrication technologies, obtained results confirm practical applicability of graphene and graphene-based membranes for water desalination. Desalination performance of pristine and chemically functionalized graphene membranes has also been investigated using numerical simulations, primarily focusing on the relation between nano-pore diameter and desalination efficiency. For example, Cohen-Tanugi and Grossman used MD simulations to model RO water desalination process using pristine nano-porous graphene membranes [32]. In addition to showing a linear relationship between water flux and applied pressure, the authors identified that a maximum pore

diameter of 5.5 Å was necessary to prevent salt ion transport. Konatham *et al*. have shown that the energy barrier exerted on salt ions (Na^+ and Cl^-) by pristine graphene membrane increases with decreasing pore diameter and reported a maximum pore diameter of 7.5 Å for water desalination [33]. It was found that passivating chemical functional groups such as hydroxyl and hydronium groups on the edges of graphene pores significantly enhance water permeability [32, 34] whereas adding carboxyl (COO^-) groups enables exclusion of Cl^- ions more effectively [33]. The mechanisms of salt rejection for pristine nanoporous graphene membranes are based on size exclusion and steric exclusion of the hydration shell, whereas those for the chemically passivated nanoporous graphene membranes relies on the interactions of solutes with the chemical structures of the nanopore. Chen *et al*. reported that passivation of graphene pore edges using nitrogen atoms increased water flux six times compared with that of pristine graphene membranes [35].

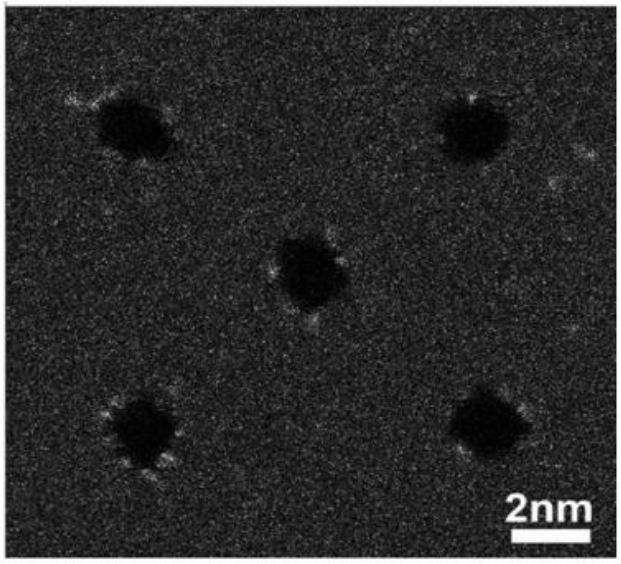

Figure 1.2. Graphene nanopores created using the STEM method with diameters smaller than 2 nm. Figure adopted from [26].

In previous MD studies, pressure-driven flows were created either by applying constant forces on rigid pistons made from single-layer graphene sheets [32, 36] (as shown in **Fig. 1.3**) or by applying constant forces on water molecules [34]. The former method establishes a pressure difference between the feed and permeate sides using two pistons located in the upstream and downstream of the simulation domain and specifying two different yet opposing forces on each piston. This force difference is balanced by the viscous losses (forces) on the membrane to induce a steady flow rate that is determined by MD simulations. However, in this approach van der Waals (vdW) interactions between the pistons and water can lead to a difference between the forces applied on each system and

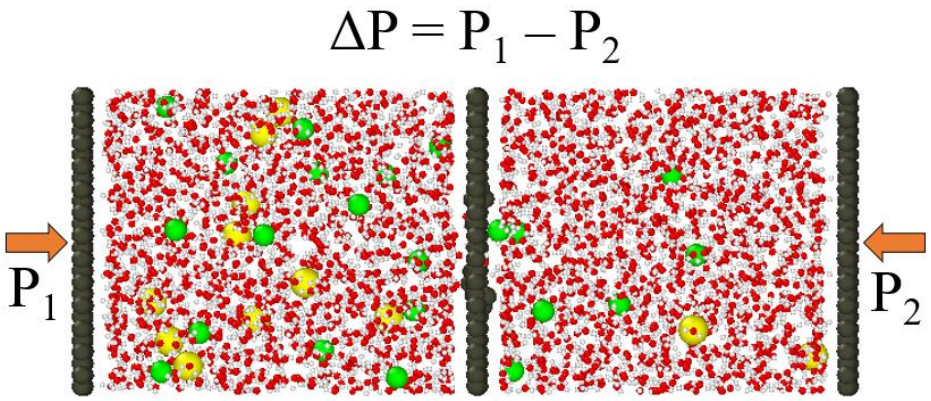

Figure 1.3. Pressure-driven flows through nanoporous graphene membranes created by applying constant forces on rigid pistons made from single-layer graphene sheets bounding the simulation domain. A nanoporous graphene membrane in the middle separates feed an permeate reservoirs. Carbon atoms, sodium ions, chloride ions, oxygen atoms, and hydrogen atoms are shown in black, yellow, green, red, and white, respectively.

the resulting bulk pressure in the feed and permeate reservoirs, leading to imprecision in the imposed pressure drop. In addition, the volume of the MD domain cannot be fixed, which can be an issue for canonical ensemble of MD results. The latter method based on

applying constant forces on all liquid molecules in the system does not exactly mimic pressure-driven flow, since the pressure gradient in an actual membrane system is not constant or unidirectional. Therefore, the previous MD results obtained for desalination performance of single-layer graphene membranes can be affected by the methodologies used to induce flow. The *objective* of the first part of this dissertation was to reassess transport of saltwater through pristine single-layer graphene membranes by using a new method to induce pressure-driven flows for MD modelling of RO water desalination processes. In this part of study, the water flows through the nanoporous membranes were created by moving two specular reflection boundaries located at the upstream and downstream of the domain with equal speed. This approach preserves the MD simulation volume and specifies a flow rate. The resulting pressures were calculated in the feed and permeate reservoirs to obtain the flow rate versus pressure drop characteristics. In addition, desalination performance of pristine single-layer nanoporous graphene membranes is observed based on volumetric flow rate, required pressure drop, and salt rejection efficiency. A functional relationship between the volumetric flow rate, pressure drop, pore diameter, and the dynamic viscosity of saltwater is also examined.

Utilizing charged nanoporous graphene membranes can enhance water desalination systems. In this method, salt rejection mechanism is based on Donnan exclusion theory which predicts that charges fixed on a semipermeable membrane impede the transport of counter-ions through it [37]. Based on this principle, larger pore sizes with fixed charges can be efficient in ion rejection when the electrostatic interactions between the charges and mobile ions are more dominant than the steric exclusion of the hydration shell of ions and hydrodynamic effects. Zhao *et al*. reported that charged-modified graphene nanopores

enhance the transport of counter-ions (K^+) and provide nearly complete exclusion of co-ions (Cl^-) under an applied electric field with pore diameters up to 12.0 Å [38]. O'Hern *et al*. revealed that ion-irradiated graphene nanopores with sub-nanometer diameters are cation-selective at short oxidation time due to the charges terminated on the pore edges [24]. In addition, Rollings *et al*. showed that electrophoretic transport of K^+ ions through single-layer graphene nanopores are preferentially allowed as compared to that of Cl^- ions [39]. Sint *et al*. demonstrated that graphene nanopores passivated with negatively charged nitrogen and fluorine as well as positively charged hydrogen are selective for counter-ions [40]. Konatham *et al*. pointed out that the negative charges of COO^- groups passivated on graphene nanopores enhance exclusion of Cl^- ions [33]. In the next part of this dissertation, we demonstrate the potential application of charged nanoporous single-layer graphene membranes in RO water desalination systems. This is reasonable, since charges accumulate at the edges and corners of conductors. In addition, the graphene nanopores can acquire charges by local oxidation [27, 41], electrical biasing [42, 43], or by other chemical methods [44-46]. **Figure 1.4(a)** shows a schematic of an oxidized nanoporous graphene membrane with attached carboxylic groups on pore edge. Deprotonation [46] or protonation [47] of carboxylic (COOH) functional groups renders negatively or positively charged pores, respectively. **Figure 1.4(b)** illustrates a schematic of creating a charged graphene nanopore using electrical biasing. This part focuses on the transport of salt ions through charged nanoporous graphene membranes with a hydraulic diameter of 14.40 Å. Our *objectives* are to reduce the required pressure drop significantly, while still preserving a practical salt rejection efficiency for this large pore size. To the best of our knowledge,

this is one of the first studies in the literature on utilization of charged graphene membranes for pressure-driven water desalination systems.

In addition to graphene, h-BN is also an extremely thin two-dimensional (2D) material, which can be fabricated with different techniques [48-51]. Interestingly, the boron and nitrogen components of h-BN membranes are also arranged in a honeycomb structure similar to graphene with a bit greater lattice constant. It shares outstanding properties with graphene such as high mechanical strength and high thermal stability [50, 52]. Nevertheless, h-BN shows other unique properties including chemical inertness, extremely

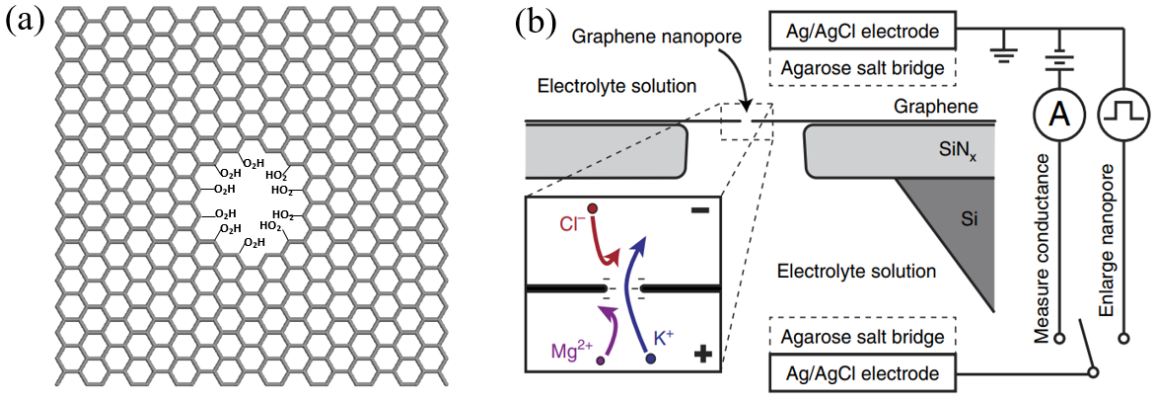

Figure 1.4. (a) Schematic of an oxidized nanoporous graphene membrane with attached carboxylic groups. (b) Diagram of a suspended graphene nanopore placed in an electrolyte solution. Calibration of pore size using electrical pulses or ionic current measurement is done by Ag/AgCl electrodes in contact with the solution via agarose salt bridges. Inset illustrates the interactions between the negatively charged nanopore and ions. Figure (b) adopted from [39].

high electrical impedance, and a wide energy gap [53-55]. Gao *et al.* [56] have examined the applicability of h-BN for water desalination using MD simulations. It was shown that h-BN membranes can provide high permeability and salt removal percentage, which are

controllable with proper pore shape designs. Therefore, nanoporous h-BN membrane is also a potential material for RO water desalination. In the third part of this dissertation, I first attempted to make a comparison in desalination performance between uncharged graphene and h-BN membranes at the same simulation conditions. The lower performance of h-BN membranes as compared to that of graphene membranes confirmed the superiority of graphene in RO desalination applications. On the other hand, the promising results obtained for positively charged 14.40 Å pore diameter single-layer graphene confirm the dominancy of electrostatic interactions between the fixed charges and mobile ions as compared to the steric and hydrodynamic effects for the investigated pore size. Therefore, it is required to further investigate ion rejection by positively charged nanoporous graphene membranes with larger pore sizes. The ultimate objectives are reducing the required pressure drop significantly, while still preserving a practical salt rejection efficiency. This study provides an optimal setting for positively charged single-layer nanoporous graphene membranes to obtain the best desalination performance in terms of salt rejection efficiency and required pressure drop at the specified high flow rate. Finally, although the obtained results for the charged single-layer nanoporous membranes are promising with reduced pressure drops as compared to the uncharged base-line case, salt rejection efficiencies are not 100%. In some scenarios, perfect salt rejection efficiencies are mandatory, especially for drinkable water. For seawater with salt concentration of 0.6 M, even a rejection percentage of 99% leaves filtered water with 0.006 M (> 0.0017 M), which is not drinkable [57]. Based on the analyses of the transport of ions through positively charged single-layer nanoporous graphene in optimal cases, only a small portion of Cl^- ions go downstream. This leads to a motivation of placing a secondary negatively low-charged nanoporous

graphene membrane behind the first one to prevent the passing of Cl^- ions. The ultimate goal is to obtain the perfect salt rejection efficiency with a pressure drop that is sustainably lower than the uncharged base-line case. This is the first approach in using charged bilayer nanoporous graphene membranes for RO desalination, although using pristine bilayer membranes ones has been proposed in the literature [58, 59]. The ultimate purpose is to come up with an optimal setting for charged bilayer nanoporous graphene membranes in which the best desalination performance is attained in terms of salt rejection efficiency and required pressure drop at the specified high flow rate.

Chapter 2

MOLECULAR DYNAMICS SIMULATIONS

In this section, the fundamentals of molecular dynamics simulations are provided.

2.1. Introduction

Molecular dynamics (MD) simulation is a computational method used to describe the evolution of positions, velocities, and orientations of atoms/molecules in a system with time. This method was first successfully implemented on a computer by Alder and Wainwright in 1957 with simple elastic collision between spherical objects [60]. With the rapid development of computer technology, present day MD simulations have become more powerful and present themselves as good alternatives for expensive experiments in predicting dynamical behaviors of atoms in a system. MD simulations are extremely useful in explaining the physical insights which cannot be attained by experiments at atomistic scale. MD simulations can be referred to "computational experiments" due to the analogy between the simulations and experiments in terms of conducting processes as shown in **Fig. 2.1**. MD simulations now are able to simulate not only simple liquid atoms but also complex water molecules, hydrocarbons, polymers, and biological molecules. The biggest limitation of MD simulations is the high computational cost, especially for systems requiring a large number of atoms.

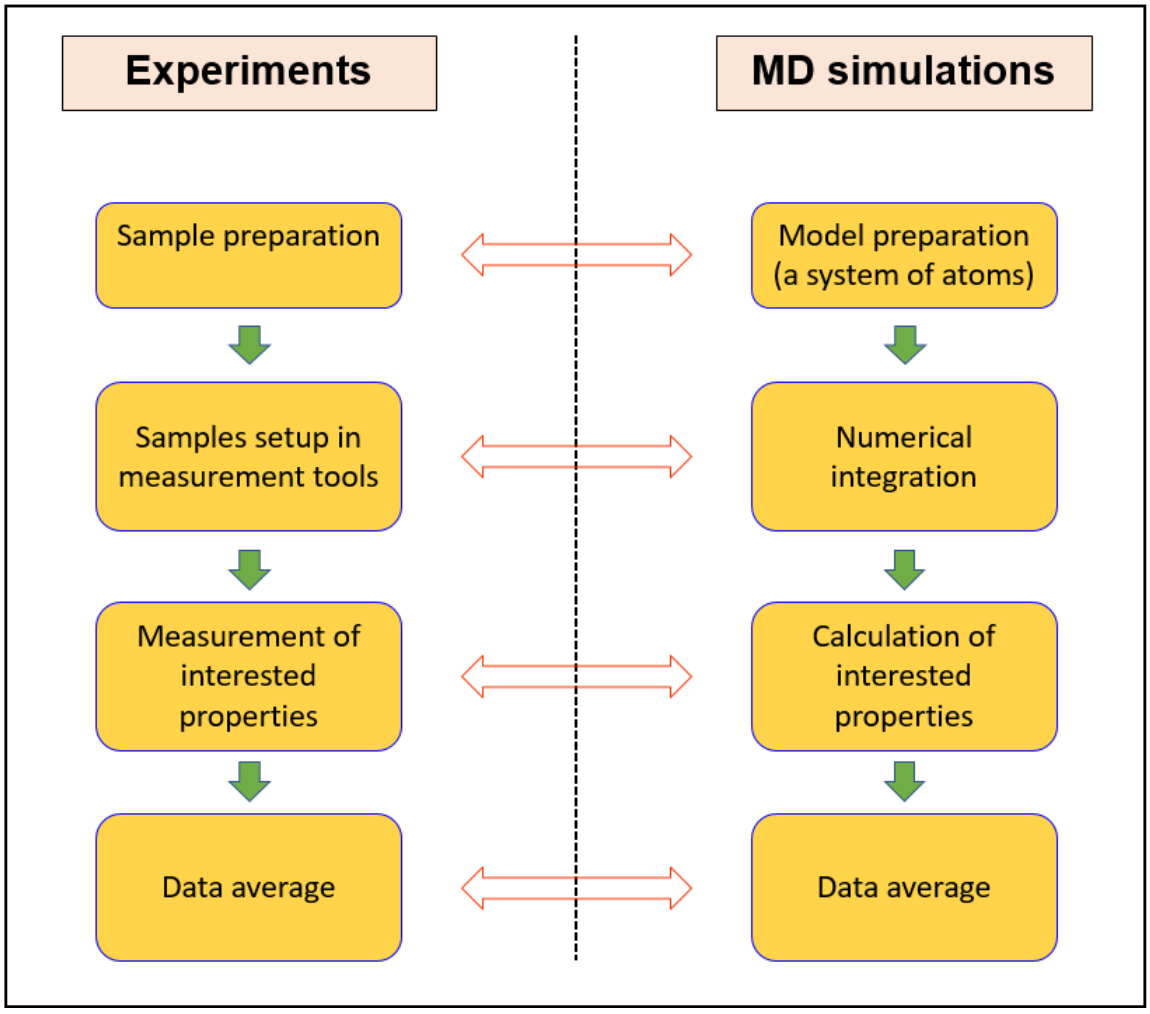

Figure 2.1. Equivalent operating steps in experiments and MD simulations.

2.2 Operating Principles of MD Simulations

Figure 2.2 presents a schematic for the working flow of MD simulations. After a simulation model is prepared with a specified number of atoms, the interaction models for the atoms are defined. Initial positions of the atoms are generated based on the physical

state of each material such as fluid or solid with crystal structures. Gas or liquid atoms are usually generated randomly while crystal structures are kept in defined shapes with bonded potentials. Initial velocities of atoms are generated based on the Maxwell-Boltzmann equation at a defined temperature. The Maxwell-Boltzmann equation provides the probability that an atom has three velocity component values in three corresponding directions (x, y, z) as follows:

$$p(v_{ix}, v_{iy}, v_{iz}) = \left(\frac{m_i}{2\pi k_B T}\right)^{\frac{2}{3}} e^{\frac{m_i (v_{ix}^2 + v_{iy}^2 + v_{iz}^2)}{2k_B T}} \tag{2.1}$$

where v_{ix}, v_{iy}, and v_{iz} are the velocity components in the *x*, *y*, and *z* directions, respectively; k_B is the Boltzmann constant, *T* is the absolute temperature, and m_i is the mass of the atom. At a timestep, the total force applied on each atom is calculated by numerically solving Newton's second law:

$$\vec{F} = m\vec{a} \tag{2.2}$$

where *F* is total force, *m* is mass of atom, and *a* is acceleration. Based on the calculated total forces and the motion equation, the acceleration of each atom can be obtained. The new positions and velocities of the atom can be calculated based on the equations of motion:

$$v_{i,\Delta t} = v_o + a\Delta t \tag{2.3}$$

$$r_{i,\Delta t} = r_o + v_o(\Delta t) + \frac{1}{2}\, a(\Delta t)^2 \tag{2.4}$$

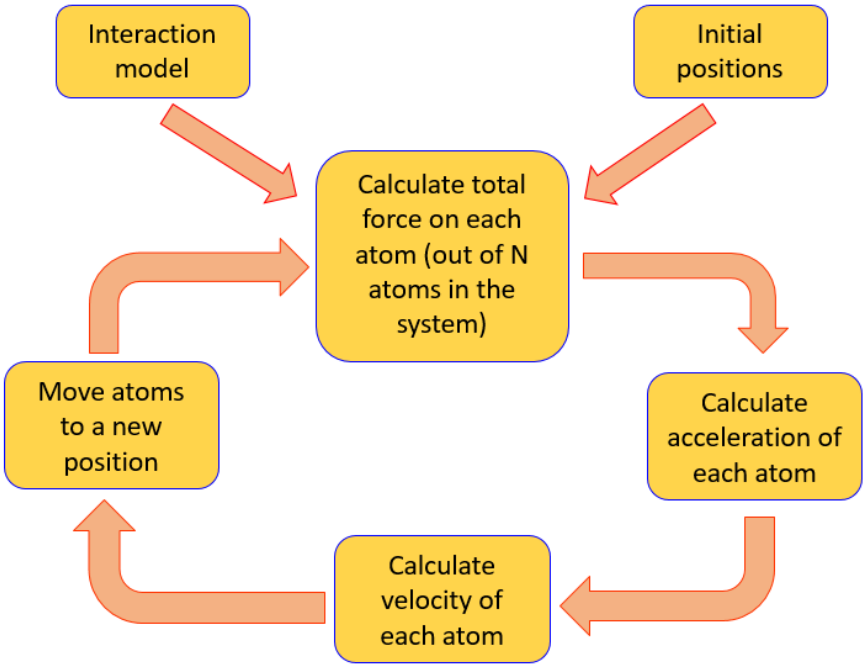

Figure 2.2. Flowchart for working flow in MD simulations.

where Δt is the time-step. The integration of motion equations in MD simulations can be simplified by using time integration algorithms. There are a couple of methods namely Leap-frog, Beeman's and Verlet. Of these, the Verlet algorithm is the most popular one which is simple and effective. It uses position and acceleration of an atom at both current and one time-step backward to calculate the new position at a next timestep based on Taylor series expansion. The center-of-mass velocity of the atom is then approximated using the past and next time positions (central difference) as:

$$v(t) = \frac{r(t+\Delta t) - r(t-\Delta t)}{2(\Delta t)} + O(\Delta t)^3 \qquad (2.5)$$

All the atoms in the systems will be moved to the next positions at the next time-step and the loop continues to the end of simulation time. Depending on the number of atoms in the system, interaction models, and CPU types, simulation time can be several picoseconds or can be up to several hundreds of nanoseconds. Currently there many powerful software packages for MD simulations such as LAMMPS [61], NAMD [62], GROMACS [63], and CHARMM [64]. LAMMPS is used in all the studies of this dissertation.

2.3 Interaction Models

Interactions between the atoms in a system are modeled by interatomic potentials or molecular force fields [65]. Molecular force fields are the sets of parameters used to calculate the energy potential of atoms in a system. The force fields are preferably used for big molecules with complicated structures like biological molecules. Interatomic potentials are mathematical functions describing the potential energy of the atomic system based on the positions of the atoms. They are usually used to describe interactions between atoms or simple molecules. The derivatives of the potentials are forces acting on the atoms. Intermolecular potentials are categorized into non-bonded and bonded potentials.

Non-bonded potentials include van der Waals (vdW) attractions and electrostatic interactions. The instantaneous dipoles inside atoms due to the movement of electrons causes vdW forces. The Lennard-Jones (LJ) potential is the most popular and accurate one mimicking vdW interactions described as follows:

$$V_{\mathrm{LJ}} = 4\varepsilon\left[\left(\frac{\sigma_{\mathrm{ij}}}{r_{\mathrm{ij}}}\right)^{12} - \left(\frac{\sigma_{\mathrm{ij}}}{r_{\mathrm{ij}}}\right)^{6}\right] \tag{2.6}$$

where ε is the well-depth of the potential presenting the interaction strength; σ is the intermolecular diameter defined as the distance between the two atoms where potential is zero; r_{ij} is the instantaneous distance between two atoms. The first term in Eq. 2.6 presents repulsive potentials at $r_{\mathrm{ij}} < \sigma_{\mathrm{ij}}$ while the second term illustrates attractive potentials at $r_{\mathrm{ij}} > \sigma_{\mathrm{ij}}$. **Figure 2.3** shows LJ potential values with respect to the distance between two atoms. As seen in the figure, at the distance of approximately 10 Å, the potential value approaches zero. Therefore, computational cost can be saved by using a cut-off distance of approximately 3σ for LJ potential to exclude long-range interactions [66]. Thus, a truncated LJ potential is used to describe vdW interactions as follows:

$$V_{\mathrm{LJ}} = \begin{cases} 4\varepsilon\left[\left\{\left(\frac{\sigma_{\mathrm{ij}}}{r_{\mathrm{ij}}}\right)^{12} - \left(\frac{\sigma_{\mathrm{ij}}}{r_{\mathrm{ij}}}\right)^{6}\right\} - \left\{\left(\frac{\sigma_{\mathrm{ij}}}{r_{\mathrm{c}}}\right)^{12} - \left(\frac{\sigma_{\mathrm{ij}}}{r_{\mathrm{c}}}\right)^{6}\right\}\right], r_{\mathrm{ij}} < r_{\mathrm{c}} \\ 0, r_{\mathrm{ij}} \geq r_{c} \end{cases} \tag{2.7}$$

where r_{c} is cut-off distance. The use of truncated LJ potential prevents the discontinuity in energy conservation and the motion of atoms in which potential values are set to zero at distances larger than the cut-off value.

In addition to vdW interactions, electrostatic interactions must be included for any atoms having charge. The well-known Coulombic potential is integrated in simulations described as follows:

$$V_{C} = \frac{1}{4\pi\varepsilon_{\mathrm{o}}}\sum_{i}^{n}\sum_{j}^{m}\frac{q_{\mathrm{i}}q_{\mathrm{j}}}{r_{\mathrm{ij}}} \tag{2.8}$$

where ε_o is the vacuum dielectric constant; q_i and q_j are the charge values of atom *i* and *j*, respectively; and r_{ij} is the instantaneous distance between two atoms. **Figure 2.4** shows typical Coulombic potential value as a function of intermolecular distance. Repulsive and

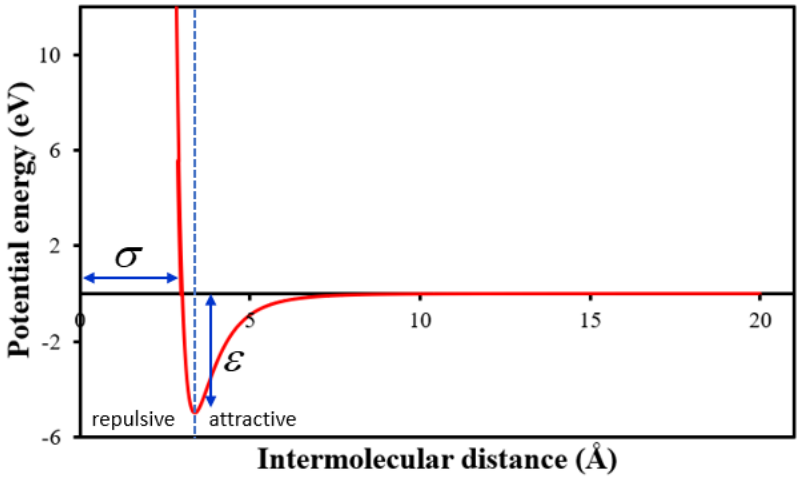

Figure 2.3. Lenard-Jones potential as a function intermolecular distance

attractive interactions are clearly seen with co-charge and counter-charge atoms, respectively. It is also observed that Columbic interactions are effective at much longer range as compared to vdW interactions. This requires a very large computation, causing a burden on computational cost. The Ewald summation method is used to solve this problem in MD simulations. This method divides Coulombic interactions into two parts including short-range and long-range ones. The short-range interactions are calculated in a real space defined by a cut-off distance similar to that with vdW interactions. The long-range interactions are calculated in reciprocal space in which the electrostatic interactions of charged atoms in infinite periodic images of the simulation domain are calculated and then summed. The sum can be presented as a Fourier transform and converted to fast Fourier

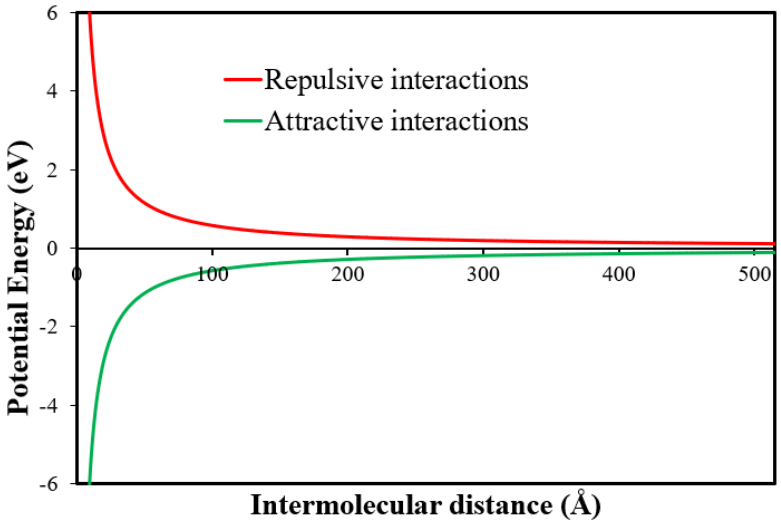

Figure 2.4. Coulombic potential as a function of intermolecular distance

transform in MD simulations [67]. In reciprocal space, these interactions converge quickly, allowing efficient computation through application of fast Fourier transforms. The Ewald summation method is associated with periodic boundary conditions of the simulation domain which will be explained later in this chapter. In addition, this long-range electrostatic summation method is only applicable for systems with zero net charge. Numerical approximation of the Ewald summation can be implemented in MD simulations using the particle mesh Ewald (PME) technique [68] or a particle-particle particle-mesh (PPPM) solver [69, 70].

Bonded potentials are used to describe covalent bonds between atoms within a molecule (i.e. oxygen and hydrogen atoms in a water molecule) or those between atoms in a lattice structure (i.e. carbon atoms in hexagonal graphene). Bonded potentials are associated with all intramolecular interactions including bonds, dihedrals, angles, and improper (out-of-

plane bending). The well-known harmonic potential which treats atoms as spheres and bond strength as spring stiffness is widely used to present bonded potentials in molecular dynamics simulations. The general mathematical equation for bonded potentials is described as follows:

$$V_B = \sum_{\text{bond}} k_b(b\text{-}b_0)^2 + \sum_{\text{angle}} k_\theta(\theta\text{-}\theta_0)^2 + \sum_{\text{dihedral}} k_\varphi(1+\cos(\varphi+\varphi_0))^2 + \sum_{\text{improper}} k_\omega(\omega\text{-}\omega_0)^2 \qquad (2.9)$$

where k_b, k_θ, k_φ, and k_ω are stiffness constants for stretching, angle bending, dihedral torsion, and improper, respectively; b_0 and φ_0 are initial bond lengths; θ_0 and ω_0 are initial angles. There are different bonded potentials/force fields utilized in MD simulations such as SPC/E, TIP3P, TIP4P/2005 for water molecules [71], CHARMM [72], AMBER [73], GROMOS [74] for biological molecules, and EAM [75], AREIBO [76], Tersoff [77] for solid crystals. Different interaction parameters, stiffness constants, and bond lengths are provided in these potentials/force fields depending on the simulated materials.

2.4 Thermodynamic Ensembles and Boundary Conditions

2.4.1. Thermodynamic Ensembles

A thermodynamic ensemble is a simplified thermodynamic system which represents the possible state of a large system. It is used to derive the properties of a real thermodynamic system based on the laws of classical and quantum mechanics. Microscopic properties of the particles inside an ensemble are used to calculate macroscopic properties of the system such as temperature, pressure, and energy based on statistical mechanics when the

ensemble is in statistical equilibrium. The typical ensembles used in MD simulations are canonical ensemble (NVT), microcanonical ensemble (NVE), isobaric-isothermal ensemble (NPT), and grand canonical ensemble (μcVT).

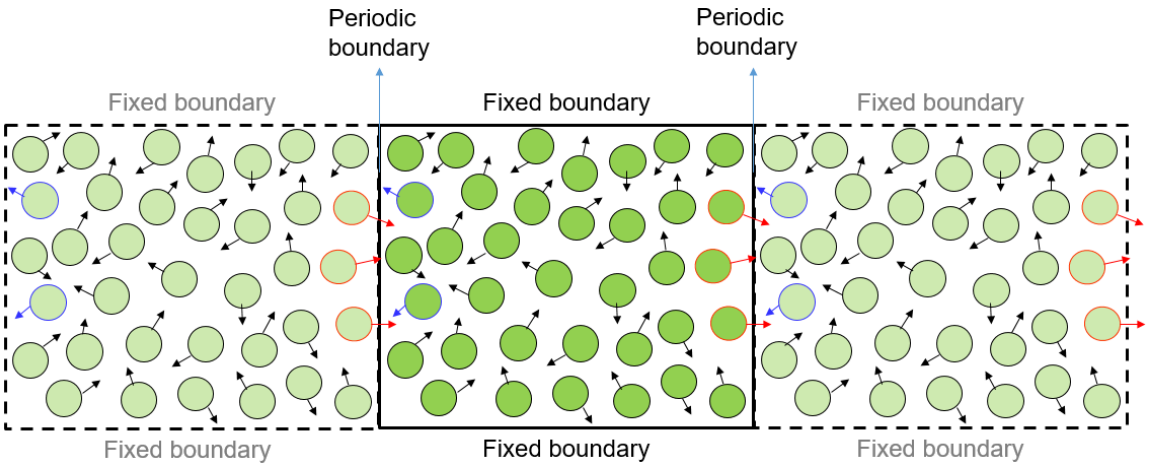

Figure 2.5. Illustration of fixed boundary condition and periodic boundary condition for a simulation domain.

The canonical ensemble (NVT) is defined as a constant number of particles (N), constant volume (V), and constant temperature (T) ensemble. This ensemble generates possible microscopic states of a system at a fixed temperature using a heat bath. The system can exchange energy with surroundings so its energy is not constant with time. The microcanonical ensemble (NVE) represents a system with constant number of particles (N), constant volume, and constant energy (E). Energy transfer cannot occur between the system and its surroundings. Thus, the energy of the system is not changing with time. No specific temperature is defined and temperature is only obtained by interactions with heat sources or both heat sources and heat sinks inside the system. This ensemble is useful in

simulating systems with heat transfer. Isobaric-isothermal ensemble (NPT) is described as constant number of particles (N), constant pressure (P), and constant temperature (T). In this ensemble, energy exchange can occur with the surroundings while volume can be adjusted so that internal pressure is consistent with pressure applied on the system by surroundings. The temperature in this ensemble is kept constant using a heat bath similar to the NVT ensemble. NPT ensemble is useful in representing chemical systems in which reactions occur under constant pressure. Finally, grand-canonical ensemble (μ_cVT) is a system of constant chemical potential (μ_c), constant volume, and constant temperature. Energy and mass transfer can occur with surroundings to approach thermal and chemical equilibrium. A heat bath is used to control the temperature of the system.

2.4.2. Boundary Conditions

The boundaries of a domain in MD simulations can be defined as fixed or periodic. For the fixed boundary condition, no particles can pass through the boundary. In periodic boundary conditions (PBCs), particles can leave at one end of the simulation domain and come back into the other end with unchanged velocity. This allows particles to interact across a boundary. **Figure 2.5** shows an illustration for a simulation domain with both fixed boundary condition and PBCs. PBCs allow infinite replication of system image in the defined directions. Due to the high computational cost and data analysis, only a small system of particles (ensemble) is simulated. Infinite repeats of the system image and cross-boundary interactions allow reproducing macroscopic properties of a much larger system. However, the number of particles in the simulation domain should be large enough (i.e.

obeying local thermal equilibrium) to avoid unphysical behavior based on results in literature [78].

2.5 MD Calculation of the Stress Tensor

A local stress can be defined based on an infinitesimally small volume constrained by surfaces A_α normal to the Cartesian axes $\alpha = x, y, z$ as illustrated in Fig. 2.6. Conventionally, the resulting forces (F_β) applied on each surface A_α in the direction of the Cartesian axes $\beta = x, y, z$ cause the local stress tensor element $S_{\beta\alpha}$ defined as:

$$S_{\beta\alpha} = \frac{F_\beta}{A_\alpha} \tag{2.10}$$

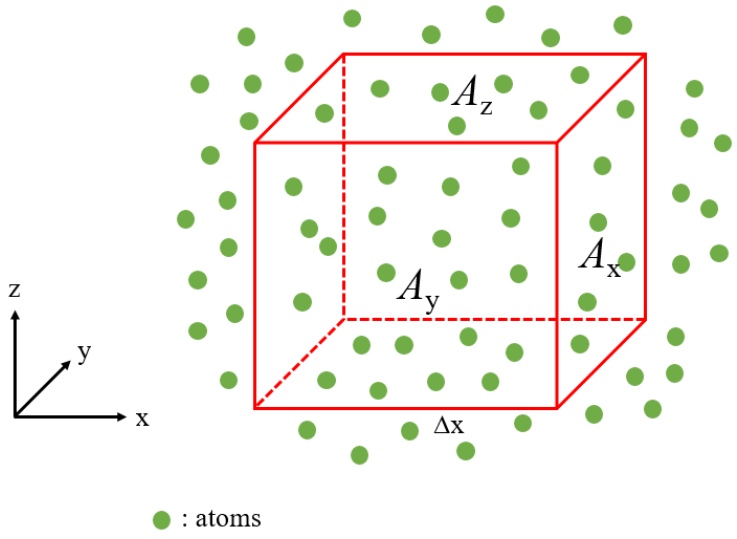

Figure 2.6. Illustration of a defined small volume in which local stress tensors are determined. Atoms moving in and around the volume are shown in green.

In MD simulations, the calculation of local stress tensor elements is based on the binning method which divides a simulation domain into many small volumes. Selecting a proper bin size is critical to obtain the correct stress tensor components. For example, bin sizes should be large enough so that the atoms inside strictly obey the local thermal equilibrium condition. Irving and Kirkwood [79] proposed a method to calculate local stress tensors for molecular systems based on the equations of hydrodynamics as follows:

$$S_{\beta\alpha} = \frac{1}{A_\alpha \Delta\alpha} \sum_{i} m_i v_{i\beta} v_{i\alpha} + \frac{1}{A_\alpha} \sum_{ij} F_{ij\beta} \tag{2.11}$$

where m_i is the mass of atom i; $v_{i\beta}$ is the velocity of atom i in β direction; $v_{i\alpha}$ is the velocity of atom i in α direction; $\Delta\alpha$ is the length of the side associated with axis α; and $F_{ij\beta}$ is the resulting force between two atoms (i and j) in β direction. The first term in Eq. 2.11 represents kinetic energy contribution, whereas the second term characterizes virial contribution. The kinetic part counts for stresses induced inside the defined volume ($A_\alpha \times \Delta\alpha$) by thermal motion of atoms based on kinetic theory. The virial part can come interactions between atoms on opposite sides of an area (A_α) due to vdW interactions, Coulombic interactions, and intramolecular constraints. The details about how bins are created within the simulation domain are presented in Chapter 3.

Chapter 3

SALTWATER TRANSPORT THROUGH PRISTINE NANOPOROUS GRAPHENE MEMBRANES

Transport of saltwater through pristine single-layer nanoporous graphene membranes is investigated using molecular dynamics (MD) simulations. Pressure-driven flows are induced by motion of specular reflection boundaries at feed and permeate sides with constant speed. Unlike previous studies in the literature, this method induces a desired flow rate and calculates the resulting pressure difference in the reservoirs. Due to the hexagonal structure of graphene, the hydraulic diameters of nano-pores are used to correlate flow rate and pressure drop data. Simulations are performed for three different pore sizes and flow rates. In order to create better statistical averages for salt rejection efficiencies, ten different initial conditions of Na^+ and Cl^- distribution in the feed side are used for each simulation case. Using data from 90 distinct simulation cases and utilizing the Buckingham Pi theorem I develop a functional relationship between volumetric flow rate, pressure drop, pore-diameter and the dynamic viscosity of saltwater. A linear relationship between the volumetric flow rate and pressure drop is observed. Graphene membranes with 9.90 Å pore dimeter results in 100% salt rejection with 163.2 L/h-cm^2 water flux, requiring a pressure drop of 35.02 MPa.

3.1. Simulation Settings and Methods

The simulation system consists of saltwater in the feed side (left) and pure water in the permeate side (right), while the two sides are separated by a fixed membrane as shown in **Fig. 3.1(a)**. Both ends of the system are bounded by specular reflection boundaries. As depicted in **Fig. 3.1(b)**, an atom interacting with a specular reflection boundary reverses its normal momentum while preserving its incident tangential momentum. Initially the two specular reflection boundaries are fixed at z = 0.0 Å and z = 87.08 Å, respectively, whereas the graphene membrane is fixed at z = 44.92 Å. The *x*- and *y*-directions in the simulation domain are periodic with the lengths of 33.17 Å and 31.25 Å, respectively. The obtained decimal place accuracy for the dimensions of the simulation domain is based on sub-nanometer lattice constant of graphene and the requirements in fixing an exact thermodynamic state of water. Both pristine and positively charged graphene membranes are used in the system. For each type of membrane, a pore is created in the middle of the membrane by removing carbon atoms. **Fig. 3.1(c)** shows a typical structure of a single-layer graphene membrane with a nano-pore. Due to the hexagonal structure of graphene, the nano-pore is noncircular. Therefore, I define hydraulic diameter $D_h = 4A_h / p$, where the pore circumference (p) is obtained by the distance between all carbon atoms on the pore edge, and the pore area (A_h) is the space constrained by the circumference. Using this definition, pore dimeters of 9.90 Å, 11.57 Å and 14.40 Å are selected, which are in the range suggested in previous studies [32, 33]. Using the nomenclature defined by Yuan *et al*. [80], the pore dimeters of 9.90 Å, 11.57 Å and 14.40 Å correspond to 24*a*, 36*a*, and 54*a*, respectively, in which "*a*" means removed atoms .

A simple point charge (SPC/E) model, which can be described as effective rigid pair potentials comprised of Lennard-Jones (LJ) and Coulombic terms, was chosen for water molecules due to its simplicity and low computational cost [81]. This water model has three interaction sites corresponding to the three atoms of a water molecule. A point charge was assigned to each atom to model the long-range Coulombic interactions and the oxygen atom also exhibits Lennard-Jones (LJ) potential to model the van der Waals (vdW) forces. Specifically, oxygen and hydrogen atoms are assigned partial charges of q_O = - 0.8476e and q_H = 0.4238e, respectively. The harmonic O-H bond length of 0.1 nm and the H-O-H angle of 109.47^o were kept rigid using the SHAKE algorithm [82]. The LJ potential was used to describe the intermolecular interactions of salt ions, oxygen atoms in the water molecules, and carbon atoms in the graphene membranes. I used the truncated LJ (12-6) potential to model the vdW interactions (Eq. 2.7). The intermolecular forces were truncated at a cut-off distance of 10.0 Å. The tail correction method was used to compensate for long-range interactions in the LJ terms. Interaction parameters between the oxygen atoms were obtained from the SPC/E model [81], while interaction parameters between oxygen atoms and carbon atoms were based on the empirical data obtained from the contact angle measurement method [83]. Also, the interaction parameters of sodium and chloride in the aqueous solutions were taken from GROMACS force field, which is based on quantum calculations [84]. In-plane interactions between the carbon atoms of the graphene membranes are described by AIREBO potential [76]. Coulombic interactions were also applied for any atomic species with charge. In our system, sodium ions (Na^+) and chloride ions (Cl^-) were used to represent the dissolved salt ions and they are assigned charges of q_{Na} = 1.0e and q_{Cl} = -1.0e, respectively. All the interaction parameters are summarized in

Table 3.1. The PPPM method was used to correct the long-range electrostatic interactions between all charged atomic species [85]. Newton's equations of motion were integrated using the VERLET algorithm with a simulation time step of 1.0 fs which is a scale of chemical bond vibrations. A larger time step cannot properly simulate the physical behavior of atoms due to the fast vibrations of bonds. All the simulations were performed using LAMMPS [61].

Table 3.1. The interaction parameters utilized in the simulations.

Interaction	**ε (eV)**	**σ (nm)**	**q (e)**
H-H	0	0	$q_H = 0.4238$
O-O	0.006736616	3.1656	$q_O = -0.8476$
O-Na	0.002079272	2.8704	N.A
O-Cl	0.005575083	3.8068	N.A
O-C	0.004062790	3.1900	N.A
Na-Na	0.000641772	2.5752	$q_{Na} = +1$
Cl-Cl	0.004613823	4.4480	$q_{Cl} = -1$
Na-Cl	0.001702700	3.5116	N.A
Na-C	0.001350014	2.9876	N.A
Cl-C	0.003619748	3.9240	N.A

Initially 1500 water molecules were added in the feed side and 1200 water molecules were added in the permeate side. The smaller number of water molecules in the permeate reservoir was used to save computational cost while a defined thermodynamic state of water was still preserved. Salt concentration in the feed region was chosen as 0.6 M, which is equivalent to the salinity of seawater. Based on this, the feed reservoir initially contained 14 Na^+ ions and 14 Cl^- ions. The Maxwell-Boltzmann velocity distribution at 300 K was

used for assigning initial conditions of all liquid molecules. Equilibrium MD simulations with two adjacent NVT (constant number of molecules, volume, and temperature) ensembles were initially used with a Nose-Hoover thermostat to retain the system at 300 K. In the first NVT ensemble, flow through a pore was not created because the pore had been closed by a plug for both pristine and charged membrane cases. The plug's area is the same with the pore area and it was modeled by utilizing the carbon atoms originally belonging to the graphene sheet. The pore plug was used to separate the two reservoirs from each other. By doing this, the thermodynamic states of water in both sides were fixed at a density of 0.997 g/cm^3 and a temperature of 300 K, while the salt concentration in the feed region was fixed at 0.6 M. The initial state was equilibrated for at least 20.0 ns for both pristine and charged membrane cases. For the next NVT ensemble, the pore plug was opened, and the system was relaxed until the bulk pressures in the feed and permeate sides equilibrated for at least 80.0 ns. Finally, non-equilibrium MD simulations were used to establish flow through the pore by moving the two specular refection boundaries with the same velocity in the *z*-direction, whereas the graphene membrane was fixed. By doing this, the total volume of the system is always conserved and the flow rate is manifested by the volume decrease in the feed side and the volume increase in the permeate side. In all of the simulations, the middle membrane was thermally vibrating in order to include the effects of mechanical deformation and wettability characteristics of the membrane on the desalination process. It was shown previously that using fixed atom membranes (cold wall model) affects the water and salt ion distributions at the solid-liquid interfaces [86], which impacts transport of saltwater through the membranes [87]. Data acquisition for the transport of water molecules and salt ions was started immediately after the motion of the

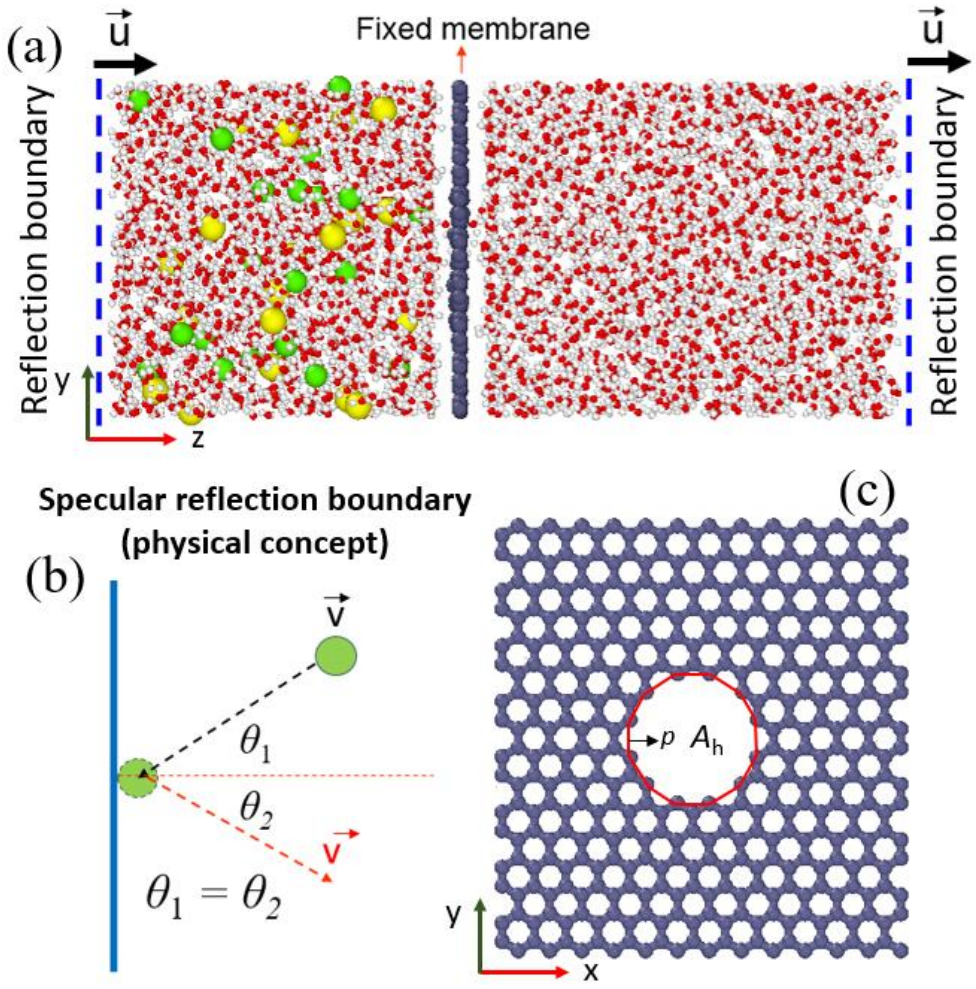

Figure 3.1 (a) Schematics of the simulation domain in side view. The size of sodium ions (yellow) and the size of chloride ions (green) are exaggerated for better visualization. (b) Definition of a specular reflection wall. (c) Typical structure of a graphene membrane with a pore in the middle.

reflection boundaries and lasted 8.0 ns. The data were collected by dividing the computational domain into slab bins along the *z*-direction with a slab size of 0.6 Å. In each slab bin, there are approximately more than 300 atoms (oxygen atoms, hydrogen atoms, and salt ions) at a time. The data were recorded for every 10,000 time-steps (10 ps), resulting in 800 time-dumps for each simulation. The MD data for the saltwater transport

through the membranes for each specified setting (pore diameter or velocity) were averaged using the ones obtained from *ten* different simulations started off at different equilibrium points from the equilibrating process. Any adjacent equilibrium points had at least 1.0 ns time-difference to ensure that flow rate simulations begin with the random positions of the ions in the feed side. This approach enabled us to start the flow rate simulations from different initial conditions, which is crucial to address the limitations induced by small number of simulated Na^+ and Cl^- ions, when reporting the ion separation efficiency of the membranes. Based on the three selected pore diameters and three selected boundary velocity values for each pore diameter, totally I have performed 90 different simulations to obtain the presented data.

3.2 Results and Discussion

Equilibrium MD simulations were used to fix the thermodynamic state of water at 0.997 g/cm^3 and 300 K, before pressure-driven flow cases were created. The local mass density of water and salt ionic concentrations were obtained by dividing the computational domain into slab bins along the z-direction as shown in **Figure 3.2(a)**. **Figure 3.2(b)** shows the density distribution of water along the z-direction of the system. It is shown that the bulk density of water in both sides of the membranes was found to correspond to 0.997 g/cm^3. The well-known density layering phenomenon [88-91] near solid-liquid interfaces is observed. **Figure 3.2(c)** presents the ionic concentration of Na^+ and Cl^- ions along the z-

direction of the system. The bulk ionic concentration of Na^+ and Cl^- ions are approximately equal and maintained at approximately 0.6 M (equivalent to that of sea water). **Figure 3.2(d)** shows normalized densities of oxygen and hydrogen atoms in the vicinity of the pristine graphene membrane. Density peaks show that oxygen and hydrogen atoms are located in the same position. This phenomenon is consistent with what is reported in literature [92, 93].

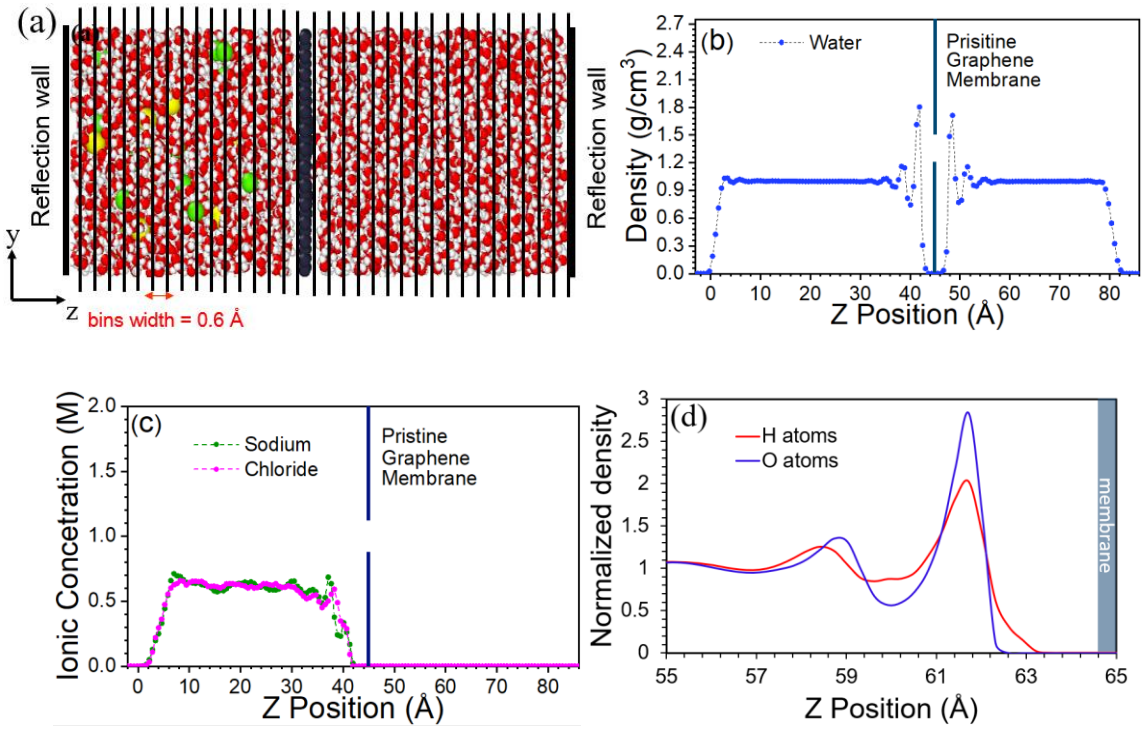

Figure. 3.2. (a) Illustration of the binning method along the z-direction of the simulation domain (b) Density distribution of water along the z-direction for a system with a pristine graphene membrane. (c) Ionic concentration distribution of sodium and chloride ions in the z-direction of the simulation domain. (d) Normalized densities of oxygen and hydrogen atoms in the vicinity of the membrane. Data were taken in the first equilibrium stage.

Flows through the membranes were created by moving the specular refection boundaries at constant speed. Different flow rates were obtained by selecting velocities of the

boundaries at 5.0 cm/s, 7.5 cm/s, and 10 cm/s. When the boundaries were moving, a pressure difference was induced between the feed and permeate sides. In order to identify

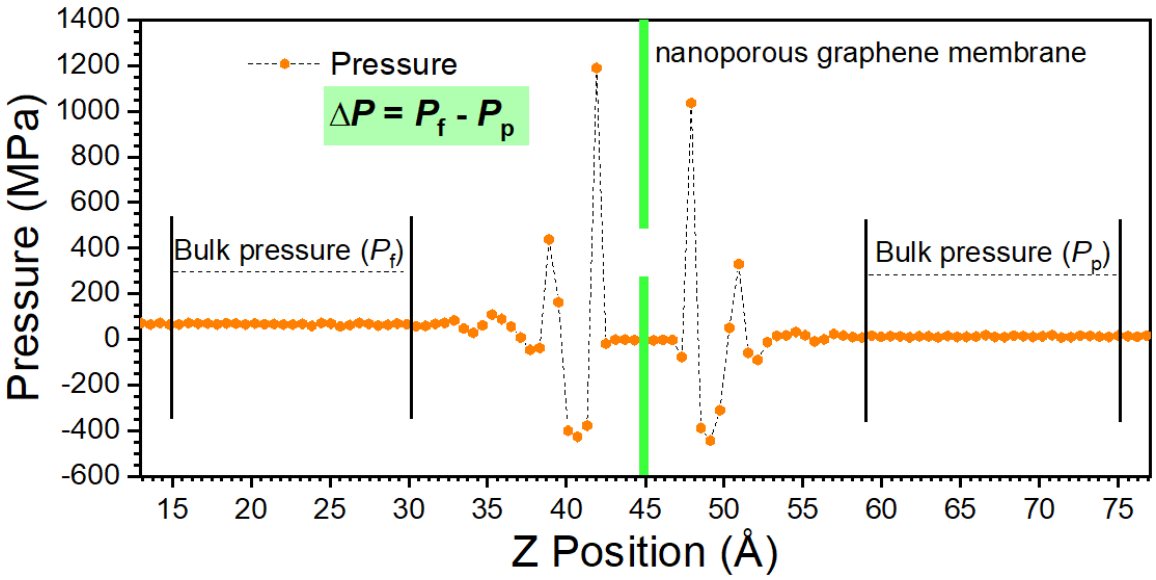

Figure. 3.3. Typical pressure distribution along the z-direction when the two reflection boundaries are moving. Bulk pressure regions in the feed and permeate sides are the average of local pressures in the defined region.

this pressure difference, bulk pressures at both sides were calculated. The bulk pressure in each side is defined as the average of the local pressure in slab bins belonging to the bulk region. The local pressure of water and salt ions in each slab bin is the average of the three normal stress components in that bin. Components of the stress tensors were calculated using Irving-Kirkwood relation and the pressure was found by averaging the diagonal components of the stress tensor in the Cartesian coordinate system.

Figure 3.3 shows variation of average normal stress in the stream-wise direction, which exhibits fluctuations near the pristine and charged membranes (only the charged membrane

case is shown for brevity). Barisik and Beskok have shown anisotropic normal stress distribution near the walls [94]. Only sufficiently away from the solid surfaces the three components of the normal stresses become equal, and the typical definition of "pressure"

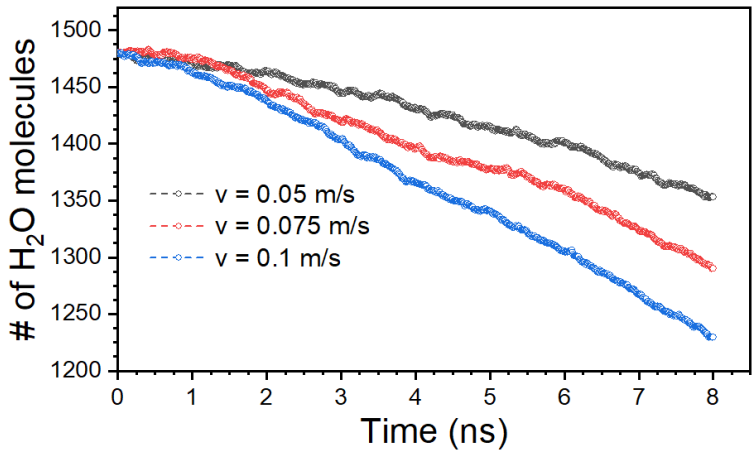

Figure. 3.4. The typical illustration for the time evolution of the number of water molecules in the feed side. The data are taken from the case with pore diameter of 11.57 Å. Volumetric flow rate of water in the desalination system was calculated using slope of data after 2 ns using Eq. (3.2).

with isotropic normal stresses is observed. As shown in **Fig. 3.3**, constant pressures are observed typically 12.0 Å from the membrane. I utilized the constant bulk pressures in the feed ($P_{\text{bulk,feed}}$) and permeate ($P_{\text{bulk,permeate}}$) sides to obtain the pressure difference as follows:

$$\Delta P = P_{\text{bulk,feed}} - P_{\text{bulk,permeate}} . \tag{3.1}$$

The number of water molecules in the feed as a function of time for different boundary velocities are shown in **Fig. 3.4** for a membrane with pore diameter of 11.57 Å. The number of water molecules in the feed side linearly decreases 2.0 ns after the boundary motion. Increased slope magnitude in the figure corresponds to higher flow rates obtained for faster

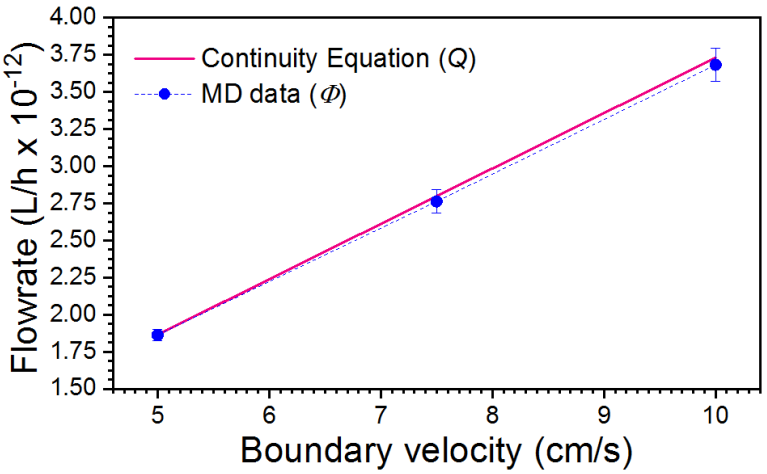

Figure. 3.5. MD volumetric flow rates of water with respect to different boundary velocities as compared to that calculated by the continuity equation (Eq. 3.3).

boundary velocity cases. I estimated the volumetric flow rate using the time rate of change of water molecules in the feed side. Since the desired flow rate is induced by specifying the boundary velocity, the flow rates for the three different pore sizes are approximately equal. The volumetric flow rates were calculated using:

$$\Phi = \dot{N} \times v_{H_2O} \ , \tag{3.2}$$

where Φ is flow rate, $\dot{N}$ is the average rate of water molecules passing through the membrane, and v_{H_2O} is the volume occupied by a water molecule, which is 2.99×10^{-23} cm^3. On the other hand, using constant boundary velocity (u) and the cross-sectional area of the moving boundary (A), the imposed volumetric flow rate (Q) through the nanoporous membrane becomes:

$$Q = A \times u \ . \tag{3.3}$$

Figure 3.5 presents variation of flow rate as a function of the imposed boundary velocity. The figure shows comparison between the MD data using Eq. (3.2) and the imposed flow rate obtained from Eq. (3.3). Good match between the predictions of two equations are observed. The minor mismatch between the two approaches can be attributed to the finite intermolecular spacing between the water molecules and compressibility of water, while hydrodynamics assumes incompressible flow. It is also attributed to the approximated volume of one water molecule. These matters render the size of the error bars.

I calculated pressure drops corresponding to different volumetric flow rates (equivalently represented by the boundary velocity) and pore diameters. **Fig. 3.6** shows that the pressure drops necessary to obtain a specific flow rate are higher for smaller pore diameters. **Fig. 3.6** also shows that the pressure drops linearly increase with the increasing flow rate. This well-known linear relationship between pressure drop and flow rate was also shown for Stokes flow and in previous studies [59, 95, 96].

It is reasonable to postulate that the pressure drop required for a specified flow rate of water through a nanopore depends on the viscosity of water, as well as the diameter and length of the pore. However, due to the extremely small thickness of a single-layer graphene membrane, which is equal to the atomic diameter of a carbon atom (1.4 Å), the effect of the pore length on pressure drop is negligible. Based on this reasoning, I applied the Buckingham Pi theorem (BPT) to establish a functional relationship between the mentioned physical quantities in this problem. Using ΔP, Φ, D_h, and μ as the notations for pressure drop, volumetric flow rate, hydraulic diameter, and dynamic viscosity, respectively, BPT results in a single Π parameter given in Eq. (3.4) as follows:

$$\Pi = \frac{\Phi\mu}{\Delta P D_h^3} \tag{3.4}$$

For each case this single Π parameter can be written as a constant C_o leading to the final functional relationship as follows:

$$\Pi = \frac{\Phi\mu}{\Delta P D_h^3} = \text{constant} = C_o \ , \tag{3.5}$$

$$\Phi = C_o \frac{\Delta P D_h^3}{\mu}. \tag{3.6}$$

This equation clearly confirms the linear relationship between flow rate and the pressure drop for a specified pore diameter. It also shows a cubic relationship between flow rate and pore diameter at a fixed pressure drop. Interestingly, Eq. (3.6) has the same form with that obtained from solving Stokes equations for a pressure-driven incompressible flow through a circular pore in an infinitely thin plate, for which C_o = 1/24 [97, 98]. In order to elucidate the value of the constant C_o in Eq. (7) based on our study, I rewrote Eq. (3.6) as $\Delta P = \left(\frac{\mu}{C_o D_h^3} \right) \Phi$. It can be seen from **Fig. 3.6** that the term $\left(\frac{\mu}{C_o D_h^3} \right)$ is the slope for the pressure-flow rate linear relationship corresponding to each specified pore diameter. Celebi and Beskok recently showed that adding salt ions into water enhances its viscosity [99]. Based on this previous study, I estimated that the viscosity value of a 0.6 M NaCl solution is in the range of 850 to 860 μPa.s for the pristine membrane case. Substituting D_h and specific viscosity values into slope of the flow rate data, I obtained a single C_o value for each pore diameter case using 30 different simulation results. I observed that the C_o values were largely unchanged between the three different pore sizes, but they have shown

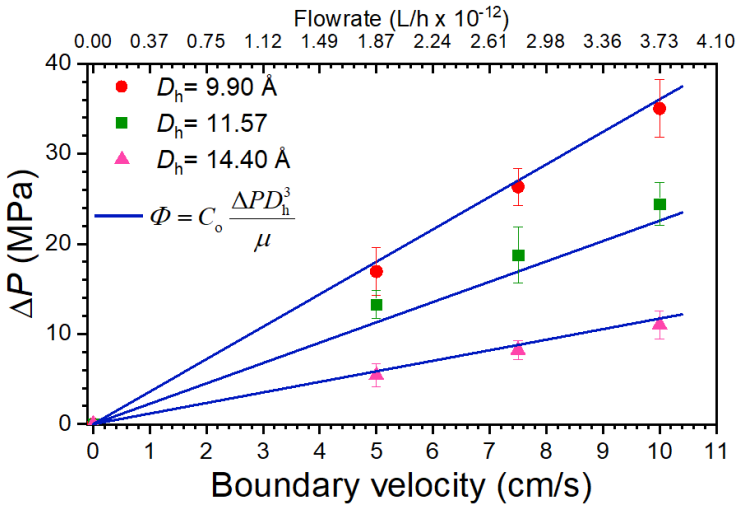

Figure. 3.6. Pressure drop versus boundary velocity for different pore diameter. The data obtained from MD simulations and from Eq. (3.6) are both presented. In Eq. (3.6), C_o=1/38 is used for all pristine membrane cases.

differences for the pristine and charged membrane cases. Obtaining the same C_o value regardless of the pore size is expected, since C_o is a coefficient induced by a geometric obstruction. Due to the atomistic thickness of the graphene nano-pores, there are no additional length-scales describing the pore effect. Using the average C_o value of the three different pore diameters I present in **Fig. 3.6** the pressure drops versus flow rate for the pristine graphene membranes. Using the previously mentioned ranges of viscosity values, C_o is approximately in the range of 1/38.62 to 1/38.17 for pristine graphene membranes. The C_o value obtained in our study is approximately one and a half times smaller than that obtained from continuum analysis (C_o = 1/24). This difference is attributed to the dominant role of vdW forces at the nanoscale, which is ignored in the continuum analysis. The dominance of vdW forces makes it more difficult for liquid particles to flow through nanoporous pores. If pore diameters are calculated based on a center-to-center method that

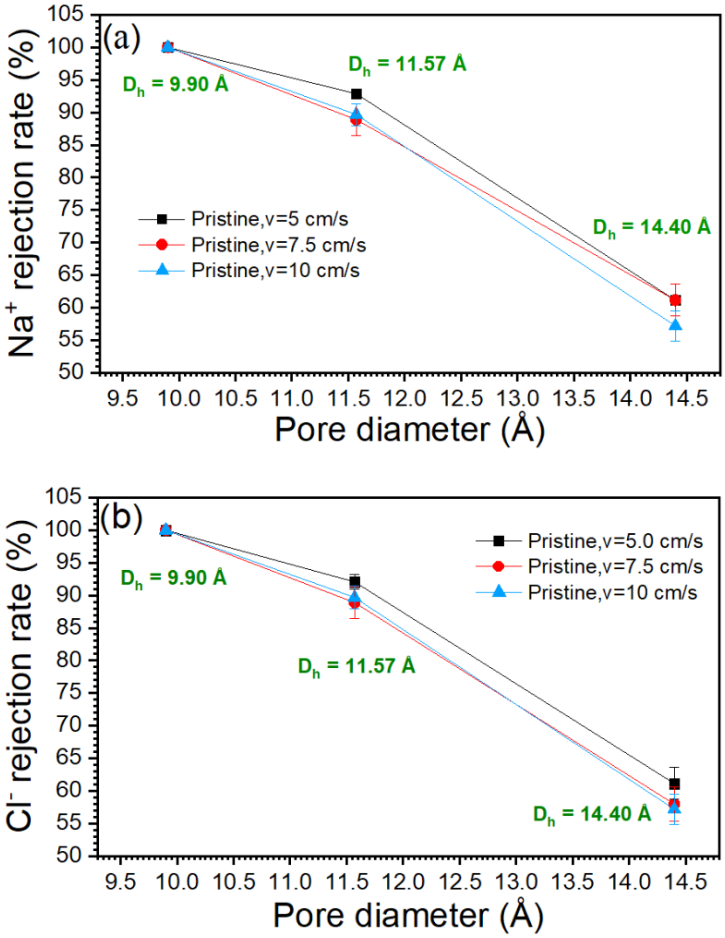

Figure. 3.7. Sodium ion rejection efficiencies for different pore diameters and boundary velocities (a). Chloride ion rejection efficiencies for different pore diameters and boundary velocities (b).

averages the distance between any two atoms on the line containing the center point of the circle, pore diameter values are 10.28 Å, 12.04 Å, and 14.76 Å. The corresponding C_o value is approximately in the range of 1/42.83 to 1/42.33. As shown in **Fig. 3.6**, the predictions of pressure drop values corresponding to the different water flow rates for each pore diameter are in good agreement with the MD data. This result verifies the established equation for predicting the critical relationship between water flow rate and pressure drop

in RO desalination systems. Eq. (3.6) with the reported C_o values can be used for future studies and engineering design.

The trade-off between water flow rate and salt rejection efficiency is always the critical concern in designing water desalination systems. It is shown in the previous section that we can obtain the same flow rate with smaller pressure drop and thus the required pumping power if larger graphene nanopore diameters are used. However, selecting a critical nanopore diameter in order to achieve an acceptable salt rejection efficiency along with a reasonable flow rate is very significant. In our study, salt rejection efficiency is defined as the ratio of the number salt ions remaining in the feed side to the total initial number of salt ions in the feed side after the entire simulation time. It is shown in **Fig. 3.7** that a rejection efficiency of 100% for both sodium and chloride ions can be attained if a pristine graphene membrane with a nanopore diameter of 9.90 Å is used. Our results show that I can obtain a rejection efficiency of 100% with a pore diameter even larger than 5.5 Å as identified by Cohen-Tanugi *et al*. [32] or 7.5 Å as claimed by Konatham *et al.* [33]. It is interesting that the pore diameter definition in these two studies is unclear, but the method of creating the nano-pore in Konatham *et al.*[33] is similar to our work. Importantly, as introduced in the MD details section, I used *ten* different initial conditions to obtain the results, where Na^+ and Cl^- are distributed in the feed side differently. Hence, I present here a better statistically converged data, compared to the previous studies, in which an equivalent number of ions but a smaller number of initial conditions were used. In addition, I found that the applied pressure needed for obtaining an equivalent water flow rate is approximately 52% lower to that shown by Cohen-Tanugi *et al.*[96] whereas perfect rejection efficiency is still maintained. The discrepancy can also be attributed to the differences in simulation

methodologies such as the way of simulating pressure-driven flows and the use of different force fields **Fig. 3.7** also indicates that the rejection efficiencies of sodium and chloride ions decrease with increasing pore diameter. It is also seen that for each of the selected pore diameters, basically rejection efficiency decreases with increasing boundary velocity but this effect is insignificant for selected range of flow rates. In other words, for each of the specified pore diameters, the obtained flow rates can be as high as 3.73×10^{-12} L/h-pore whereas rejection efficiency is largely unchanged. If a pore diameter of 9.90 Å is used, the corresponding ideal pore density is $1/A_p = 127.25 \times 10^{12}$ pore/cm^2. Based on the maximum porosity for a sustainable nanoporous graphene sheet of 35.0% [28], the obtained water flux can be as high as 163.2 L/h-cm^2 with a required pressure drop of 35.02 MPa and a salt rejection efficiency of 100%. This high flux of water associated with the perfect rejection efficiency is consistent with that found by Surwade *et al.* using plasma-etched single-layer nanoporous graphene membranes [22].

3.3. Conclusions

In this Chapter, I performed an in-depth investigation of transport of saltwater across pristine graphene membranes using a new approach in modelling pressure-driven flows with molecular dynamics simulations. Using moving specular reflection boundaries flow rate was specified and pressure drop was calculated. Our simulation method was verified by showing that the volumetric flow rates of water through the membranes from MD data are in good agreement with those calculated from the continuity equation, and the well-known linear relationship between pressure drop and water flow rate was observed. I found

that the pressure drop and therefore the required power consumption for having an equivalent water flow rate through the graphene membranes decreases with increasing the pore diameter. A functional relationship between the volumetric flow rate, pressure drop, pore-diameter and the dynamic viscosity of saltwater was developed using the Buckingham Pi theorem and the MD simulation data. The resulting equation successfully predicts the relationship between the volumetric flow rate through a nanoporous graphene membrane and the corresponding pressure drop for a specified pore diameter. This relation can be used for future studies or in designs of RO water desalination systems using pristine nanoporous graphene membranes. Further investigation of salt ion rejection showed that salt rejection efficiency is dependent on the pore diameter of the graphene membranes. MD simulations have shown that water flux as high as 163.2 L/h-cm^2 with perfect salt rejection efficiency can be obtained using a pristine graphene membrane with the pore diameter of 9.90 Å. Finally, the current simulation domain is chosen to create steady flow that mimics pressure-driven flow processes. This creates accumulation of salt ions in the feed side for any given rejection efficiency, creating time-dependent ion concentration. Therefore, the current results show average ionic transport when the feed volume is reduced approximately by 25%. Running the simulations further will reduce the presented rejection efficiencies. In practice, it may be necessary to flush the feed side to eliminate these unfavorable effects.

Chapter 4

CHARGED NANOPOROUS GRAPHENE MEMBRANES FOR WATER DESALINATION

Water desalination using positively and negatively charged single-layer nanoporous graphene membranes are investigated using molecular dynamics (MD) simulations. Pressure-driven flows are induced by the motion of specular reflection boundaries with a constant speed, resulting in a prescribed volumetric flow rate. Simulations are performed for a 14.40 Å hydraulic pore diameter membrane with four different electric charges distributed on the pore edges. Salt rejection efficiencies and the resulting pressure drops are compared with the previously obtained base-line case of 9.9 Å diameter pristine nanoporous graphene membrane, which exhibits 100% salt rejection with 35.02 MPa pressure drop at the same flow rate. Among the positively charged cases, $q = 9e$ shows 100% and 98% rejection for Na^+ and Cl^- ions respectively, with 35% lower pressure drop than the reference. For negatively charged pores, optimum rejection efficiencies of 94% and 93% are obtained for Na^+ and Cl^- ions for the $q = -6e$ case, which requires 60.6% less pressure drop than the reference. The results indicate the high potential of using charged nanoporous graphene membranes in reverse osmosis (RO) desalination systems with enhanced performance.

4.1.Simulation Settings and Methods

The schematic of the simulation domain is shown in **Fig. 4.1**, which consists of a feed reservoir on the left and a permeate reservoir on the right. A nanoporous graphene membrane with a hydraulic pore diameter of 14.40 Å separates the two reservoirs. The hydraulic diameter is defined as $D_h = 4A_h / p$, where the pore area (A_h) is the empty space surrounded by the pore edge and the pore circumference (p) is obtained by calculating the distance between all carbon atoms on the pore edge. Hydraulic diameter is used due to the hexagonal structure of graphene, which causes the noncircular structure of the pore. Both ends of the simulation domain are bounded with specular reflection boundaries which are initially located at z = 0.0 Å and z = 82.34 Å, respectively. The nanoporous graphene membrane is fixed at z = 45.18 Å.

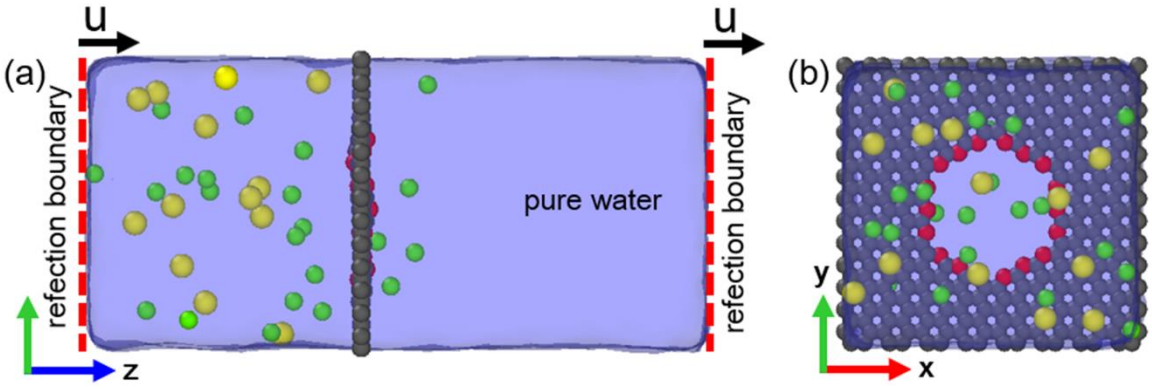

Figure 4.1 Schematic side-view of the simulation domain. Sizes of the sodium (yellow) and chloride (green) ions are exaggerated for better visualization. (b) Normal view of the simulation domain at the membrane. Charged carbon atoms belonging to the pore edge are shown in red.

The SPC/E model was chosen for water molecules as discussed in Chapter 3. A truncated LJ 12-6 potential was used to model van der Waals (vdW) interaction, and it was utilized to describe the intermolecular interactions of salt ions, oxygen atoms in water molecules, and carbon atoms in graphene membranes. A cut-off distance of 10.0 Å was used to truncate intermolecular forces. The long-range interactions in LJ terms were compensated by the tail correction method. Interaction parameters between the oxygen atoms were obtained from the SPC/E model [81]. Interaction parameters between oxygen atoms and carbon atoms were selected based on the empirical data obtained from contact angle measurements [83]. The AIREBO potential was used to model the in-plane interactions between the carbon atoms of the graphene membranes [76]. Any atomic species with charge was coupled with Coulombic interactions. In our system, the dissolved salt ions were represented by sodium ions (Na^+) and chloride ions (Cl^-) with assigned charges of q_{Na} = 1.0e and q_{Cl} = -1.0e, respectively. The vdW interaction parameters of sodium and chloride ions in aqueous solutions were taken from GROMACS force field, which was based on quantum calculations and have been shown to reproduce reasonable transport properties for ionized water [84]. **Table 3.1** summarizes all interaction parameters used in computations. The PPPM method was used to correct the long-range electrostatic interactions between all charged atomic species [85]. The VERLET algorithm was used to integrate Newton's equations of motion with a simulation time step of 1.0 fs. All the simulations were performed using LAMMPS [61].

Initially the feed reservoir contains 1500 water molecules while the permeate reservoir contains 1200 water molecules. The smaller number of water molecules in the permeate reservoir was used to save computational cost while a defined thermodynamic state of

water was still preserved. Electrical charges were uniformly distributed on the carbon atoms located at the pore edges with total net charges of ±3*e*, ±6*e*, ±9*e*, and ±12*e* as commonly practiced in MD literature [38]. The current nano-pore has 18 carbon atoms around the edge. Therefore, the total charge cases of ±3*e*, ±6*e*, ±9*e*, and ±12*e* require ±0.167*e*, ±0.333*e*, ±0.5*e*, and ±0.667*e* charge per carbon atom (on average charge), respectively. The charge cases of ±0.5*e* and ±0.667*e* per carbon atom are considered rather high from experimental viewpoint. However, it is also important to add that charge distribution in experiments could happen around the periphery of the pore at a larger area, which can reduce the number of required charges per carbon atom. For example, for the cases of ±9*e*, the charge per carbon atom can be reduced to ±0.214*e* if the carbon atoms in the pore periphery right next to the pore edge are also included. The bulk concentration of salt (NaCl) in the feed reservoir was 0.6 M to represent seawater. For each simulation associated with a specified total number of charges on the pore, the number of salt ions is changed to maintain electrical neutrality conditions in the simulation system. For the positively charged cases, the feed reservoir contains 13 Na^+ - 16 Cl^- ions, 13 Na^+ - 19 Cl^- ions, 13 Na^+ - 22 Cl^- ions, and 13 Na^+ - 25 Cl^- ions, corresponding to the cases of 3*e*, 6*e*, 9*e*, and 12*e*, respectively. For the negatively charged cases, the feed reservoir contains 16 Na^+ -13 Cl^- ions, 19 Na^+ - 13 Cl^- ions, 22 Na^+ - 13 Cl^- ions, and 26 Na^+ - 14 Cl^- ions, corresponding to the cases of -3*e*, -6*e*, -9*e*, and -12*e*, respectively.

MD simulations require three distinct simulation stages consisting of (a) equilibrium MD with graphene sheet, (b) equilibrium MD with open graphene nanopores, and (c) non-equilibrium MD with pressure-driven flow. In stage (a), all liquid molecules were assigned initial conditions using Maxwell-Boltzmann velocity distribution at 300 K. Equilibrium

MD simulations were performed for the two reservoirs by closing the nanopore with a plug containing the carbon atoms originally belonging to the graphene membrane, while NVT (constant number of molecules, volume, and temperature) ensemble with a Nose-Hoover thermostat was applied to retain both reservoirs at 300 K. Closing the nanopore with a plug separated the two reservoirs and the thermodynamic states of water in both sides were fixed at 0.997 g/cm^3 and 300 K. This state was equilibrated for at least 50 ns for all the different applied charge cases. The pore plug was opened in stage (b) and the system was relaxed for at least 100 ns until the bulk pressures in the feed and permeate reservoirs equilibrate, while the entire simulation domain was kept at 300 K. The specular reflection boundaries are still fixed in their initial positions in this stage. Finally, in stage (c) non-equilibrium MD simulations were used to induce pressure-driven flow through the charged graphene nanopores by moving the two specular refection boundaries with identical velocities in the stream-wise (z) direction, while the graphene membrane was fixed in its place. Details of this method were discussed in Chapter 3 as well as in Nguyen and Beskok [100]. This approach eliminates possible errors caused by applying constant forces on rigid pistons made from single-layer graphene sheets or applying constant forces on water molecules. In all simulations, the graphene membranes could vibrate thermally and were kept at 300 K, enabling modelling of their mechanical deformation and wetting characteristics. Previous studies using membranes with fixed atoms (cold wall model) showed influence of their approach on water and ionic salt distributions near the surfaces, which affected transport of saltwater through the membranes [87]. I imposed the velocity of the specular refection boundaries as 10 cm/s, which results in a volumetric flow rate of 3.73×10^{-12} L/h-pore. This is the largest volumetric water flow rate that resulted in 100% salt rejection

shown in Chapter 3 as well as Nguyen and Beskok [100]. Data acquisition for transport of water molecules and salt ions was started immediately after the motion of the specular reflection boundaries and lasted 10.0 ns. The computational domain was divided into slab bins along the *z*-direction with a slab size of 0.6 Å to examine variations in the streamwise direction.

The small computational volume requires limited number of salt ions, creating challenges in reporting the salt rejection efficiencies and bin averaged values. This deficiency was addressed by using *ten* different MD simulations that started off at different equilibrium conditions, selected with at least 1.0 ns time-difference from each other. Our approach ensures that each simulation begins with random positions of the salt ions. Therefore, all ten simulations are statistically different from each other. Uncertainties associated with pressure drop and rejection efficiencies were estimated by calculating the standard deviation of data for each applied charge case. With four different total applied charges on each membrane polarization, a total of 80 different MD simulations were performed, resulting in significant reductions in statistical fluctuations of the presented data.

4.2.Results and Discussion

4.2.1. Positively Charged Nanoporous Graphene Membranes

Figure 4.2 shows the distributions of sodium (Na^+) and chloride (Cl^-) ions in the streamwise z-direction for the charged membranes with different total applied charges in stage (a). For each case of total applied charge, the nanopore was initially blocked to fix

the thermodynamic state of water at 0.997 g/cm3 and 300 K. The concentrations of Na^+ and Cl^- ions were preserved at approximately 0.6 M in the bulk region sufficiently away from the graphene membrane regardless of the total charge fixed on the pore edge. However, Cl^- ions accumulate near the membrane whereas Na^+ ions are excluded. Due to Coulombic forces, counter-ions (Cl^-) are attracted to the positively charged nanopores, while co-ions (Na^+) are repelled. This establishes a peak of Cl^- ions near the membrane, forming an electric double layer (EDL) to balance the charges on the nanopore.

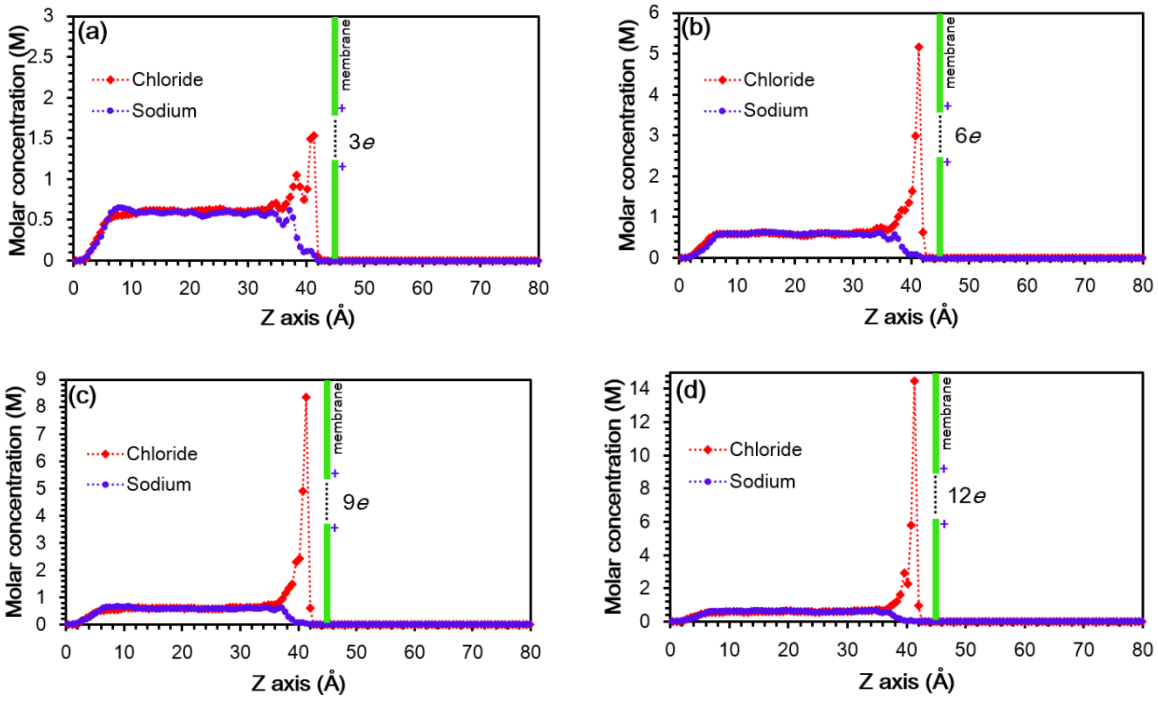

Figure 4.2. Distributions of sodium and chloride ions in the z-direction for positively charged graphene membranes with 3*e* (a), 6*e* (b), 9*e* (c), and 12*e* (d) total applied charge. At the first equilibrium state (stage *a*), the nano-pore is blocked, and the thermodynamic state of water is fixed at 0.997 g/cm^3 and 300 K in the feed and permeate reservoirs. Due to the use of slab-bins in z-direction, the presented ionic distributions are averaged across the entire membrane and pore areas.

Figure 4.3 shows salt ion distributions along the *z*-direction in stage (b) where the nanopore is open, but specular refection boundaries are not moved. Interestingly, some of the Cl^- ions accumulating near the graphene membrane in stage (a) pass through the nanopore and form another concentration peak on the permeate side of the nanoporous graphene membrane.

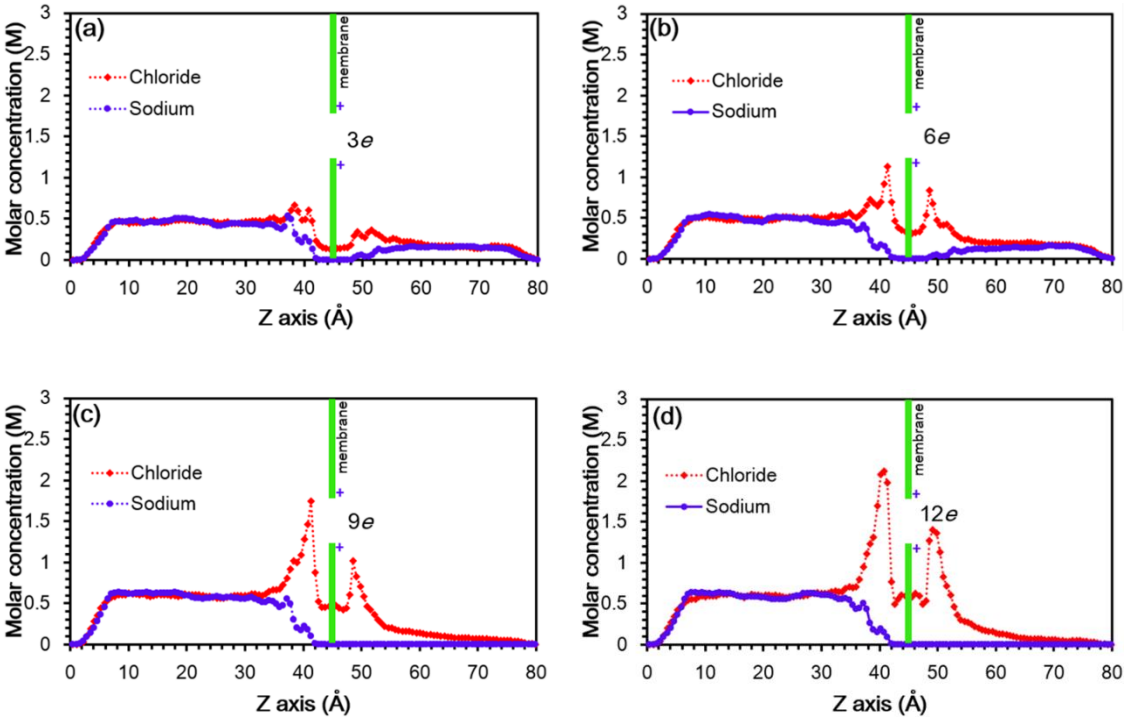

Figure 4.3. Distributions of sodium and chloride ions in the streamwise (z) direction for 3*e* (a), 6*e* (b), 9*e* (c), and 12*e* (d) total applied charge at the second equilibrium state (stage b, 100-120 ns after opening the pore) where the nano-pore is open but there is zero net flow (i.e., the specular reflection boundaries are not moving). Due to the use of slab-bins in z-direction, the presented ionic distributions are averaged across the entire membrane and pore areas.

This results in a reduction in the peak of the Cl^- ions on the feed side. It should be also noted that in the $q = 3e$ and $q = 6e$ cases, some of the Na^+ ions also pass through the nanopore along with the Cl^- ions. In the permeate reservoir, these Na^+ ions are pushed away

from the nanoporous graphene membranes and form another bulk flow region with the mobile Cl^- ions. Leakage of both Cl^- and Na^+ ions in these two cases leads to the reduction in the bulk concentration of salt ions in the feed reservoir. However, starting from the case of $q = 9e$, Na^+ ions do not pass through the nanopore and the bulk salt concentration of 0.6 M is still conserved in the feed reservoir. This is attributed to the strong repulsion of Na^+ ions by the large positive charges fixed on the pores, whereas repulsion of positive charges for $q = 3e$ and $q = 6e$ cases is not strong enough. While some of the Cl^- ions pass through the nanopore and reside on the permeate side of the membrane, some of them accumulate in the pore region. It is seen in **Fig. 4.3** that the concentration of Cl^- ions inside the pore region is greater than zero and increases with the applied charge. In order to elucidate localization of Cl^- ions inside the pore region, I show in **Fig. 4.4** Cl^- ion distributions at the *z*-location of the nanoporous graphene membrane for different applied charges. I found that the Cl^- ions reside around the pore edge and the degree of localization increases with increasing the total applied charge fixed on the pore edge. Crowding of Cl^- ions around the pore edge is sustainable and more profound in the $q = 9e$ and $q = 12e$ cases, while the ions are distributed randomly around the pore for the $q = 3e$ case.

In stage (c), pressure-driven flows were created through the charged nanopores by the motion of specular reflection boundaries. Variation of the pressure drop as a function of the applied charge at the prescribed flow rate is also investigated. **Figure 4.5(a)** shows a typical pressure distribution in the *z*-direction between the two moving specular refection boundaries. Data for the $q = 6e$ case is shown for brevity. The local pressure of water and salt ions in each slab bin is the average of the three normal stress components in that bin. The stress tensor components were calculated using Irving-Kirkwood relation introduced

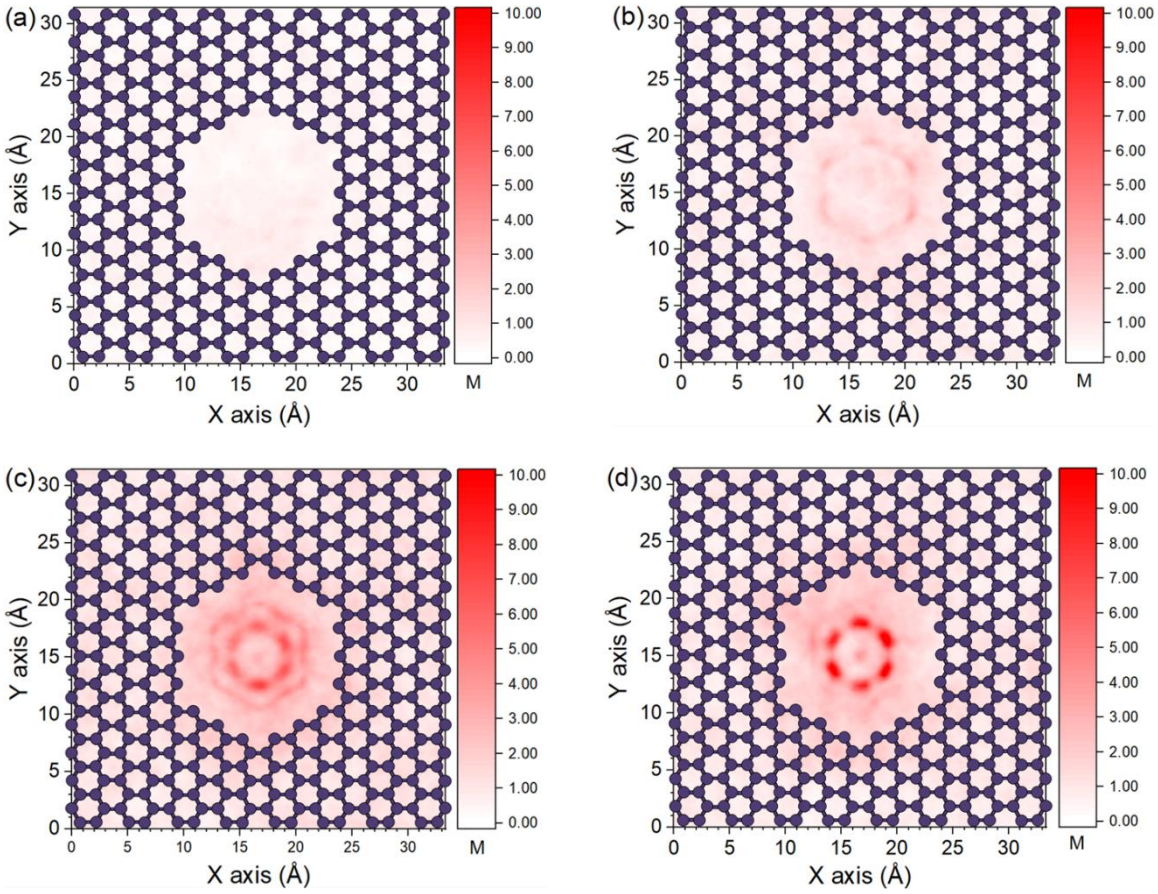

Figure 4.4. Distributions of chloride ions in the plane containing the positively charged nanoporous graphene membranes with 3*e* (a), 6*e* (b), 9*e* (c), and 12*e* (d) total applied charge at the second equilibrium state (stage b), where the nano-pore is open but there is zero net flow. Contour colors show Cl^- concentration in M.

in Chapter 2. The well-known pressure fluctuation near the nanoporous graphene membranes is observed. It was shown previously that anisotropic normal stresses exist near the walls, whereas the three components of the normal stresses become equal sufficiently far away from the membrane and create the bulk pressure [94, 100-102]. The pressure drop is defined as the pressure difference between the bulk pressures in the feed and permeate reservoirs. The bulk pressure in each reservoir is defined as the average of the local

pressures in slab bins belonging to each bulk region. **Figure 4.5(b)** shows variation of pressure drop as a function of the applied charge, while the data for $q = 0e$ is from Chapter 3. The pressure drop increases nonlinearly with the increased applied charge at the specified flow rate. This interesting phenomenon is attributed to the bulk viscosity enhancement of water due to the charges on the pores [99, 103-105] In addition, it should be noted from **Fig. 4.4** that increasing the applied charge increases localization of Cl^- ions in the pore region. Water molecules in the feed reservoir need to overcome crowding of the Cl^- ions in the middle of the pore, resulting in increased pressure drop at the specified flow rate.

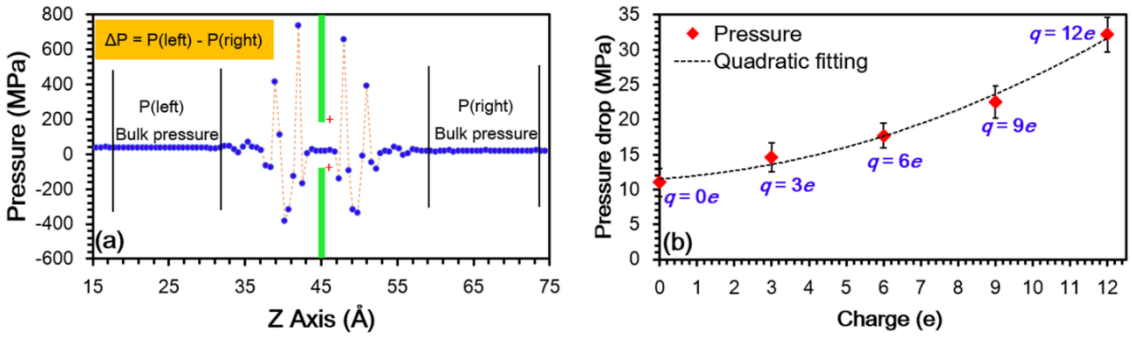

Figure 4.5 Pressure distribution along the *z*-direction for q=6e case (a). Variation of pressure drop as a function of the total surface charge (b). Data for $q = 0e$ is from Chapter 3. Standard deviation in the pressure drop was calculated using data from *ten* different simulations with statistically different initial conditions.

Figure 4.6 shows salt ion distribution in the *z*-direction at the end of flow simulations (10 ns of boundary motion in stage *c*). The following two important phenomena are observed: (1) Cl^- ions in the permeate reservoir reside near the positively charged membrane despite

the steady water flow, and (2) salt concentration in the feed reservoir increases with time, exhibiting higher values than its initial value shown in **Fig. 4.3**. For the $q = 3e$ and $q = 6e$ cases, in addition to the transport of some Cl^- and Na^+ ions through the membranes in stage (b), additional Cl^- and Na^+ ions flow to the permeate reservoir with water. Although some Cl^- ions are in the vicinity of the membrane, a noticeable amount of Cl^- ions along with

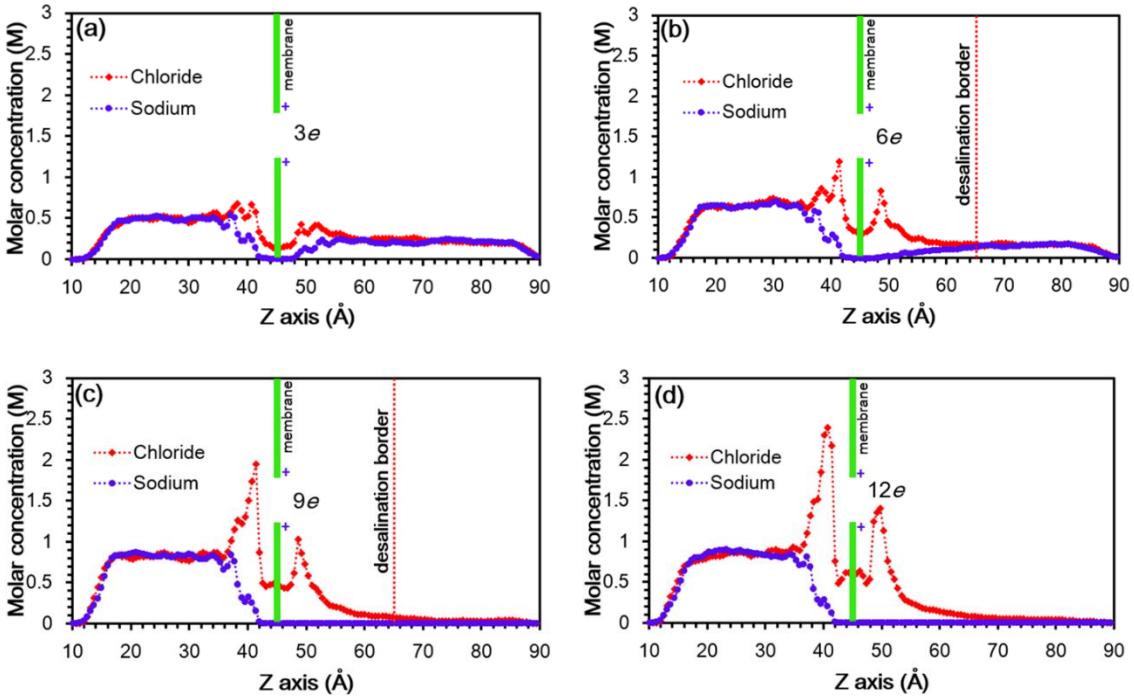

Figure 4.6. Distributions of sodium and chloride ions in the streamwise (z) direction for $3e$ (a), $6e$ (b), $9e$ (c), and $12e$ (d) total applied charge at the end of flow simulations (t=10 ns in stage c). Salt concentration in the permeate reservoir is dominant between the charged membrane and desalination border located 20.0 Å behind the membrane. Desalination border is shown in figures (b) and (c). Due to the use of slab-bins in z-direction, the presented ionic distributions are averaged across the entire membrane and pore areas.

Na^+ ions pass through the membrane and create a visible bulk salt concentration in the permeate reservoir. On the other hand, salt concentration in the feed reservoir increases due to the decrease in the volume, while the number of salt ions transported to the permeate

reservoir is insufficient to keep salt concentration in the feed reservoir at 0.6 M. Especially, for the $q = 9e$ and $q = 12e$ cases, zero Na^+ ions pass through the charged membrane, whereas only a few of Cl^- ions transport with the flow. Even after passing through the membrane, the majority of Cl^- ions in the permeate reservoir reside at the membrane-water interface and leave the permeate bulk regions with almost zero salt concentration. In addition, the Cl^- concentrations inside the pore region for all four charge cases are largely unchanged before, during and after the flow due to stable localization of Cl^- ions near the pore edges. These interesting and important phenomena bring a novel viewpoint to the rejection of salt ions through charged nanoporous graphene membranes. I defined a "desalination border" at a location approximately 20.0 Å away from the charged membrane, which is the onset of the permeate bulk region as shown in **Fig. 4.6(b)**. Counter-ions concentrate, and co-ions are depleted in the region between the charged membrane and desalination border, where ionic distribution is not similar to the electric double layer in the feed side of the charged membrane.

In order to assess membrane effectiveness, salt rejection efficiency was previously defined as the ratio of the number of salt ions remaining in the feed reservoir to the total number of salt ions as in Chapter 3. I denoted this as "viewpoint one." I also define a new salt rejection efficiency as the ratio of the number of salt ions remaining in the volume constrained by the left specular reflection boundary and the desalination border to the total number of salt ions, and named this as "viewpoint two". **Figure 4.7** shows the salt rejection efficiencies for Na^+ and Cl^- ions based on these two definitions at the end of flow simulations (i.e., 10 ns in stage *c*). The Na^+ ion rejection increases with increasing positive charges on the pore. This is attributed to the increase in Coulombic repulsion of the positive

charges acting on the Na^+ ions. In addition, there is not much difference in the rejection efficiencies of Na^+ ions based on the two different viewpoints. This is understandable because as soon as a Na^+ ion passes through the charged membrane, it is pushed away from the membrane due to the Columbic interactions with the positive charges on the pore and due to the water flow. The Na^+ ion passing through the nanopore continues to flow downstream and passes through the desalination border. Therefore, the remaining number of Na^+ ions in front of the nanoporous graphene membrane and that in front of the defined desalination border are very similar. Especially, starting from the $q = 9e$ case, no Na^+ ions pass through the charged membrane, so that 100% rejection of Na^+ ions is obtained using both viewpoints. Interestingly, the rejection of Cl^- ions slightly increases as more positive charges are put on the pores for viewpoint one. It is observed that the increase in total positive charges on the pore causes more Cl^- ions to steadily gather in front of the membrane. This leads to the increase in the percentage of the remaining Cl^- ions in the feed reservoir. However, the rejection efficiency of Cl^- ions based on viewpoint two is much higher than those of the viewpoint one and shown to increase with increasing the total applied charge. This is attributed to the stable concentration of Cl^- ions in the pore region and at the membrane-water interface. As more charges are put on the pore edge, the additional Cl^- ions passing the membrane are accumulated onto the membrane-water interface in front of the desalination border but not flow far downstream. Meanwhile, the localization of Cl^- ions in the pore region is still reserved. This leads to the increase in the rejection efficiency of Cl^- ions. Especially, in the $q = 9e$ case, the rejection efficiency of Cl^- ions is approximately 98%, whereas that of Na^+ ion is 100%. Interestingly, the pressure drop associated with this case is approximately 22.7 MPa, which is 35% lower than that in

the case of 9.9 Å pore diameter pristine graphene membrane with 100% salt rejection efficiency [100]. Although I obtained a similar result for salt rejection efficiency for the *q*

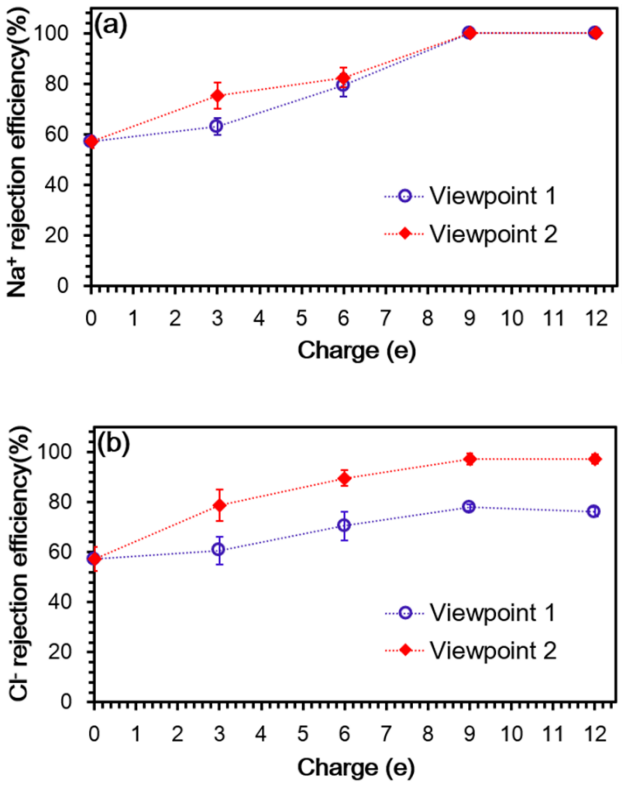

Figure 4.7. Salt rejection efficiency for sodium (a) and chloride (b) ions as a function of the total positive applied charge obtained at the end of flow simulations (t=10 ns in stage c). Data for q=0e is from Chapter 3. Standard deviation was calculated using data from ten different simulations with statistically different initial conditions. The salt rejection efficiencies are shown using viewpoint one based on the ions in permeate reservoir, and viewpoint two based on the ions behind the desalination border.

= 12e case, the required pressure drop is approximately 33.2 MPa, which is comparable to the case of 9.9 Å pore diameter pristine graphene membrane. Therefore, q = 9e is the optimal choice for enhancing the performance of RO water desalination systems for the specified high flow rate. Thus, a positively charged nanoporous graphene membrane with

a hydraulic pore diameter of 14.4 Å and total applied charge of 9*e* per pore is an excellent alternative for pristine nanoporous graphene membranes with a pore diameter of 9.9 Å at the same prescribed flow rate, resulting in very high salt rejection with 35% reduction in the required pressure drop.

4.2.2. Negatively Charged Nanoporous Graphene Membranes

Similar to the positively charged cases, all four negatively charged nanoporous graphene membranes (q = -3*e*, -6*e*, -9*e*, and -12*e*) were first blocked to fix the thermodynamic state of water at 0.997 g/cm^3 and 300 K. **Figure 4.8** shows Na^+ and Cl^- ion distributions along the *z*-direction at this state. The Na^+ and Cl^- concentrations in the feed reservoir were preserved at approximately 0.6 M in the bulk regions regardless of the total applied charge. Similar to the positively charged cases, I observed accumulation of the counter-ions (Na^+) near the negatively charged membrane, whereas the co-ions (Cl^-) are repelled, forming an EDL on the feed reservoir side of the membrane. I also observed the increase of counter-ion (Na^+) density peak with the increased total applied charge. Interestingly, starting from the q = -9*e* case, co-ions (Cl^-) accumulate near the peak of the counter-ions as shown in the insets of **Fig. 4.8(c)** and **Fig. 4.8(d).** This is due to excessive adsorption of counter-ions at the Stern layer, leading to a larger co-ion charge density than the counter-ion charge density in the diffuse layer [106]. This phenomenon is known as charge inversion, and it was previously reported for negatively charged surfaces with large surface charge densities [107-109].

Figure 4.9 shows the salt ion distributions in the *z*-direction in stage (b) where nanopores are opened, but the specular reflection boundaries are not moved. Similar to the positively charged cases, some of the counter ions (Na^+) accumulating near the membrane in stage (a) go through the nanopore, forming a concentration peak on the permeate side of the membrane. This leads to a reduction in the concentration peak of the Na^+ ions on the feed side and eliminates charge inversion for the q = -9e and q = -12e cases. The excessive co-

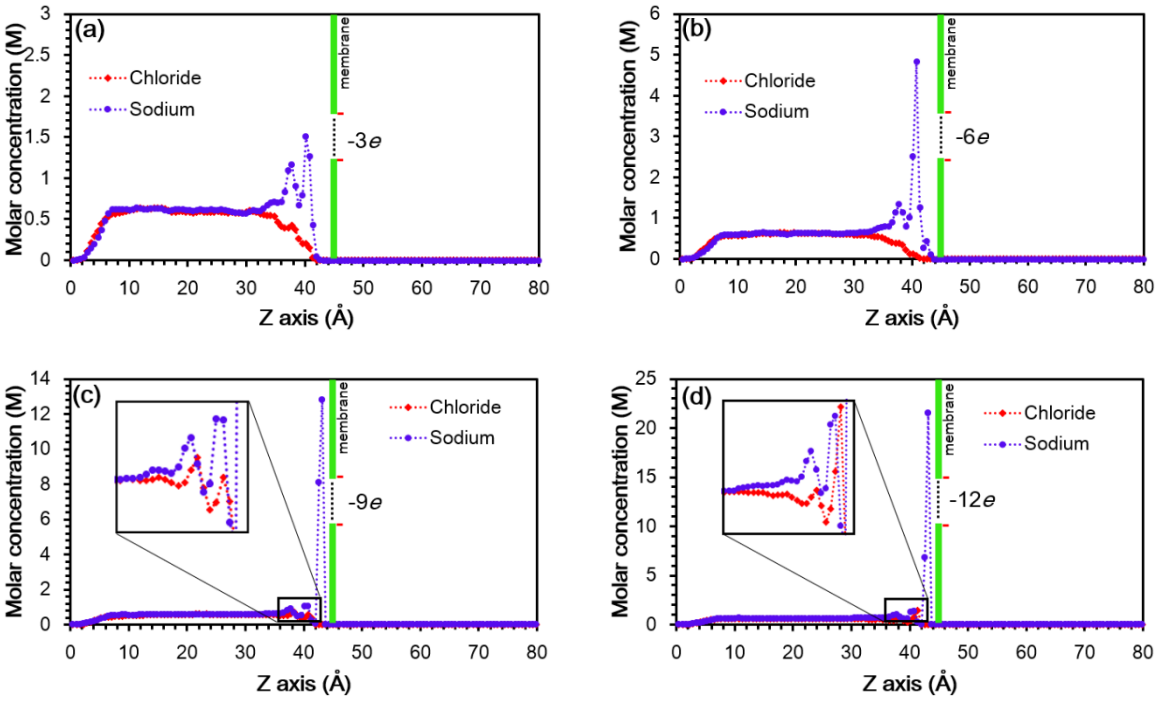

Figure 4.8. Distributions of sodium and chloride ions in the streamwise z-direction for negatively charged graphene membranes with -3*e* (a), -6*e* (b), -9*e* (c), and -12*e* (d) total applied charge. At the first equilibrium state (stage a), the nano-pore is blocked, and the thermodynamic state of water is fixed at 0.997 g/cm^3 and 300 K in the feed and permeate reservoirs. Due to the use of slab-bins in z-direction, the presented ionic distributions are averaged across the entire membrane and pore areas.

ions (Cl^- ions) in the diffuse layer observed before opening the pore leak through the membrane along with the counter-ions (Na^+ ions). In addition, some counter-ions (Na^+)

accumulate in the pore region similar to the positively charge membrane cases. Interestingly, in the q = -9e and q = -12e cases, counter-ions (Na^+) are located closer to the membrane and more in the pore region as compared to the distributions of counter-ions (Cl^-) in the positively charged membrane cases with equivalent magnitude of total applied charges.

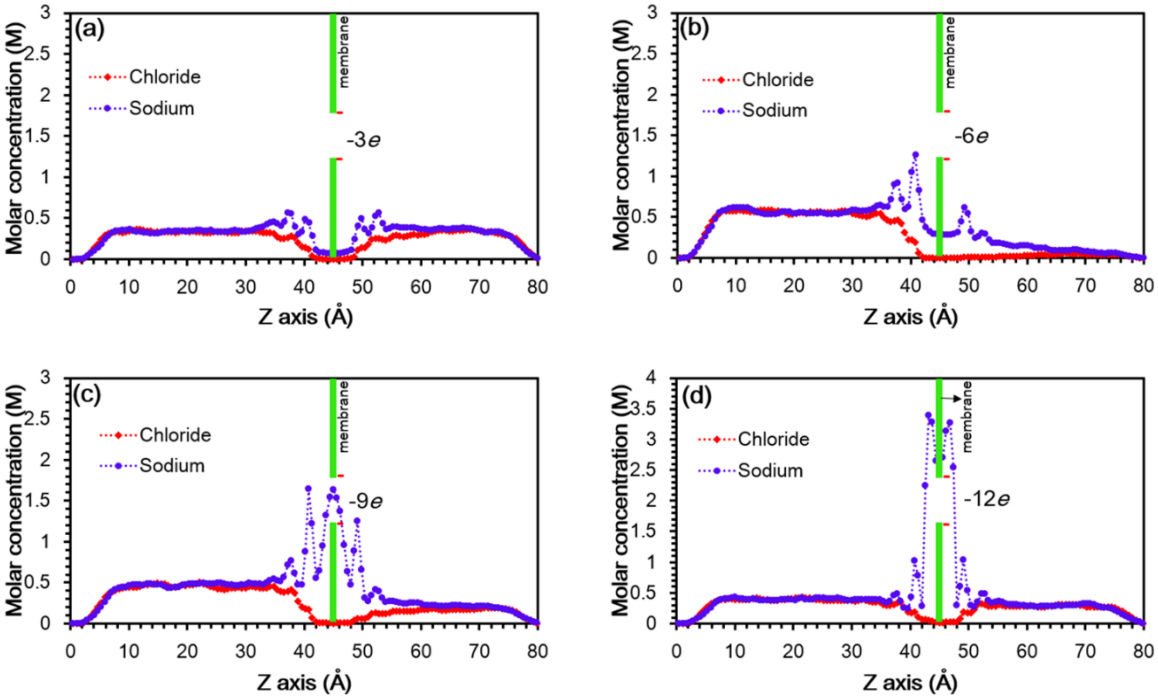

Figure 4.9. Distributions of sodium and chloride ions in the streamwise (z) direction for -3e (a), -6e (b), -9e (c), and -12e (d) total applied charge at the second equilibrium state (stage b) where the nano-pore is open but there is zero net flow (i.e., specular reflection boundaries are not moving). Due to the use of slab-bins in z-direction, the presented ionic distributions are averaged across the entire membrane and pore areas.

I present in **Fig. 4.10** the Na^+ ion distribution in the plane containing the negatively charged membrane for different applied charge cases**.** The Na^+ ions reside around the pore edge and the degree of localization increases with increased total applied charge. However, it is

interesting that while the Na^+ ions are located in the middle of the pore in the q = -6e case, the Na^+ ions are pulled closer the pore edge in the cases of q = -9e and q = -12e, decreasing crowding of Na^+ ions at the middle of the pore. This is different from the q = 9e and q =

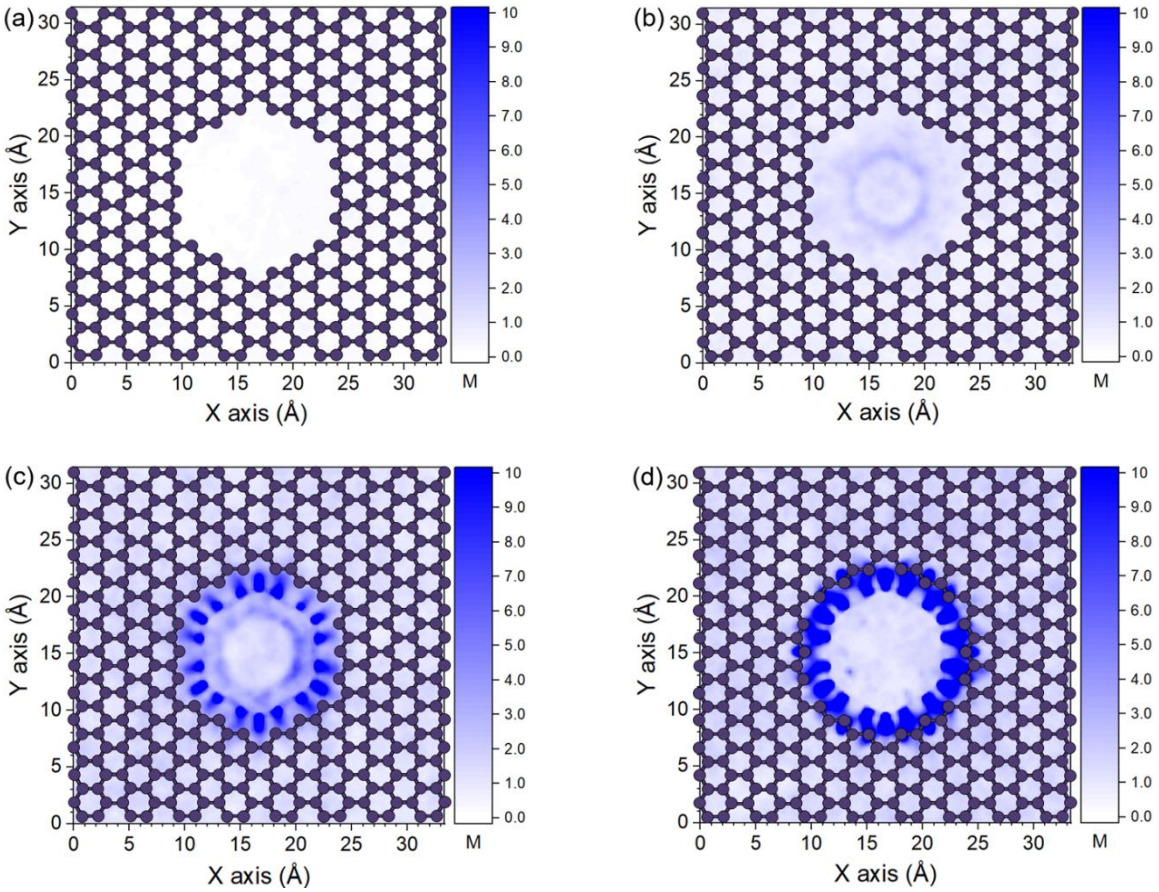

Figure 4.10. Distributions of sodium ions in the plane containing the negatively charged nanoporous graphene membranes with -3e (a), -6e (b), -9e (c), and -12e (d) total applied charge at the second equilibrium state (stage *b*), where the nano-pore is open but there is zero net flow. Contour colors show Na^+ concentration in M.

12e cases in **Fig. 4.4**, where the counter-ions (Cl^-) were still concentrated in the middle of the pore similar to that in q = 6e case. It should be noted that both vdW interaction strength between chloride and carbon atoms ($\varepsilon_{Cl\text{-}C}$) and Cl-C intermolecular diameter ($\sigma_{Cl\text{-}C}$) are

greater than those of sodium and carbon atoms ($\varepsilon_{Na\text{-}C}$ and $\sigma_{Na\text{-}C}$) (See **Table 3.1**). Therefore, with the same Coulombic attraction strength (which is addressed in terms of the same magnitude of total charge fixed on the pore edge), sodium atoms are attracted closer to the carbon atoms due to the dominance of the Coulombic interactions over the vdW interactions and due to the shorter minimum distance ($\sigma_{Na\text{-}C}$) between the sodium and carbons atoms.

Figure 4.11 shows salt ion distributions in the *z*-direction at the end of the entire simulation time of pressure-driven flows through the negatively charged nanoporous graphene membranes. Similar to the positively charged cases, the counter-ions (Na^+) gather at the water-membrane interfaces and inside the pore region despite the pressure-driven flow. In all the four charged cases, Na^+ and Cl^- ions continue to flow with the water molecules. However, only in the case q = -6e, the passage of Na^+ and Cl^- ions through the membrane is small and the salt concentration in the feed reservoir increases with time, exhibiting higher values than its initial value shown in **Fig 4.9(b)**. This leaves a very small bulk concentration of salt ions in the permeate reservoir as shown in **Fig. 4.11(b)**. Different from positively charged cases, the Na^+ and Cl^- ions continue to pass through the membrane and result in large ionic concentrations in the permeate reservoir for the q = -9e and q = -12e cases. This can be attributed to the decreased crowding of Na^+ in the middle of the pore for $q \leq$ -9e, which leaves more space for the transport of salt ions in comparison with the behavior of q = -6e case. **Figure 4.12(a)** shows rejection efficiency for sodium and chloride ions as a function of the total negative charge obtained using viewpoint two, which shows an optimal value at q = -6e with 94% and 93% rejection efficiencies for Na^+ and Cl^- ions, respectively. **Figure 4.12(b)** provides the variation of pressure drop as a function of

the total applied charge. Similar to the positively charged cases, pressure drop increases nonlinearly with increased applied charge for the specified flow rate. This behavior is attributed the enhancement of bulk viscosity of water due to surface charges [99, 103-105].

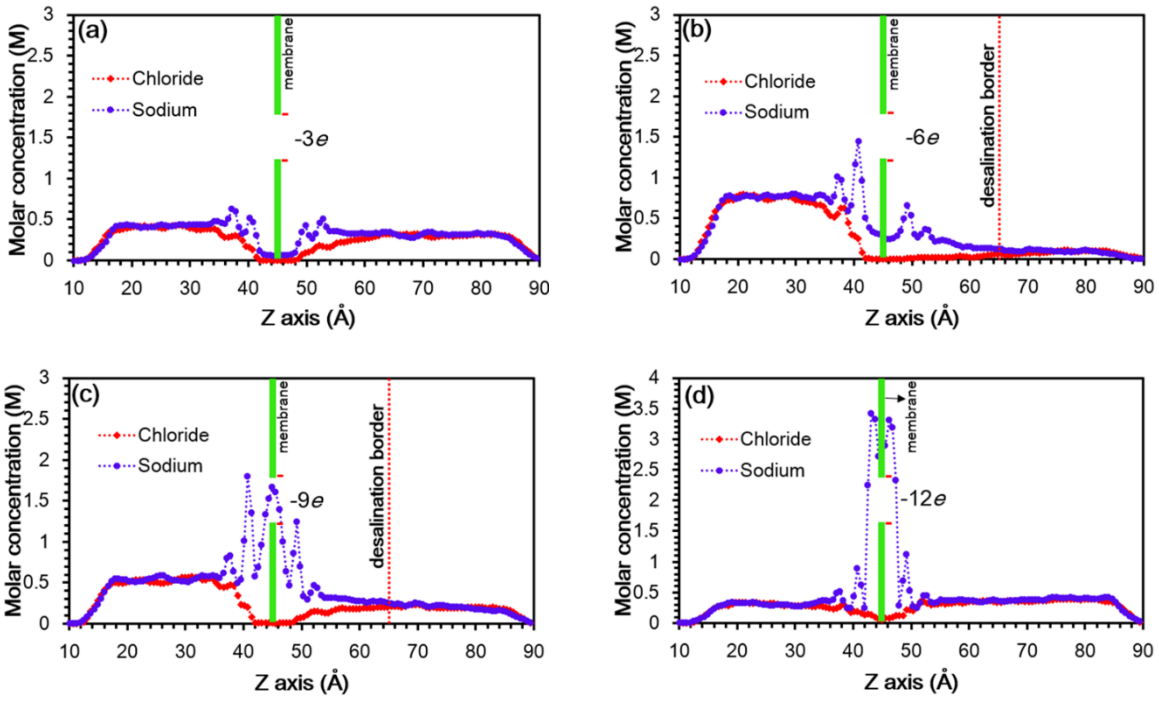

Figure 4.11. Distributions of sodium and chloride ion in the streamwise (*z*) direction for -3*e* (a), -6*e* (b), -9*e* (c), and -12*e* (d) total applied charge at the end of flow simulations (*t*=10 ns in stage *c*). The desalination border is shown in figures (b) and (c). Due to the use of slab-bins in z-direction, the presented ionic distributions are averaged across the entire membrane and pore areas.

Interestingly, with the reported salt rejection efficiencies for the q = -6e case, the corresponding pressure drop is approximately 13.8 MPa, which is 60.6% lower than that in the case of 9.9 Å pore diameter pristine graphene membranes that exhibits 100% salt rejection. Also, this value of pressure drop is approximately 20% lower than that in the case q = 9e. As compared to the q = 9e case, the result for the q = -6e case is better in terms

of required pressure drop but worse in terms of salt rejection. Negatively charged nanoporous graphene membranes with a hydraulic pore diameter of 14.4 Å and a total applied charge of -6*e* on the pore can be a good choice for RO desalination systems, where less power consumption is more critical than perfect salt rejection.

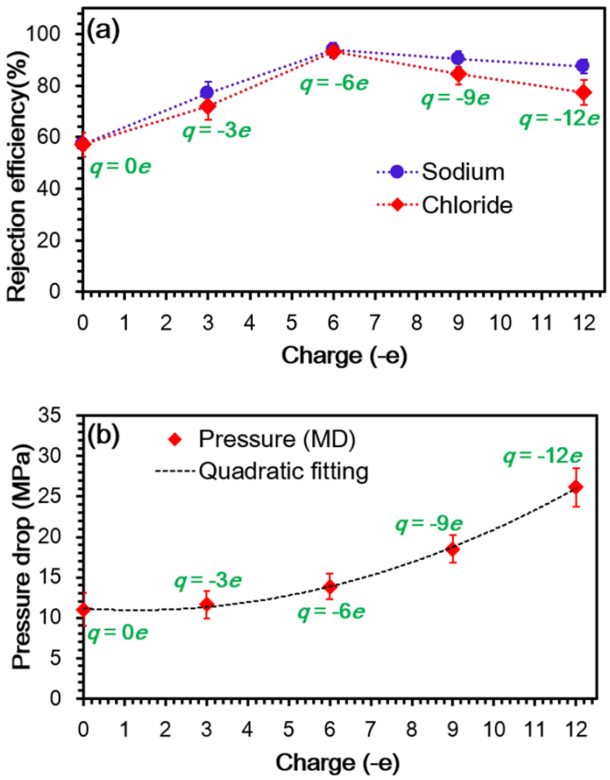

Figure 4.12. Rejection efficiency for sodium and chloride ions as a function of the total negative charge (a) obtained based on viewpoint two. Results were obtained at the end of flow simulations (*t*=10 ns in stage c). Variation of pressure drop as a function of the total surface charge (b). Data for *q*=0*e* are from Chapter 3. Standard deviation was calculated using data from ten different simulations with statistically different initial conditions.

In order to elucidate the differences in the transport of salt ions through charged membranes, I calculated the potential of mean force (PMF) experienced by the salt ions

before pressure-driven flows were established. PMF gives the average force potential that the membranes apply on the salt ions, representing the energy barier of the membranes for

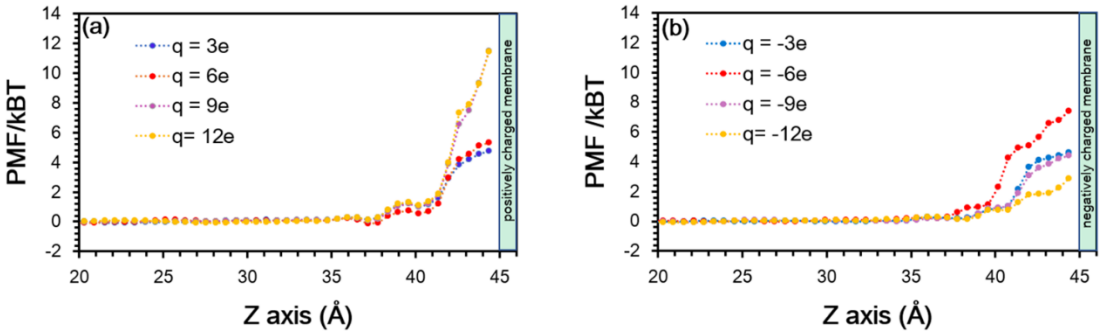

Figure 4.13. Potential of mean force (PMF) experienced by co-ions in the feed reservoir near the positively (a) and negatively (b) charged membranes with different total applied charges. Results were obtained in stage (b), where the nano-pore is open but there is zero net flow. Co-ions in figures (a) and (b) are Na^+ and Cl^-, respectively.

salt ions. In other words, a salt species with a higher PMF value has less probability to pass through the membranes. The PMF was extracted from the equilibrium density distribution of the salt ions in stage (b) using the following equation:

$$\mathrm{PMF}(z) = -k_B T \ln \frac{\rho(z)}{\rho_b} \tag{4.1}$$

where T is the temperature, k_B is the Boltzmann constant, and ρ_b is the salt density at the bulk region where PMF is zero. **Figure 4.13** shows the normalized PMF distributions of co-ions in the feed reservoir for positively and negatively charged cases. As shown in **Fig. 4.13(a)**, at the region near the positively charged membrane, the energy barrier for the co-ions (Na^+) increases with increased total applied charge and reaches to its highest value for the $q = 9e$ and $q = 12e$ cases. For the negatively charged membranes, the energy barrier for

the co-ions (Cl^-) is low in the q = -3e, -9e, and -12e cases and highest in the q = -6e case as shown in **Fig. 4.13(b)**. The PMF results are consistent with the previously discussed optimal salt rejection efficiencies.

4.2.3. Time-Dependence of Salt of Ion Concentration in Feed Reservoirs

Accumulation of salt ions in the feed reservoir creates time-dependent ion concentration. Because of the limitations in computational resources, all MD systems in the literature focusing on RO water desalination selected the sizes of feed reservoirs on the order of several nanometers. This leads to a large decrease in the volume of the feed reservoirs after a short simulation time, and the presented salt rejection efficiencies can be artificially reduced with longer simulation time. In practical RO desalination systems, the length of feed reservoirs should be much longer than those illustrated in MD simulations. Correspondingly, the accumulation of salt ions in feed reservoirs can slowly occur. In order to better link our study results with those in practical RO water desalination systems, I extracted the time-dependent salt concentration in the q = 9e case for the current simulation domain, called "single-feed domain", and for a simulation domain with the feed reservoir's length doubled, called "double-feed domain". **Figure 4.14(a)** presents the concentration of salt ions in different regions as a function of time for the single-feed domain, whereas **Figure 4.14(b)** shows those for the double-feed one. It is seen in both settings that Cl^- bulk concentration increases with time until the feed bulk region disappears. The Cl^- concentration in the feed interface region also increases with time while those in permeate interface and permeate bulk regions remain unchanged for a while. Feed interface region

is bounded by the membrane and the point where Na^+ and Cl^- concentrations starts to be equivalent in the feed reservoir (approximately 10 Å away from the membrane, see **Fig. 4.6(c)**). The permeate interface region is defined from the membrane to the desalination border in the permeate reservoir. Upon the leakage of Cl^- ions through the membrane due to the artificially close distance of the moving reflection boundary to the membrane, the Cl^- concentration in permeate interface starts to increase. However, the leakage of Cl^- ions through the defined desalination border is very small, presented by the small increase in the Cl^- concentration in the permeate bulk region. This confirms the stable absorption of Cl^- ions into the interfaces of the positively charged membranes as discussed previously. In the same manner, the Na^+ bulk concentration increases with time and then decreases sooner than Cl^- concentration. A minor increase in the Na^+ permeate bulk region presents small leakage of Na^+ through the desalination border. Importantly, the time at which salt ions start to leak for the double-feed domain is approximately twice as long as that for the single-feed one (68 ns and 34 ns for Cl^- ions, and 65 and 32 ns for Na^+ ions). The longer time for the initiation of salt leakage in the double-feed domain confirms the slow accumulation of salt ions in feed reservoirs with longer feed length. This ensures that the presented desalination efficiencies are persevered in practical RO desalination systems. I also noticed a linear regime of bulk salt accumulation in the feed reservoirs before an abrupt build-up occurs. In this stage, the percentage of increase of the bulk salt concentration in the feed reservoir is approximately equal to the percentage of decrease of the feed volume. Using MD data as conditions for establishing this linear functional relationship, I achieved an equation as follows:

$$C = C_0(1+2\lambda) \tag{4.2}$$

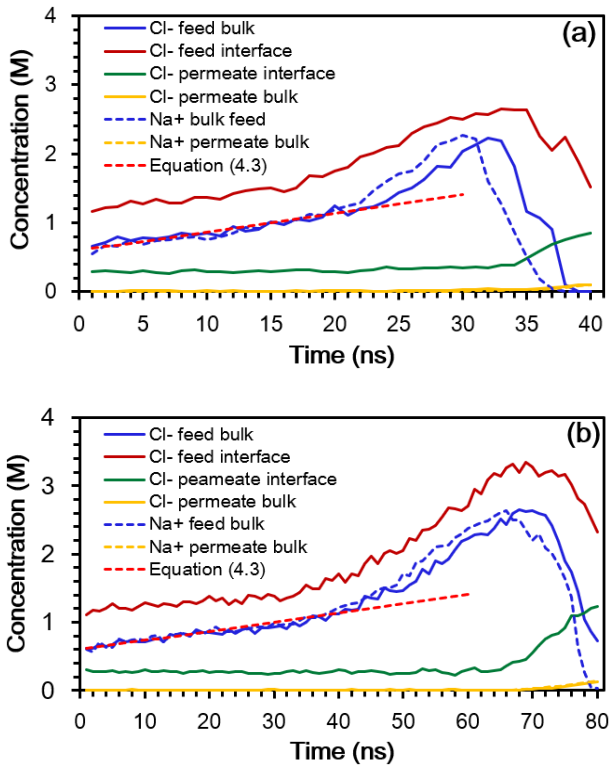

Figure 4.14. Na^+ and Cl^- ions concentration in different regions as function of time for (a) the single-feed simulation domain and for (b) the double-feed simulation domain.

where C is the bulk salt concentration in the feed reservoir at a given time, C_0 is the initial bulk concentration in the feed reservoir, λ is the time-rate of decrease of the feed reservoir volume given by $\lambda = (u \times t) / L_0$, where u is the velocity of the specular reflection boundary, t is the time, and L_0 is the original length of the feed reservoir in the stream-wise direction. Rewriting Eq. (4.2) one obtains an explicit time-dependent function of bulk salt concentration in the feed reservoir as follows:

$$C = C_0 \left(1 + 2 \frac{u \times t}{L_0} \right) \tag{4.3}$$

As shown in **Fig. 4.14**, predictions from Eq. (4.3) are in good agreement with the MD data as long as the bulk salt concentration in the feed reservoir is less than 1.2 M. This value can be considered as a general limit for saltwater processed in RO desalination systems using the proposed charged nanoporous graphene membrane. Equation (4.3) serves as an efficient prediction tool for time-dependent salt concentration in the feed reservoirs of those systems.

4.3.Conclusions

In this Chapter, a systematic investigation of salt water transport through positively and negatively charged nanoporous graphene membranes was conducted. Charges were equally distributed on the carbon atoms belonging to the pore edge with total charge of ±3e, ±6e, ±9e, and ±12e per pore, respectively. Pressure-driven flows through the membranes were established by moving specular reflection boundaries at a constant speed, resulting in a specified flow rate for all cases. By analyzing the salt ion distributions before and after starting flows, I identified a desalination border 20 Å downstream of the membrane in the permeate reservoir. Counter-ions concentrate, and co-ions are depleted in the region between the charged membrane and desalination border. Based on this observation, I found that the rejection efficiency for the $q = 9e$ case is approximately 100% and 98% for Na^+ and Cl^- ions, respectively. The required pressure drop in this case is 35% less than that in 9.9 Å pore diameter pristine graphene membrane case with 100% salt rejection efficiency at the same flow rate. I also found that for $q = -6e$, the rejection

efficiencies of the Na^+ and Cl^- ions are 94% and 93%, respectively, and the required pressure drop is 60.6% less than that in 9.9 Å pore diameter pristine graphene membrane case. It was also seen that applied electric charges increase the pressure drop through the membrane due to Coulomb interactions and ionic crowding near the pores. However, reported pressure drops for all 14.40 Å pore diameter charged cases are significantly lower than that with the 9.9 Å diameter pristine membrane at the same flow rate. Therefore, the q = 9e case is considered as the optimal charge setting for 14.40 Å pore diameter graphene membranes. In addition, PMF experienced by the salt ions before pressure-driven flow was established was analyzed to explain the differences in the transport of salt ions through the charged membranes. The PMF distributions of co-ions in the feed reservoir are consistent with the reported optimal salt rejection efficiencies. Finally, I developed a functional relationship between the accumulation of salt ions with the time-dependent volume change in the feed reservoir. The established equation is valid for the optimal case of $q = 9e$ as long as bulk salt concentration in the feed reservoir is less than 1.2 M. This value can be considered as a general limit for saltwater processed in RO desalination systems. Overall, reported results promise high potential of using charged nanoporous graphene membranes in RO desalination systems.

Chapter 5

GRAPHENE AND HEXAGONAL BORON NITRIDE COMPARISON, AND DETERMINATION OF OPTIMAL CHARGES FOR WATER DESALINATION

Pressure-driven water desalination using hexagonal boron nitride (h-BN) and charged nanoporous graphene membranes is investigated using molecular dynamics (MD) simulations. Nanoporous h-BN membranes with pore diameters of 10.1 Å, 12.2 Å, and 14.7 Å were selected to compare with similar pore diameters of uncharged nanoporous graphene membranes. Charged graphene membranes with large pore diameters of 15.9 Å, 18.9 Å, and 20.2 Å were also considered. I found that salt rejection efficiency with uncharged graphene is superior to that of h-BN, whereas pressure drop follows the same inverse-cubic dependence on pore diameter regardless of the membrane materials. I also found a 15.9 Å pore diameter with total fixed charge of 12*e* as the optimal setting for single-layer graphene membrane, in which the rejection efficiencies of Na^+ and Cl^- ions of 100% and 98% are achieved, respectively. The corresponding pressure drop is 51.8% lower than that obtained with 9.9 Å pore diameter uncharged graphene with 100% salt rejection. Starting from a pore diameter of 20.2 Å, positively charged nanoporous graphene membranes are not efficient in salt removal. Importantly, I found charged bilayer graphene membranes with a 15.9 Å pore diameter, 12*e* total charge on the first layer, and -1*e* on the second one as the alternative setting for perfect salt removal. The associated pressure drop is 35.7% lower than that obtained in 9.9 Å pore diameter uncharged base-line case. Our findings confirm the high potential application of charged bilayer nanoporous graphene membranes in improving performance of reverse osmosis (RO) desalination systems.

5.1. Simulation Settings and Methods

Desalination performance of nanoporous h-BN membranes with hydraulic dimeters of 10.1 Å, 12.2 Å, and 14.7 Å were investigated to compare with that of uncharged graphene membranes having hydraulic diameters of 9.9 Å, 11.57 Å, and 14.4 Å. The small mismatch between each corresponding pore size is because of the small difference in the lattice constants of h-BN and graphene as the same number of atoms were removed to create a pore on the membranes. As demonstrated in **Fig. 5.1(a)**, the simulation system was comprised of feed and permeate reservoirs. Specular reflection boundaries bound the ends of the simulation domain while a membrane (h-BN or graphene) was placed in the middle to separate the two reservoirs. **Figure 5.1(b) and (c)** show typical structures of nanoporous graphene and h-BN membranes with similar pore sizes. Hydraulic diameters were used due to the noncircular structure of the pores, which originated from the hexagonal lattice structure of both graphene and h-BN. In addition, nanoporous graphene membranes with hydraulic diameters of 15.9 Å, 18.9 Å, and 20.2 Å were then investigated by applying positive charges on the pore edge as shown in **Fig 5.1(d).** This approach seeks an optimal setting of charged single-layer nanoporous graphene membranes providing smaller required pressure drop and high salt rejection efficiency at the specified high flow rate. For each pore diameter, the carbon atoms around the pore edge have uniform charge distribution with a total net charge of 9*e*, 12*e*, 15*e*, and 18*e*, respectively. The chosen

starting case of $q = 9e$ is based on the optimal charge setting for pore radius of 14.4 Å as introduced in Chapter 4 [110].

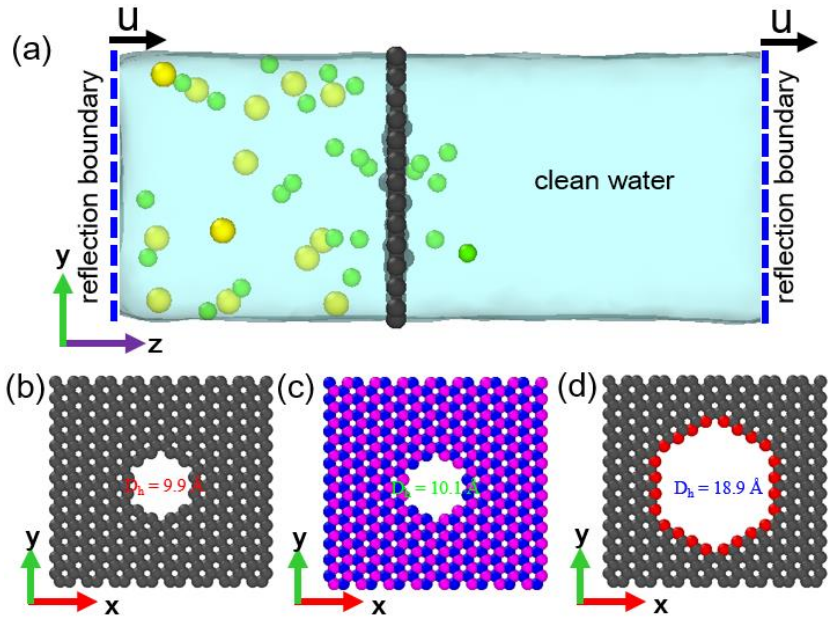

Figure 5.1. (a) Schematics of the single-layer simulation domain in side view. Sizes of sodium (yellow) and chloride (green) ions are exaggerated for better visualization. Pore shapes for (b) uncharged graphene (c) h-BN, and (d) charged graphene. Boron atoms are shown in pink and nitrogen atoms are shown in blue. Charged carbon atoms belonging to the graphene pore edge are shown in red.

Initially the system contained salt water and pure water molecules in the feed and permeate reservoirs, respectively. For the ultimate focus on seawater, the feed-reservoir bulk NaCl concentration was preserved at 0.6 M in all cases. Based on this, the feed reservoir with h-BN membranes was initially assigned 14 ions for each salt type. The feed reservoir with charged graphene membrane was allocated 13 Na^+ ions whereas the number of Cl^- ions were selected as 22, 25, 28 and 31 for the cases of 9e, 12e, 15e, and 18e, respectively, for

each pore diameter. The change in the number of Cl^- ions was aimed to preserve electrical neutrality in the simulation system.

Water molecules were simulated using the SPC/E model introduced in Chapter 3. The intermolecular interactions (van der Waals forces) of salt ions, oxygen atoms in water, boron and nitrogen atoms in h-BN membranes, and carbon atoms in graphene membranes were modelled by a truncated LJ 12-6 potential. Short-range LJ interactions were trimmed at 10.0 Å while long-range ones were compensated by a tail correction technique. Oxygen-oxygen interaction values were taken from the SPC/E model [81]. Oxygen-carbon interaction parameters were selected based on empirical contact angle measurements [83]. Those between oxygen atoms and boron and nitrogen atoms were from the calculation of Aluru *et al*. for the SPC/E water model [111]. Bonding between the carbon atoms on graphene sheets was reserved by the AIREBO potential [76]. Intramolecular interactions between boron and nitrogen atoms in h-BN sheets were modeled using the Tersoff potential [77]. Coulombic interactions were coupled with all atomic species having charge, and long-range electrostatic interactions were corrected using the PPPM method [85]. Sodium ions and chloride ions were allocated charges of $q_{Na} = 1.0e$ and $q_{Cl} = -1.0e$, respectively. Quantum calculated GROMACS force fields were used for LJ interactions of sodium and chloride ions in aqueous solutions to observe reasonable transport properties for ionized water [84]. All the utilized interaction terms are provided in **Table 5.1**. The LAMMPS software package was used to perform all the simulations with the VERLET algorithm integration for a time-step of 1.0 fs [61].

Simulation of saltwater transport through the nanoporous membranes was conducted with three consecutive MD simulation stages including equilibrium simulation with closed-pore

membranes, equilibrium simulation with opened-pore membranes, and non-equilibrium simulation with pressure-driven flow as well presented in Chapters 3 and 4 [100, 110]. Notably, in the non-equilibrium stage, flow through the nanopores was established by moving the two specular refection boundaries with a constant speed in the stream-wise (z) direction, while the membranes were fixed at the initial locations. A volumetric flow rate of 3.73×10^{-12} L/h-pore, which is the maximum volumetric flow rate of water obtained in the uncharged graphene base-line case, was preserved. The membranes were thermally vibrating at 300 K to include mechanical deformation and wetting characteristics. Data acquisition lasted in 10.0 ns of the non-equilibrium stage. Presented data for pressure and ion rejection efficiency were averaged from the results obtained from 10 different non-equilibrium simulations starting off at different equilibrium points.

5.3. Results and Discussion

Figures 5.2(a) and (b) illustrate the typical distributions of salt ions in z-direction of the simulation domain with nanoporous h-BN membranes at the opened-pore stage. Data were only taken from 10.1 Å and 12.2 Å pore diameter cases, respectively, for brevity due to the similarity between 12.2 Å and 14.4 Å cases. It is seen that ionic concentrations of Na^+ and Cl^- ions are approximately identical and there is no significant accumulation of salt ions near the membranes as similarly seen with graphene membranes [100]. This is attributed to the overall electrical neutrality of both graphene and h-BN membranes although each boron or nitrogen atom in h-BN has its own partial charge. This is different from what was observed with charged graphene membranes in which counter-ions excessively gather near

the membrane whereas co-ions are depleted, forming an electrical double layer [110]. It is also noted that in this stage no ions pass through the 10.1 Å pore diameter h-BN membranes while ion leakage happens for 12.2 Å and 14.4 Å cases. **Figure 5.2(c)** provides the comparison in the distributions of water near h-BN and graphene membranes. There is no difference in the water distributions except that density peak near h-BN membrane is higher than that near graphene membrane. This is consistent with the hydrophilic property of h-BN [111] and the hydrophobic property of graphene [101, 112]. Stronger solid-liquid interaction attracts more water molecules to solid-liquid interfaces [101, 102]. There is also no mismatch between the positions of the density peaks near the membranes due to the equivalence between the intermolecular diameters of carbon-oxygen, boron-oxygen, and nitrogen-oxygen. **Figure 5.2(d)** shows the required pressure drop for the different pore diameters of h-BN and graphene membranes. Pressure drop is proportional to inverse of the cube of pore diameter regardless of the membrane material. This reveals the negligible effects of slip at pore edges. It is worth mentioning that the inverse cubic prediction shown in the figure is consistent with that established for graphene $\left(\Delta P = \frac{\mu \Phi}{C_{\mathrm{o}}} \frac{1}{D_{\mathrm{h}}^3} \right)$ as shown in Chapter 3. The C_{o} value of 1/38.1 was obtained for both h-BN and graphene, and it is comparable to that previously obtained for graphene only. In addition, for any similar pore diameter, salt rejection efficiency with h-BN membrane is smaller than that with a graphene membrane. Particularly, no perfect rejection was seen with the 10.1 Å pore diameter h-BN membrane as compared to the 9.9 Å pore diameter uncharged graphene membrane.

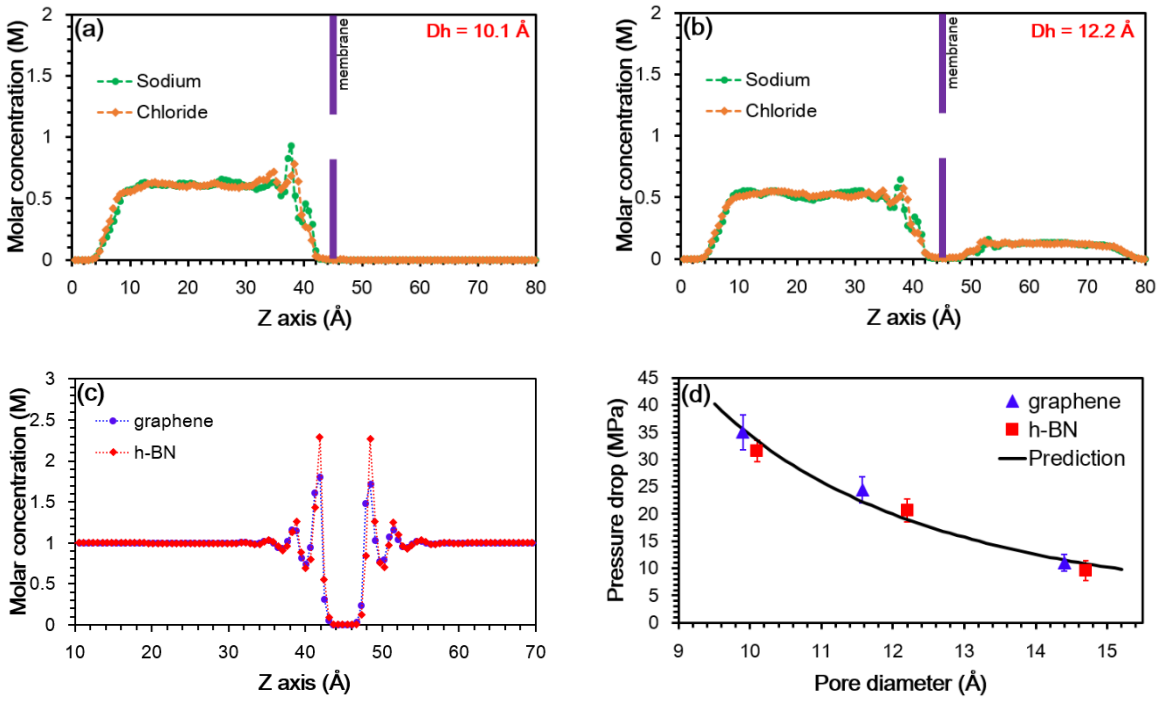

Figure 5.2. Distributions of Na^+ and Cl^- a long the z-direction of a h-BN membrane simulation domain for (a) D_h = 10.1 Å and (b) D_h = 12.2 Å. (c) The comparison of water distribution near h-BN and graphene membranes. (d) Pressure drop for the different pore dimeters of h-BN and graphene membranes. Data for uncharged graphene were taken from Chapter 3.

Distributions of salt ions in the *z*-direction after the entire simulation time of pressure-driven flows for several selected cases of pore diameter and charges of graphene membranes are shown in **Fig. 5.3**. It was seen that in all the selected cases and other different pore diameter and charge cases (not shown), a big portion of Cl^- ions gather at both sides of the membranes. For the 15.9 Å, $q = 9e$ case, some Cl^- and Na^+ ions go downstream after passing the membrane and form a noticeable bulk salt concentration. Feed-reservoir salt concentration increases with time due to the decreased volume of the feed reservoir and reduced transported salt ions. In the 15.9 Å, $q = 12e$ case, no Na^+ ions

leak through the membrane and only a couple of Cl^- ions go downstream. The permeate bulk region is therefore left with very small salt concentration. These phenomena were also observed in 18.9 Å, $q = 15e$ or higher charge case although a tiny portion of Na^+ ions pass through the membranes. Based on these observations, a "desalination border" is defined at 20 Å behind the charged membrane, which is the beginning of the bulk regions in the permeate reservoirs as shown in **Fig. 5.3(b)** and **Fig. 5.3(c)**. Between the membrane and desalination border, accumulation of counter-ions and depletion of co-ions coexist. For the pore diameter of 20.2 Å, prominent leakage of Na^+ ions through the membrane was observed in all charge cases as typically shown in **Fig. 5.3(d)** for $q = 18e$, forming a significant salt bulk regions downstream. The permeation of salt ions in the mentioned cases reduces feed-reservoir bulk salt concentration. This reveals that Coulombic interactions are not able to compensate for the small contribution from weak Na^+/pore intermolecular interactions in this large pore size even with the large charge setting ($q = 18e$).

Figure 5.4(a) shows the dependence of pressure drop on total fixed charge for different pore diameters. For all pore sizes, pressure drop is a nonlinear function of the charge magnitude at the specified flow rate. The charges fixed on the nanopores enhance bulk water viscosity due to the increase in hydrogen bonding between water molecules [99, 103-105], leading to higher required pressure drop. Moreover, the increased crowding of Cl^- ions in the pore region with the increased fixed charge requires higher pressure drop for water molecules to pass through the pores at the specified flow rate (Chapter 4) [110]. In addition, it was observed that for a specified charge, pressure drop is significantly lower for larger pore diameter. **Figures 5.4(b)** and **(c)** show Na^+ and Cl^- ions rejection efficiencies

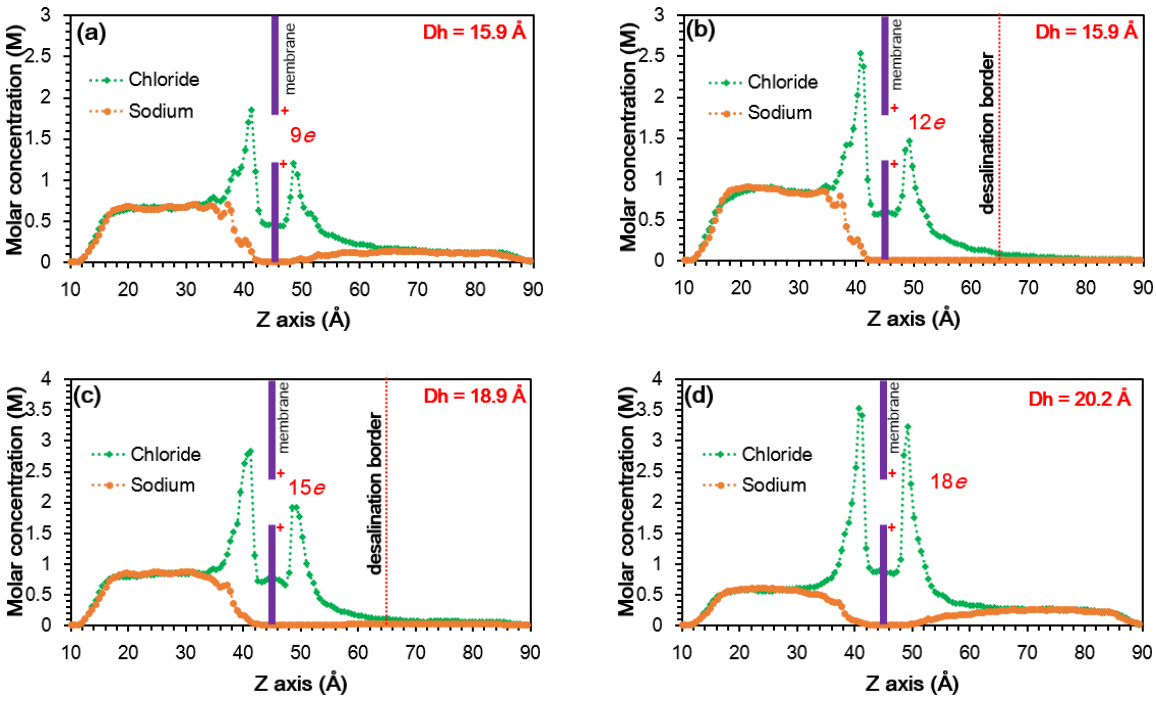

Figure 5.3. Distribution of salt ion along the z-direction of the charged nanoporous graphene membrane simulation system at 10 ns after the flow has been started for (a) 15.9 Å, q = 9e; (b) 15.9 Å, q = 12e; (c) 18.9 Å, q = 15e; (d) 20.2 Å, q = 18e.

for different pore diameters and charges. Salt rejection efficiency was calculated by considering the number of salt ions remaining past the desalination border at the end of simulations. For 15.9 Å and 18.9 Å pore diameter cases, both Na^+ and Cl^- ion rejection efficiencies increase with higher charge and then stabilize at a maximum value starting from q = 12e and q = 15e, respectively. The increase in Na^+ rejection is attributed to the larger hindrance caused by the greater amount of positive charges on the pores, whereas the increase in Cl^- rejection is ascribed to the increased gathering of Cl^- ions at solid-liquid interfaces. With increased surface charge, more Cl^- ions are trapped between the membrane and the desalination border and the crowding of Cl^- ions in the pore region is also increased.

However, for the 20.2 Å pore diameter case, Na^+ and Cl^- rejection efficiencies for different fixed charges are not much different from each other and all are lower than those of the smaller pore sizes. This is consistent with the salt distributions after flow was established for this pore size as discussed earlier. Notably, in the 15.9 Å and $q = 12e$ case, 100% salt ions are eliminated, whereas approximately 98% of Cl^- ions are filtered. The corresponding pressure drop is approximately 16.93 MPa, which is 51.8% lower than that in 9.9 Å pore diameter uncharged graphene case with compete salt rejection [100]. Although we obtained similar results for salt rejection efficiencies in 15.9 Å with $q = 15e$ and $q = 18e$, the required pressure drops were higher. Therefore, $q = 12e$ is considered as the *optimal charge setting* for the 15.9 Å pore diameter membrane. For the 18.9 Å pore diameter, salt rejection percentages are highest and similar for $q = 15e$ and $q = 18e$ cases (99% for Na^+ and 98% for Cl^-) but the necessary pressure drop is higher for the $q = 18e$ case. The corresponding pressure drops for $q = 15e$ and $q = 18e$ are 14.08 MPa and 18.73 MPa, respectively. Therefore, the $q = 15e$ is considered as the optimal charge setting for the 18.9 Å pore diameter membrane. Although the required pressure drop associated with the 18.9 Å and $q = 15e$ case is lower than that with the 15.9 Å and $q = 12e$ case, the salt rejection efficiency is lower. Consequently, the 15.9 Å pore diameter and $q = 12e$ is generally considered as the optimal design for charged single-layer nanoporous graphene membranes by considering both salt rejection capability and pressure drop. In addition, for this optimal case, we attempted to develop a functional relationship between pressure drop, flow rate, pore diameter, and viscosity of water using the similar dimensional analysis as done with the pristine nanoporous graphene membrane (Chapter 3). The obtained form for the

equation is exactly the same with Eq. (3.6) in Chapter 3. I obtained C_o values approximately in the range of 1/44.87 to 1/45.40.

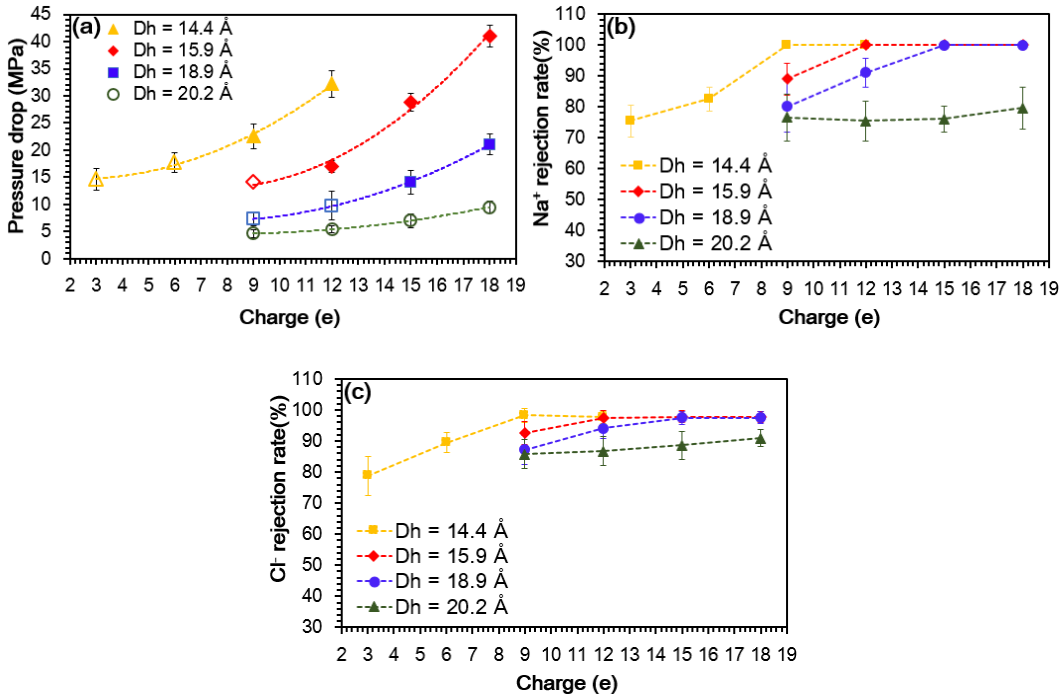

Figure 5.4. Dependence of pressure drop on the membrane charge for different pore diameters. Salt rejection efficiencies for (b) Na^+ and (c) Cl^- ions at the end of flow simulations for different pore diameters and charges. Data for D_h = 14.4 Å were taken from Chapter 4.

It was shown above that single-layer nanoporous graphene membranes with positive charges applied on the pores are efficient in RO desalination with pore sizes as large as 18.9 Å. Obtained results confirm the dominancy of electrostatic interactions between the fixed charges and mobile ions over the steric and hydrodynamic effects for pores as large as 18.9 Å. Although the obtained results for the charged single-layer nanoporous membranes are promising with reduced pressure drops as compared to the uncharged base-line case, salt rejection efficiencies are not 100%. In some scenarios, perfect salt rejection

efficiencies are mandatory, especially for drinkable water. For seawater with salt concentration of 0.6 M, even a rejection percentage of 99% leaves filtered water with 0.006 M (> 0.0017 M), which is not drinkable [57]. Based on the above analyses of the transport of ions through positively charged single-layer nanoporous graphene in optimal cases, only a small portion of Cl^- ions go downstream. **Table 5.2** summaries the salt rejection efficiencies and associated pressure drop for cases of optimal charge and pore size settings with single-layer nanoporous graphene membranes. Based on the above analyses of ion

Table 5.1 The interaction parameters utilized in the simulations.

Interaction	**ε (eV)**	**σ (Å)**
H-H	0	0
O-O	0.006736616	3.1656
O-Na	0.002079272	2.8704
O-Cl	0.005575083	3.8068
O-C	0.004062790	3.1900
Na-Na	0.000641772	2.5752
Na-Cl	0.001702700	3.5116
Na-C	0.001350014	2.9876
Cl-C	0.003619748	3.9240
Cl-Cl	0.004613823	4.4480
B-O	0.005264404	3.3100
B-Na	0.001617408	3.0141
B-Cl	0.004336703	3.9505
N-O	0.006504617	3.2660
N-Na	0.002001874	2.9558
N-Cl	0.005367560	3.9065

Table 5.2 Optimal cases of salt rejection efficiency and associated pressure drop for uncharged and charged single-layer nanoporous graphene membranes with different pore sizes at a specified maximum flow rate.

Pore diameter (Å)	**Charge (e)**	**Rejection efficiency (%)**		**Pressure drop (MPa)**
		Na^+	**Cl^-**	
9.9	0	100	100	35.02
14.4	9	100	98	22.70
15.9	12	100	98	16.93
18.9	15	99	98	14.08

transport through the charged single-layer membranes in optimal cases, only a small portion of Cl^- ions goes downstream. This leads to a motivation of placing a negatively low charged nanoporous graphene membrane behind the first one to prevent the passing of the Cl^- ions. The ultimate objectives are to obtain a perfect salt rejection efficiency, while pressure drop is still sustainably lower than that in the uncharged base-line case. This is the first approach in using charged bilayer graphene nanoporous for RO desalination while some studies for uncharged bilayer ones have been suggested in the literature [58, 59]. The proposed bilayer membrane desalination system is comprised of one feed reservoir and two permeate reservoirs as illustrated in **Fig. 5.5**. The first permeate reservoir is bounded by the two membranes. Pores on the two membranes are located at the same *x* and *y* coordinates and they have the same diameter. Hydraulic diameters of 14.4 Å, 15.9 Å, and 18.9 Å, were chosen. The total net charges of 9*e*, 12*e*, and 15*e* were assigned on the first membranes with uniform distribution on pore-edge carbon atoms. The chosen number of charges is based on the optimal charge setting for the corresponding pore sizes on single-

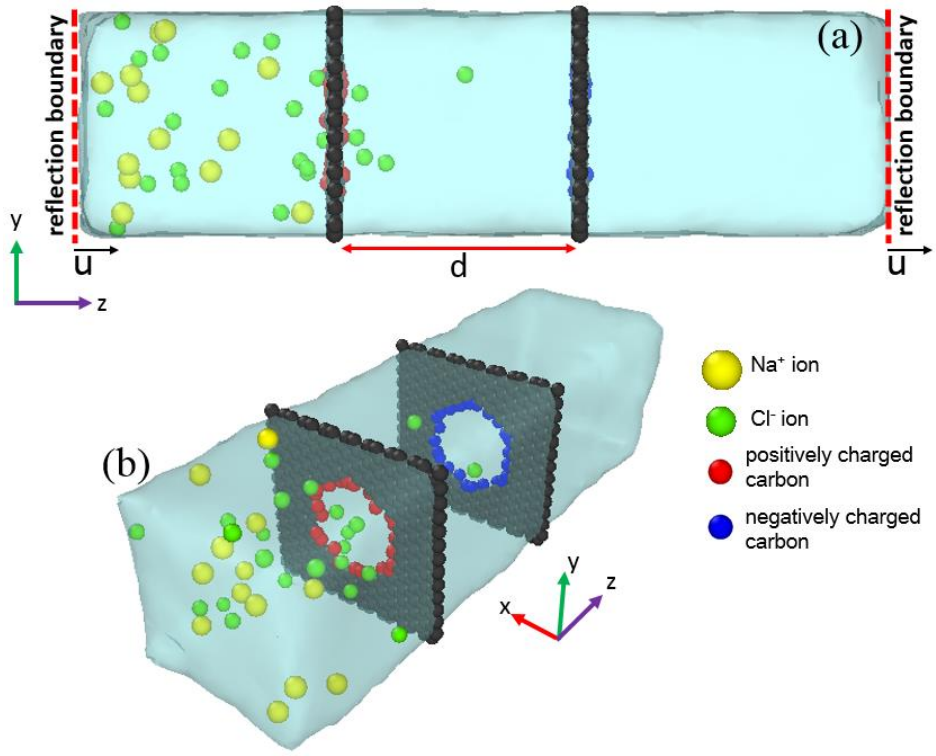

Figure 5.5. (a) Schematics of the bilayer simulation domain in two-dimensional (2D) view. (b) Schematics of the simulation domain in three-dimensional (3D) view. In (a) and (b), sizes of sodium (yellow) and chloride (green) ions are exaggerated for better visualization. Postively charged carbon atoms belonging to the pore edge of the first membrane are shown in red. Negatviely charged carbon atoms belonging to the pore edge of the second membrane are shown in blue.

layer membranes (**Table 5.2**). The total net charge of -1*e* was distributed on the pore edge carbon atoms of the second membranes. This is considered low charge setting with only -0.0417*e* per carbon atom even for the smallest pore size (14.4 Å). Initially 13 Na^+ - 21 Cl^- ions, 13 Na^+ - 24 Cl^- ions, 13 Na^+ - 27 Cl^- ions were assigned to the feed reservoirs of corresponding cases of (14.4 Å, 9*e*, -1*e*), (15.9 Å, 12*e*, -1*e*), and (18.9 Å, 15*e*, -1*e*), respectively. Methods of establishing flows and data acquisition were the same with those for the investigated single-layer membranes (Chapters 3 & 4).

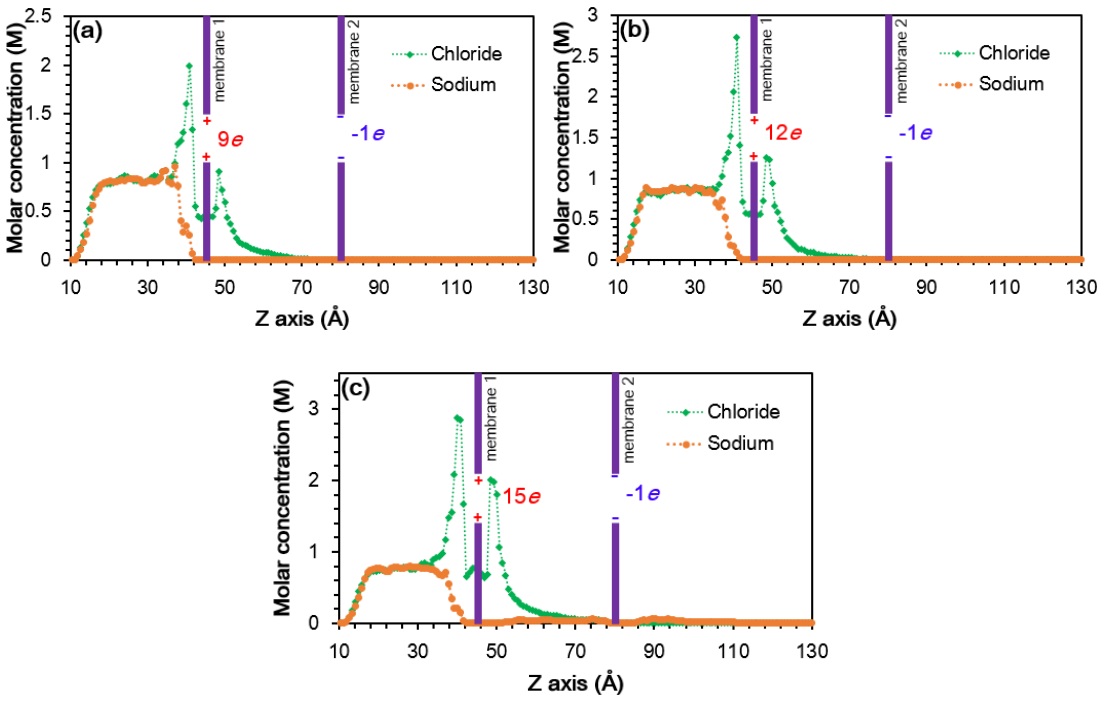

Figure 5.6. Distributions of sodium and chloride ions in the feed and permeate reservoirs along the z-direction of the simulation domain when pores are opened and pressure-drvien flows are ebtablished with the moving specular reflection boundaries (at t = 10 ns). (a) D_h = 14.4 Å, q_1 = 9*e*, q_2 = -1*e*; (a) D_h = 15.9 Å, q_1 = 12*e*, q_2 = -1*e*; (a) D_h = 18.9 Å, q_1 = 15*e*, q_2 = -1*e*.

Figure 5.6 provides the distributions of salt ions along the simulation domain after the entire simulation time of the non-equilibrium opened-pore stage. It is observed that the accumulation of Cl^- ions on both sides and inside the pore of the first membrane is stable. Due to the volume decrease of the feed reservoir, bulk salt concentration increases. For the (14.4 Å, 9*e*, -1*e*) and (15.9 Å, 12*e*, -1*e*) cases, still no Na^+ ion pass through the first membrane, leaving the first and second permeate reservoirs with zero Na^+ concentration. In these cases, no Cl^- ions pass the second membrane. For the (18.9 Å, 15*e*, -1*e*) case, there are a few salt ions passing the second membrane, leaving the second reservoir with nonzero

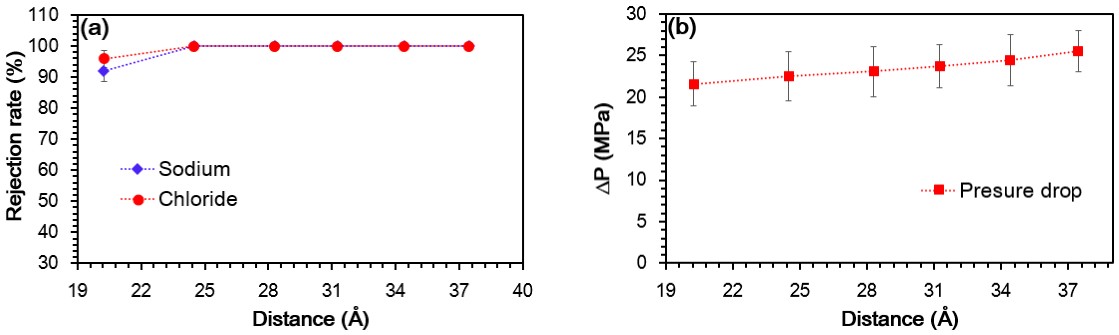

Figure 5.7. (a) Salt rejection efficiencies (a) and pressure drop (b) with different distances between the two membranes in the (D_h = 15.9 Å, q_1 = 12*e*, q_2 = -1*e*) case.

salt concentration. According to these observations, salt efficiencies for the considered case are based on the number of ions remaining past the second membrane. Results show 100% salt rejection efficiencies for the (14.4 Å, 9*e*, -1*e*) and (15.9 Å, 12*e*, -1*e*) cases. For the (18.9 Å, 12*e*, -1*e*) case, 91% of Na^+ ions and 98% of Cl^- ions are filtered. I also took into account the associated pressure drop with each membrane setting case. The pressure drop is the difference of the feed-reservoir bulk pressure and the second-permeate-reservoir bulk pressure. The pressure drops associated with the cases of 14.4 Å, 15.9 Å, and 18.9 Å are approximately 30.73 MPa, 25.56 MPa, and 16.73 MPa, respectively. It is seen that although the (18.9 Å, 12*e*, -1*e*) case requires the smallest pressure drop, its salt rejection is not perfect. For the other two cases, (15.9 Å, 12*e*, -1*e*) is better with a smaller pressure drop and perfect salt rejection. This required pressure drop is approximately 27% lower than the 35.02 MPa needed in the 9.9 Å pore diameter uncharged membrane base-line case. Therefore, (15.9 Å, 12*e*, -1*e*) is considered as the best within the three selected cases of membrane and charge settings.

I investigated effects of pore size and charge setting of charged bilayer graphene membranes on RO desalination performance. For all the previously presented data, the distance between the graphene membranes (d) was fixed at 37.45 Å. To further understand the effects of the membrane distance on the desalination performance, I systematically reduced the membrane distance in the (15.9 Å, 12e, -1e) case with d = 34.4 Å, 31.25 Å, 28.3 Å, 24.5 Å, and 20.24 Å. Smaller d values were not considered because the thermodynamic state of water inside the first permeate reservoir was not well defined due to solid force-field effects of graphene membranes. It is shown in **Fig. 5.7(a)** that perfect salt rejection is well reserved with d equal or greater than 24.5 Å. It is also revealed in **Fig. 5.7(b)** that the required pressure drop decreases with the decreased distance between the two membranes, which is an expected hydrodynamic effect as the flow exiting the first membrane could not expand and recirculate before it enters the second membrane. In combining the effects of the distance on salt rejection and pressure drop, d = 24.5 Å is considered as the optimal setting with ΔP = 22.51 MPa, which is 35.7% less than that of the uncharged membrane base-line case (35.02 MPa).

5.3. Conclusions

In this study, the comparison of the desalination performance of nanoporous h-BN and graphene membranes as well as the optimal design for charged nanoporous graphene membranes were provided using molecular dynamics simulations. Key conclusions are summarized as follows:

1. Salt rejection efficiency of nanoporous h-BN membranes are lower than that of nanoporous uncharged graphene membranes with similar pore size at the specified flow rate. The dependence of pressure drop on pore diameter follows the same inverse-cubic function regardless of the difference in the two membrane materials.

2. For charged graphene membranes with pore diameters as large as 18.9 Å, Na^+ and Cl^- ion rejection efficiencies increase with increasing the total charge on the pore edges and then stabilize at a maximum. However, for a pore diameter of 20.2 Å, Na^+ and Cl^- rejection is low even with higher charge setting.

3. For the different pore sizes of nanoporous graphene membranes, pressure drop is a nonlinear function of charge on the pore at the specified flow rate. For the same total fixed charge, pressure drop is significantly smaller for larger pore sizes.

4. A single-layer graphene membrane with 15.9 Å pore diameter and 12*e* total charge on a pore is the optimal setting in which the rejection efficiencies of Na^+ ions and Cl^- ions with 100% and 98% are achieved, respectively. The corresponding required pressure drop is approximately 16.93 MPa, which is 51.8% the uncharged graphene base-line case.

5. Charged bilayer nanoporous graphene membranes with D_h = 15.9 Å, q_1 = 12*e*, q_2 = -1*e*, and membrane distance of ~ 2.5 nm is the optimal setting for obtaining 100% salt rejection efficiency and 35.7% lower pressure drop as compared to the uncharged single-layer graphene base-line case with the same rejection efficiency.

Overall, the reported results disclose the high potential applications of charged nanoporous graphene membranes for enhancing the performance of RO desalination systems.

Chapter 6

SUMMARY AND FUTURE RESEARCH

This chapter summarizes the work presented in this dissertation and discusses possible future works related to the current study.

6.1 Summary of the Current Study

In Chapter 1, I first introduced the motivation and the potential applications of using graphene-based membranes for RO water desalination based on a literature review. The fundamental aspects in RO water desalination performance including sustainability of membranes, salt rejection efficiency, pressure drop, and flow rate were discussed. The broad picture of the whole research was also provided in this chapter to make it easier to follow the subsequent developments. Chapter 2 provided fundamentals of the molecular dynamics simulation method which was used in all simulations in this dissertation. In Chapter 3, first the method of creating pressure-driven flows through nanoporous graphene membranes in molecular dynamics simulations based on the motion of specular reflection boundaries was proposed and validated. After that, desalination performance of pristine nanoporous graphene membranes with hydraulic pore diameters of 9.9 Å, 11.57 Å and 14.40 Å was examined. It was shown that perfect rejection can be obtained with a pore diameter of 9.9 Å whereas larger pore diameters render lower salt rejection rates at the specified maximum flow rate. A functional relationship between the pressure drop, flow rate, dynamic viscosity, and pore diameter for water flows through nanoporous graphene membranes was also developed. In Chapter 4, the potential application of charged

nanoporous graphene membranes were studied for graphene membranes with a pore diameter of 14.4 Å. This pore size is associated with the lowest salt rejection efficiency and required less pressure drop compared with uncharged graphene membranes. It was shown that the positively charged membranes are better than the negatively charged membranes in rejecting salt ions. Specifically, I found $q = 9e$ as the optimal setting for positively charged membranes in which approximately 100% and 98% rejection of Na^+ and Cl^- ions were obtained, respectively. The required pressure drop in this case is 35% less than that in the 9.9 Å pore diameter pristine graphene membrane case with 100% salt rejection efficiency at the same flow rate. Also, $q = -6e$ was determined as the optimal setting for negatively charged membranes with rejection efficiencies of 94% and 93% for Na^+ and Cl^- ions, respectively. Required pressure drop is 60.6% less than that in the 9.9 Å pore diameter base-line case. In Chapter 5, I first tried to compare desalination performance of h-BN and pristine graphene membranes due to the emergence of h-BN as a potential 2D material for RO water desalination. In addition, based on the promising results obtained for positively charged 14.4 Å pore diameter graphene membranes, larger pore sizes were investigated. It was observed that positively charged graphene membranes still provide high salt removal with reduced pressure drop for pore diameters as large as 18.9 Å. Based on the critical requirement of salt rejection efficiency of approximately 100% for drinkable water, a design of charged bilayer nanoporous graphene membranes was proposed based on the optimal cases of single-layer graphene membranes. It was shown that $D_h = 15.9$ Å, $q_1 = 12e$, $q_2 = -1e$, and a membrane distance of ~ 2.5 nm is the optimal setting for obtaining 100% salt rejection efficiency and 35.7% lower pressure drop as compared to the uncharged single-layer graphene base-line case with the same rejection effectiveness.

6.2 Future Research

In future work, comparison of desalination performance between different atomically thin materials such as graphyne, graphane, MoS_2, borophene, MXenes and graphene membranes can be performed. A broad understanding in water desalination performance of the mentioned membranes can provide flexible applications in pressure-driven flows water desalination. The selection of each type of the membranes depends on the feasibility in membrane fabrication, mechanical and chemical stability of the membranes, and water desalination performance for different purposes. Beyond the applications in water desalination, the biological applications of graphene-based and h-BN membranes can be investigated, such as DNA and protein sequencing using electrically driven flows based on our knowledge of simulating transport of fluids through the 2D membranes. Determining nucleotides in DNA and amino acids in proteins can help diagnose early serious diseases like cancer and provide faster and essential treatment. Thus, these researches will be significantly beneficial to disease treatment or other medical applications.

References

1. Postel, S., *The last oasis: facing water scarcity*. 2014: Routledge.
2. National Academy of Engineering. http://www.engineeringchallenges.org/challenges.aspx.
3. Gleick, P., *The world's water*. Issues in Science and Technology, 1998. **14**(4): p. 80-88.
4. Hsu, S., K. Cheng, and J.-S. Chiou, *Seawater desalination by direct contact membrane distillation.* Desalination, 2002. **143**(3): p. 279-287.
5. Sadrzadeh, M. and T. Mohammadi, *Sea water desalination using electrodialysis.* Desalination, 2008. **221**(1-3): p. 440-447.
6. Greenlee, L.F., et al., *Reverse osmosis desalination: water sources, technology, and today's challenges.* Water Research, 2009. **43**(9): p. 2317-2348.
7. Loeb, S., *Sea water demineralization by means of an osmotic membrane.* Adv Chem Ser, 1962. **38**: p. 117-132.
8. Cadotte, J.E., *Evolution of composite reverse osmosis membranes.* Materials Science of Synthetic Membranes, 1985: p. 273-294.
9. Kurihara, M., et al., *Spiral-wound new thin film composite membrane for a single-stage seawater desalination by reverse osmosis.* Desalination, 1980. **32**: p. 13-23.
10. Brousse, C., R. Chapurlat, and J. Quentin, *New membranes for reverse osmosis I. Characteristics of the base polymer: sulphonated polysulphones.* Desalination, 1976. **18**(2): p. 137-153.
11. Duke, M.C., et al., *Structural effects on SAPO-34 and ZIF-8 materials exposed to seawater solutions, and their potential as desalination membranes.* Desalination, 2016. **377**: p. 128-137.
12. Zhu, B., et al., *Application of robust MFI-type zeolite membrane for desalination of saline wastewater.* Journal of Membrane Science, 2015. **475**: p. 167-174.
13. Zhao, K. and H. Wu, *Fast water thermo-pumping flow across nanotube membranes for desalination.* Nano Letters, 2015. **15**(6): p. 3664-3668.
14. Corry, B., *Designing carbon nanotube membranes for efficient water desalination.* The Journal of Physical Chemistry B, 2008. **112**(5): p. 1427-1434.
15. Lee, C., et al., *Measurement of the elastic properties and intrinsic strength of monolayer graphene.* Science, 2008. **321**(5887): p. 385-388.
16. Agrawal, K.V., et al., *Fabrication, pressure testing, and nanopore formation of single-layer graphene membranes.* The Journal of Physical Chemistry C, 2017. **121**(26): p. 14312-14321.
17. Bae, S., et al., *Roll-to-roll production of 30-inch graphene films for transparent electrodes.* Nature Nanotechnology, 2010. **5**(8): p. 574.
18. Priyadarsini, S., et al., *Graphene and graphene oxide as nanomaterials for medicine and biology application.* Journal of Nanostructure in Chemistry, 2018. **8**(2): p. 123-137.
19. He, H., et al., *A new structural model for graphite oxide.* Chemical Physics Letters, 1998. **287**(1-2): p. 53-56.

20. Perreault, F., A.F. De Faria, and M. Elimelech, *Environmental applications of graphene-based nanomaterials.* Chemical Society Reviews, 2015. **44**(16): p. 5861-5896.
21. Chang, J., et al., *Graphene-based sensors for detection of heavy metals in water: a review.* Analytical and Bioanalytical Chemistry, 2014. **406**(16): p. 3957-3975.
22. Surwade, S.P., et al., *Water desalination using nanoporous single-layer graphene.* Nature Nanotechnology, 2015. **10**(5): p. 459.
23. Russo, C.J. and J.A. Golovchenko, *Atom-by-atom nucleation and growth of graphene nanopores.* Proceedings of the National Academy of Sciences, 2012. **109**(16): p. 5953-5957.
24. O'Hern, S.C., et al., *Selective ionic transport through tunable subnanometer pores in single-layer graphene membranes.* Nano Letters, 2014. **14**(3): p. 1234-1241.
25. Garaj, S., et al., *Molecule-hugging graphene nanopores.* Proceedings of the National Academy of Sciences, 2013. **110**(30): p. 12192-12196.
26. Xu, Q., et al., *Controllable atomic scale patterning of freestanding monolayer graphene at elevated temperature.* ACS Nano, 2013. **7**(2): p. 1566-1572.
27. Kuan, A.T., et al., *Electrical pulse fabrication of graphene nanopores in electrolyte solution.* Applied Physics Letters, 2015. **106**(20): p. 203109.
28. Cohen-Tanugi, D. and J.C. Grossman, *Mechanical strength of nanoporous graphene as a desalination membrane.* Nano Letters, 2014. **14**(11): p. 6171-6178.
29. Nair, R., et al., *Unimpeded permeation of water through helium-leak–tight graphene-based membranes.* Science, 2012. **335**(6067): p. 442-444.
30. Joshi, R., et al., *Precise and ultrafast molecular sieving through graphene oxide membranes.* Science, 2014. **343**(6172): p. 752-754.
31. Han, Y., Z. Xu, and C. Gao, *Ultrathin graphene nanofiltration membrane for water purification.* Advanced Functional Materials, 2013. **23**(29): p. 3693-3700.
32. Cohen-Tanugi, D. and J.C. Grossman, *Water desalination across nanoporous graphene.* Nano Letters, 2012. **12**(7): p. 3602-3608.
33. Konatham, D., et al., *Simulation insights for graphene-based water desalination membranes.* Langmuir, 2013. **29**(38): p. 11884-11897.
34. Wang, Y., et al., *Molecular dynamics study on water desalination through functionalized nanoporous graphene.* Carbon, 2017. **116**: p. 120-127.
35. Chen, Q. and X. Yang, *Pyridinic nitrogen doped nanoporous graphene as desalination membrane: molecular simulation study.* Journal of Membrane Science, 2015. **496**: p. 108-117.
36. Heiranian, M., A.B. Farimani, and N.R. Aluru, *Water desalination with a single-layer MoS 2 nanopore.* Nature Communications, 2015. **6**: p. 8616.
37. Waki, H. and Y. Tokunaga, *Donnan exclusion chromatography: I. Theory and application to the separation of phosphorus oxoanions or metal cations.* Journal of Chromatography A, 1980. **201**: p. 259-264.
38. Zhao, S., J. Xue, and W. Kang, *Ion selection of charge-modified large nanopores in a graphene sheet.* The Journal of Chemical Physics, 2013. **139**(11): p. 114702.
39. Rollings, R.C., A.T. Kuan, and J.A. Golovchenko, *Ion selectivity of graphene nanopores.* Nature Communications, 2016. **7**: p. 11408.

40. Sint, K., B. Wang, and P. Král, *Selective ion passage through functionalized graphene nanopores.* Journal of the American Chemical Society, 2008. **130**(49): p. 16448-16449.
41. Lee, Y.K., et al., *Charge transport-driven selective oxidation of graphene.* Nanoscale, 2016. **8**(22): p. 11494-11502.
42. Gracheva, M.E., J. Vidal, and J.-P. Leburton, *p− n semiconductor membrane for electrically tunable ion current rectification and filtering.* Nano Letters, 2007. **7**(6): p. 1717-1722.
43. Shankla, M. and A. Aksimentiev, *Conformational transitions and stop-and-go nanopore transport of single-stranded DNA on charged graphene.* Nature Communications, 2014. **5**: p. 5171.
44. Loh, K.P., et al., *The chemistry of graphene.* Journal of Materials Chemistry, 2010. **20**(12): p. 2277-2289.
45. Ataca, C. and S. Ciraci, *Perpendicular growth of carbon chains on graphene from first-principles.* Physical Review B, 2011. **83**(23): p. 235417.
46. Fornasiero, F., et al., *Ion exclusion by sub-2-nm carbon nanotube pores.* Proceedings of the National Academy of Sciences, 2008. **105**(45): p. 17250-17255.
47. Stewart, R. and K. Yates, *The Position of Protonation of the Carboxyl Group1.* Journal of the American Chemical Society, 1960. **82**(15): p. 4059-4061.
48. Lin, Y., T.V. Williams, and J.W. Connell, *Soluble, exfoliated hexagonal boron nitride nanosheets.* The Journal of Physical Chemistry Letters, 2009. **1**(1): p. 277-283.
49. Corso, M., et al., *Boron nitride nanomesh.* Science, 2004. **303**(5655): p. 217-220.
50. Golberg, D., et al., *Boron nitride nanotubes and nanosheets.* ACS nano, 2010. **4**(6): p. 2979-2993.
51. Coleman, J.N., et al., *Two-dimensional nanosheets produced by liquid exfoliation of layered materials.* Science, 2011. **331**(6017): p. 568-571.
52. Wang, X., et al., *"Chemical Blowing" of Thin-Walled Bubbles: High-Throughput Fabrication of Large-Area, Few-Layered BN and Cx-BN Nanosheets.* Advanced Materials, 2011. **23**(35): p. 4072-4076.
53. Pakdel, A., et al., *Low-dimensional boron nitride nanomaterials.* Materials Today, 2012. **15**(6): p. 256-265.
54. Lee, C., et al., *Frictional characteristics of atomically thin sheets.* Science, 2010. **328**(5974): p. 76-80.
55. Jin, C., et al., *Fabrication of a freestanding boron nitride single layer and its defect assignments.* Physical Review Letters, 2009. **102**(19): p. 195505.
56. Gao, H., et al., *Rational design and strain engineering of nanoporous boron nitride nanosheet membranes for water desalination.* The Journal of Physical Chemistry C, 2017. **121**(40): p. 22105-22113.
57. USGS. https://www.usgs.gov/special-topic/water-science-school/science/saline-water-and-salinity?qt-science_center_objects=0#qt-science_center_objects.
58. Cohen-Tanugi, D., L.-C. Lin, and J.C. Grossman, *Multilayer nanoporous graphene membranes for water desalination.* Nano Letters, 2016. **16**(2): p. 1027-1033.
59. Muscatello, J., et al., *Optimizing water transport through graphene-based membranes: insights from nonequilibrium molecular dynamics.* ACS Applied Materials & Interfaces, 2016. **8**(19): p. 12330-12336.

60. Alder, B.J. and T.E. Wainwright, *Phase transition for a hard sphere system.* The Journal of Chemical Physics, 1957. **27**(5): p. 1208-1209.
61. Plimpton, S., *Fast parallel algorithms for short-range molecular dynamics.* Journal of Computational Physics, 1995. **117**(1): p. 1-19.
62. Phillips, J.C., et al., *Scalable molecular dynamics with NAMD.* Journal of Computational Chemistry, 2005. **26**(16): p. 1781-1802.
63. Van Der Spoel, D., et al., *GROMACS: fast, flexible, and free.* Journal of Computational Chemistry, 2005. **26**(16): p. 1701-1718.
64. Brooks, B.R., et al., *CHARMM: the biomolecular simulation program.* Journal of Computational Chemistry, 2009. **30**(10): p. 1545-1614.
65. Rapaport, D.C. and D.C.R. Rapaport, *The art of molecular dynamics simulation*. 2004: Cambridge University Press.
66. Karniadakis, G., A. Beskok, and N. Aluru, *Microflows and nanoflows: fundamentals and simulation*. Vol. 29. 2006: Springer Science & Business Media.
67. Tuckerman, M., *Statistical mechanics: theory and molecular simulation*. 2010: Oxford University Press.
68. Darden, T., D. York, and L. Pedersen, *Particle mesh Ewald: An N· log (N) method for Ewald sums in large systems.* The Journal of Chemical Physics, 1993. **98**(12): p. 10089-10092.
69. Hockney, R.W. and J.W. Eastwood, *Computer simulation using particles*. 1988: CRC Press.
70. Pollock, E. and J. Glosli, *Comments on P3M, FMM, and the Ewald method for large periodic Coulombic systems.* Computer Physics Communications, 1996. **95**(2-3): p. 93-110.
71. Zielkiewicz, J., *Structural properties of water: Comparison of the SPC, SPCE, TIP4P, and TIP5P models of water.* The Journal of Chemical Physics, 2005. **123**(10): p. 104501.
72. Vanommeslaeghe, K., et al., *CHARMM general force field: A force field for drug-like molecules compatible with the CHARMM all-atom additive biological force fields.* Journal of Computational Chemistry, 2010. **31**(4): p. 671-690.
73. Case, D.A., et al., *AMBER 9.* University of California, San Francisco, 2006. **45**.
74. Scott, W.R., et al., *The GROMOS biomolecular simulation program package.* The Journal of Physical Chemistry A, 1999. **103**(19): p. 3596-3607.
75. Doyama, M. and Y. Kogure, *Embedded atom potentials in fcc and bcc metals.* Computational Materials Science, 1999. **14**(1-4): p. 80-83.
76. Stuart, S.J., A.B. Tutein, and J.A. Harrison, *A reactive potential for hydrocarbons with intermolecular interactions.* The Journal of Chemical Physics, 2000. **112**(14): p. 6472-6486.
77. Tersoff, J., *New empirical approach for the structure and energy of covalent systems.* Physical Review B, 1988. **37**(12): p. 6991.
78. Kim, B.H., A. Beskok, and T. Cagin, *Viscous heating in nanoscale shear driven liquid flows.* Microfluidics and Nanofluidics, 2010. **9**(1): p. 31-40.
79. Irving, J. and J.G. Kirkwood, *The statistical mechanical theory of transport processes. IV. The equations of hydrodynamics.* The Journal of Chemical Physics, 1950. **18**(6): p. 817-829.

80. Yuan, Z., et al., *Mechanism and prediction of gas permeation through sub-nanometer graphene pores: comparison of theory and simulation.* ACS Nano, 2017. **11**(8): p. 7974-7987.
81. Berendsen, H., J. Grigera, and T. Straatsma, *The missing term in effective pair potentials.* Journal of Physical Chemistry, 1987. **91**(24): p. 6269-6271.
82. Ryckaert, J.-P., G. Ciccotti, and H.J. Berendsen, *Numerical integration of the cartesian equations of motion of a system with constraints: molecular dynamics of n-alkanes.* Journal of Computational Physics, 1977. **23**(3): p. 327-341.
83. Werder, T., et al., *On the water− carbon interaction for use in molecular dynamics simulations of graphite and carbon nanotubes.* The Journal of Physical Chemistry B, 2003. **107**(6): p. 1345-1352.
84. Patra, M. and M. Karttunen, *Systematic comparison of force fields for microscopic simulations of NaCl in aqueous solutions: diffusion, free energy of hydration, and structural properties.* Journal of Computational Chemistry, 2004. **25**(5): p. 678-689.
85. Allen, M.P. and D.J. Tildesley, *Computer Simulation of Liquids*. 2017: Oxford University Press.
86. Celebi, A.T., et al., *The role of water models on the prediction of slip length of water in graphene nanochannels.* The Journal of Chemical Physics, 2019. **151**(17): p. 174705.
87. Ang, E.Y., et al., *Free-standing graphene slit membrane for enhanced desalination.* Carbon, 2016. **110**: p. 350-355.
88. Yu, C.-J., et al., *Molecular layering in a liquid on a solid substrate: an X-ray reflectivity study.* Physica B: Condensed Matter, 2000. **283**(1-3): p. 27-31.
89. Lee, C.Y., J.A. McCammon, and P. Rossky, *The structure of liquid water at an extended hydrophobic surface.* The Journal of Chemical Physics, 1984. **80**(9): p. 4448-4455.
90. Cheng, L., et al., *Molecular-scale density oscillations in water adjacent to a mica surface.* Physical Review Letters, 2001. **87**(15): p. 156103.
91. Van Dinh, Q., T.Q. Vo, and B. Kim, *Viscous heating and temperature profiles of liquid water flows in copper nanochannel.* Journal of Mechanical Science and Technology, 2019. **33**(7): p. 3257-3263.
92. Ho, T.A., et al., *Aqueous NaCl and CsCl solutions confined in crystalline slit-shaped silica nanopores of varying degree of protonation.* Langmuir, 2011. **28**(2): p. 1256-1266.
93. Ho, T.A. and A. Striolo, *Polarizability effects in molecular dynamics simulations of the graphene-water interface.* The Journal of Chemical Physics, 2013. **138**(5): p. 054117.
94. Barisik, M. and A. Beskok, *Equilibrium molecular dynamics studies on nanoscale-confined fluids.* Microfluidics and Nanofluidics, 2011. **11**(3): p. 269-282.
95. Suk, M. and N. Aluru, *Molecular and continuum hydrodynamics in graphene nanopores.* RSC Advances, 2013. **3**(24): p. 9365-9372.
96. Cohen-Tanugi, D. and J.C. Grossman, *Water permeability of nanoporous graphene at realistic pressures for reverse osmosis desalination.* The Journal of Chemical Physics, 2014. **141**(7): p. 074704.

97. Sampson, R.A., *On Stokes's current function.* Philosophical Transactions of the Royal Society of London. A, 1891. **182**: p. 449-518.
98. Jensen, K.H., A.X. Valente, and H.A. Stone, *Flow rate through microfilters: influence of the pore size distribution, hydrodynamic interactions, wall slip, and inertia.* Physics of Fluids, 2014. **26**(5): p. 052004.
99. Celebi, A.T. and A. Beskok, *Molecular and Continuum Transport Perspectives on Electroosmotic Slip Flows.* The Journal of Physical Chemistry C, 2018. **122**(17): p. 9699-9709.
100. Nguyen, C.T. and A. Beskok, *Saltwater transport through pristine and positively charged graphene membranes.* The Journal of Chemical Physics, 2018. **149**(2): p. 024704.
101. Nguyen, C.T. and B. Kim, *Stress and surface tension analyses of water on graphene-coated copper surfaces.* International Journal of Precision Engineering and Manufacturing, 2016. **17**(4): p. 503-510.
102. Nguyen, C.T., M. Barisik, and B. Kim, *Wetting of chemically heterogeneous striped surfaces: Molecular dynamics simulations.* AIP Advances, 2018. **8**(6): p. 065003.
103. Celebi, A.T., M. Barisik, and A. Beskok, *Surface charge-dependent transport of water in graphene nano-channels.* Microfluidics and Nanofluidics, 2018. **22**(1): p. 7.
104. Qiao, R. and N.R. Aluru, *Atomistic simulation of KCl transport in charged silicon nanochannels: Interfacial effects.* Colloids and Surfaces A: Physicochemical and Engineering Aspects, 2005. **267**(1-3): p. 103-109.
105. Celebi, A.T., M. Barisik, and A. Beskok, *Electric field controlled transport of water in graphene nano-channels.* The Journal of Chemical Physics, 2017. **147**(16): p. 164311.
106. Lyklema, J., *Overcharging, charge reversal: chemistry or physics?* Colloids and Surfaces A: Physicochemical and Engineering Aspects, 2006. **291**(1-3): p. 3-12.
107. Qiao, R. and N. Aluru, *Charge inversion and flow reversal in a nanochannel electro-osmotic flow.* Physical Review Letters, 2004. **92**(19): p. 198301.
108. Rezaei, M., A. Azimian, and D.T. Semiromi, *The surface charge density effect on the electro-osmotic flow in a nanochannel: a molecular dynamics study.* Heat and Mass Transfer, 2015. **51**(5): p. 661-670.
109. Cao, Q. and R.R. Netz, *Anomalous electrokinetics at hydrophobic surfaces: Effects of ion specificity and interfacial water structure.* Electrochimica Acta, 2018. **259**: p. 1011-1020.
110. Nguyen, C.T. and A. Beskok, *Charged nanoporous graphene membranes for water desalination.* Physical Chemistry Chemical Physics, 2019. **21**(18): p. 9483-9494.
111. Wu, Y., L.K. Wagner, and N.R. Aluru, *Hexagonal boron nitride and water interaction parameters.* The Journal of Chemical Physics, 2016. **144**(16): p. 164118.
112. Taherian, F., et al., *What is the contact angle of water on graphene?* Langmuir, 2013. **29**(5): p. 1457-1465.